Monitoring of Lung Cancer Patients during Radiotherapy Using Combined Texture and Level Set Analysis of CBCT Images

Roushanak Rahmat

Submitted for the Degree of Doctor of Philosophy

HERIOT-WATT UNIVERSITY

March, 2017

Abstract

In the UK, radiotherapy (RT) contributes to a large amount of lung cancer treatment while its imaging information is limited to computed tomography (CT) and cone beam CT (CBCT) images. The oncologists defines the gross tumour volume (GTV) manually on the planning-CT images before any treatment starts. Manual contouring suffers from many disadvantages and the bad quality of CBCT images makes it very challenging for the clinicians to observe tumour behaviour in the time of treatment. CBCT is the only kind of image available throughout the whole course of RT which is used in the mechanical procedure of adjusting patient position before starting each session of treatment and is not generally used by clinicians for monitoring the tumour. The goal of this thesis is to develop a tumour detection model of non-small cell lung tumours on CBCT images in the course of treatment. By developing this process clinicians will be greatly aided in their role, helping them to detect lung tumours to allow better diagnosis and improving patient treatment outcome. Therefore a new segmentation approach is proposed as combined texture analysis and level set model. It has the potential capability to track the variation of the tumour shape over time of treatment solely using CBCT images, and evaluate the accountability of RT for different patients. The texture analysis, second-order statistics obtained from gray level co-occurrence matrices (GLCM), highlight the tumour boundary and help Chan-Vese and Li level set models convergence in the segmentation process. Further on a new parallel level sets model is proposed by combining Chan-Vese and Li models in the concept of vector-valued image level set. This new approach overcomes the difficulties in the parameter settings of current models by giving more freedom of choice in tuning parameters as well as selecting level set models. All proposed models were evaluated on the dataset of fifty different patients suffered from non-small cell lung cancer. For the validation procedure, qualitative analysis was carried out by an oncologist as there is no ground truth in each CBCT image during RT. The decision of the oncologist based on patient history has proven the results of this work. For quantitative analysis, the Dice coefficient is used to evaluate the tumour segmentation results on CBCT compared to GTV on CT images prior to treatment to evaluate the amount of changes especially after one third of RT on CBCT #10. Additionally, the proposed segmentation models had the accuracy of almost 90% to the GTV delineated by the oncologist for the only one patient in the dataset having GTV on CBCT images which proved the ability of these models for further analysis during the absence of GTV on CBCTs. For improving this research and helping the clinicians at most, the proposed segmentation model can be used as a notification model to assist clinicians for a better understanding of the tumour during RT and subsequent use in offline adaptive radiotherapy (ART).

To my parents: for all the love, affection and guidance.

To Steve and Bill: for being the best supervisors one can hope for.

Acknowledgements

One of the greatest pleasures of writing a thesis is acknowledging the effort of many people whose names may not appear on the cover but without their hard work, cooperation, friendship and understanding, this PhD would have been impossible.

I wish to express my deep and sincere gratitude to my precious supervisor, Prof. Stephen McLaughlin, who found time in a very busy schedule to teach me about concepts of my work, monitor my progress and answer my questions. I have very much benefited from his professional advice and guidance along my PhD. I appreciate him for accepting me as his PhD student, it was an honour. I would like to thank my amazing and very kind co-supervisor, Dr. William Nailon, for his support, attention and time. I am also deeply indebted for his advises, guidance, and for the patience duration my PhD. Without his help, this work would never have been possible. I am very grateful to them for their constant encouragement and many fruitful discussions.

Also, I would like to thank Prof. Allan Price for evaluating my results and answering my questions about oncology, I am very grateful for all he taught me.

My deepest appreciation and love go to my dear parents, Dr. Gholamreza Rahmat and Mrs. Mahin Rahmat and my amazing brothers, Bijan and Danial. I thank them for their sacrifice and encouragement. My kind family who are the idols in my life, I do appreciate their trust and believe in me.

I am truly honoured and privileged to have worked in the Computer Vision Lab at Heriot-Watt University as well as Radiotherapy Physics, Image Analysis and Cancer Informatics group at Cancer Research Centre, The University of Edinburgh. The groups consist of some of the smartest people I have met in my life and having constant access to them made my PhD studies a very rewarding experience. I would like to thank the terrific people that I met in these labs, particularly Yang, Dean, Kun, Dan, David, Marcelo and Gwen for their good company and constructive support.

Finally, I would like to express my thanks to examiners, Prof. Yvan Petillot and Prof. Stephen Marshall for taking the time to evaluate this thesis. I also need to appreciate the wonderful Scottish education system, James-Watt Scholarship which helped me financially to get this degree, NHS for providing me with data and collaboration of Heriot Watt University and The University of Edinburgh for their support during this study.

ACADEMIC REGISTRY

Research Thesis Submission

Name*:*			
School:			
Version: *(i.e. First, Resubmission, Final)*		Degree Sought:	

Declaration

In accordance with the appropriate regulations I hereby submit my thesis and I declare that:

1) the thesis embodies the results of my own work and has been composed by myself
2) where appropriate, I have made acknowledgement of the work of others and have made reference to work carried out in collaboration with other persons
3) the thesis is the correct version of the thesis for submission and is the same version as any electronic versions submitted*.
4) my thesis for the award referred to, deposited in the Heriot-Watt University Library, should be made available for loan or photocopying and be available via the Institutional Repository, subject to such conditions as the Librarian may require
5) I understand that as a student of the University I am required to abide by the Regulations of the University and to conform to its discipline.
6) I confirm that the thesis has been verified against plagiarism via an approved plagiarism detection application e.g. Turnitin.

* *Please note that it is the responsibility of the candidate to ensure that the correct version of the thesis is submitted.*

Signature of Candidate*:*		Date:	

Submission

Submitted By *(name in capitals):*	
Signature of Individual Submitting:	
Date Submitted:	

For Completion in the Student Service Centre (SSC)

Received in the SSC by *(name in capitals):*			
Method of Submission *(Handed in to SSC; posted through internal/external mail):*			
*E-thesis Submitted (**mandatory for final theses)***			
Signature:		Date:	

Please note this form should be bound into the submitted thesis.

Contents

Figures and Tables

Figures

Tables

Acronyms and Abbreviations

2D/3D	Two/Three Dimensional
ART	Adaptive Radiotherapy
CBCT	Cone-Beam Computed Tomography
CRT	Conformal Radiation Therapy
CT	Computed Tomography
CTV	Clinical Target Volume
DICOM	Digital Imaging and Communications in Medicine
DRR	Digitally Reconstructed Radiograph
EBRT	External Beam Radiotherapy
GTV	Gross Tumour Volume
ICRU	International Commission on Radiation Units
IGART	Image Guided Adaptive Radiation Therapy
IGRT	Image Guided Radiation Therapy
IMRT	Intensity Modulated Radiation Therapy
kV	kilovolt
LINAC	Linear Accelerator
MLC	Multi Leaf Collimator
MRI	Magnetic Resonance Imaging
MV	Megavoltage
OAR	Organ at Risk
PET	Positron Emission Tomography
PTV	Planning Target Volume
RT	Radiotherapy
RCS	Reference Coordinate System

Publications

Published

Roushanak Rahmat, Yang Feng, William Nailon and Stephen McLaughlin, Lung Tumour Segmentation using a Combined Texture and Level Set, Dundee Medical Image Analysis Workshop 2015, Dundee, UK on 27th March 2015.

In Preparation

Roushanak Rahmat, William Nailon and Stephen McLaughlin, A Review of Level Set Models to Image Segmentation, to be submitted to IEEE Transaction of Medical Image Processing.

Roushanak Rahmat, William Nailon and Stephen McLaughlin, Texture and Level Set Model for Lung Cancer, to be submitted to Medical Image Understanding.

Roushanak Rahmat, William Nailon and Stephen McLaughlin, A case study of tumour evolvement of a patient suffered from collapsed lung during RT, to be submitted to Radiation Oncology.

Roushanak Rahmat, William Nailon and Stephen McLaughlin, Parallel Level Sets in Vector-Valued Image Model, to be submitted to MIUA 2017.

Chapter 1

Introduction

1.1 Introduction

In 2011 in the United Kingdom (UK) 43,463 people were diagnosed with lung cancer and in the following year 35,371 deaths were directly attributable to it [1]. A major part of lung cancer treatment involves radiotherapy (RT), that is the treatment of cancer by ionising radiation. This aims to deliver a dose of radiation to the diseased tissue whilst minimising damage to healthy tissue. RT contributes towards 40% of curative treatment for cancer [2]. It is used to treat lung cancer patients during different fractionation schedules that usually last several weeks.

In RT planning, delineation of the volume of interest is based on a visual assessment of medical images, such as X-ray, computed tomography (CT) and magnetic resonance imaging (MRI), by an oncologist. The accuracy of the volume of interest is dependent primarily upon the ability to visualise the tumour, interpret anatomy and understand the potential areas of tumour involvement based on tumour biology. Interpretation of these variables is complex, time consuming and requires considerable clinical expertise.

In lung cancer, CT imaging is used before treatment for planning the therapy. During the treatment period there is no MRI taken in the majority of cases due to the high cost, lengthy time and delay reporting associated with it. During some RT treatment cone beam computed tomography (CBCT) images are produced which are used for patient positioning. Regardless of the RT approach it is essential that the gross tumour volume (GTV) is accurately defined on CT images used for RT planning and on CBCT images acquired at the time-of-treatment to verify the position of the patient. However, CBCT images suffer from poor soft-tissue contrast, which makes identification of the GTV or indeed the tumours on these images extremely difficult to identify. This is a major problem for clinicians when assessing CBCT images to discern changes due to disease progression and response to RT.

Figure 1.1 illustrates some differences in two relevant slices of CT and CBCT. CBCT produces poorer quality images than CT and projections in CBCT occupy a cone beam shape rather than CT images which is a fan beam shape as shown in Figure 1.1.a. compared to

Figure 1.1.b. The radiation source in CT rotates around the patient but in CBCT it is fixed. It also has a lower radiation dose as the slices do not overlap as in CT and has a lower image resolution. The CT image on Figure 1.1.c. contains a small tumour which is not visible in the relevant CBCT slice on the Figure 1.1.d.

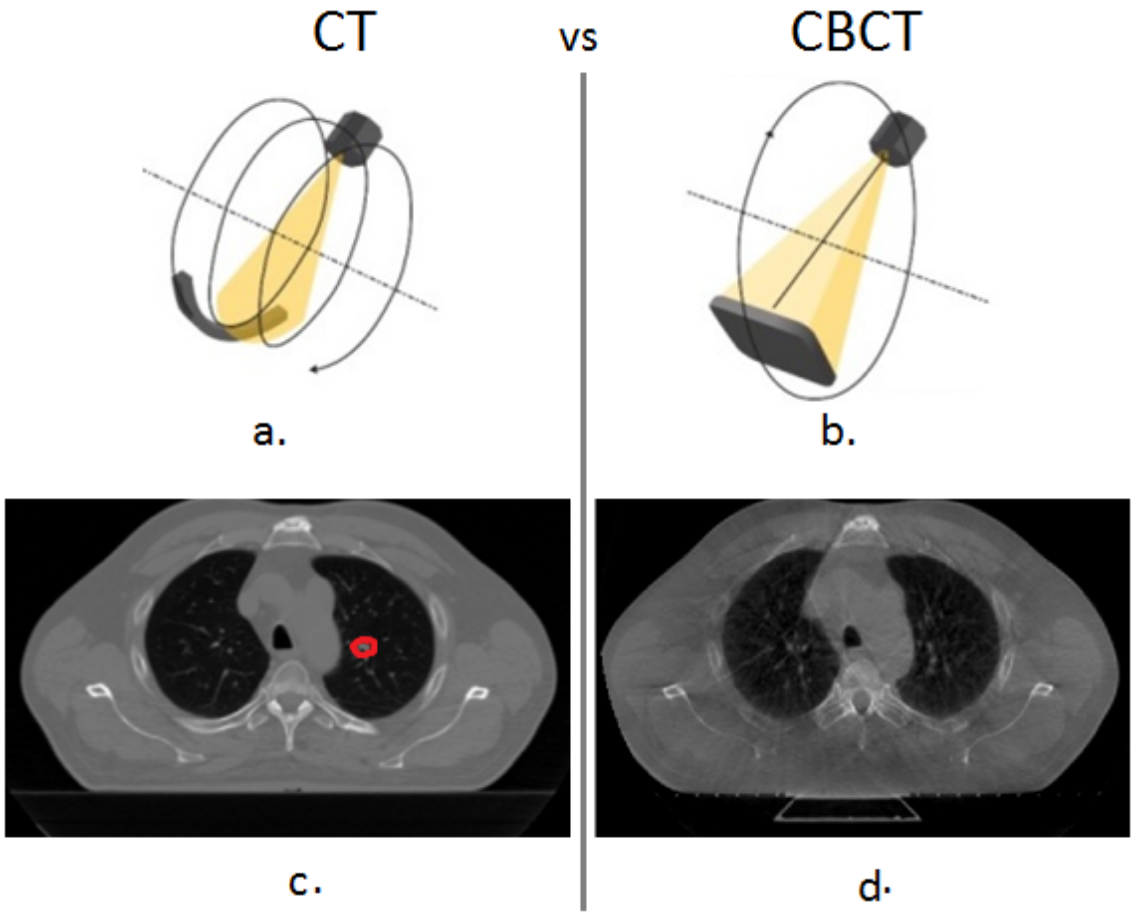

Figure 1.1: CT vs CBCT, a. fan beam, b. cone beam [3], c. CT image with an obvious tumour delineated in red and d. CBCT image relevant to c without showing the tumour due to lower quality.

The poor quality of CBCT images restricts the ability of clinicians to monitor the status of a tumour size during treatment thus limiting potential to adapt the RT dosage and consequently minimizing further damage to healthy tissue. Therefore, the tumour is radiated with the same shape and position defined on the planning-CT for the whole period of treatment. Since a tumour may shrink or expand, knowing the situation of the patient during treatment can be of considerable assistance for clinicians, especially since treatment sessions can be as long as one month.

This research aims to improve and enhance the quality of CBCT images and analyse the situation of tumours during the whole period of RT. This will enable clinicians to identify changes in tumour size. There is however no gold standard during treatment due to the

difficulties in visualizing and interpreting CBCT images. This research is focused on analysing the changes after specific RT sessions while the course of treatment is ongoing. The focus has generally been at fraction 10 (#10), that is the 10^{th} day of treatment, as it is more likely that the tumour position and condition may have changed by this point in response to radiation.

To obtain tumour size information during treatment (the main objective of this thesis), texture analysis combined with a level set method was applied to the CT and CBCT images. The hypothesis is that the texture of a cancerous region will change during treatment and differ from a healthy region. Therefore texture analysis will boost the quality of the region of interest compared to normal CBCT images. Level set methods were used as the segmentation model to find tumour boundaries on #10, which utilised the images from #1 for parameter tuning.

The combined texture and level set model was applied to CBCT image data from fifty lung cancer patients treated at the Edinburgh Cancer Centre in 2010-2011 and results reviewed by a radiation oncologist. This model has the potential to alert clinicians to unacceptable changes in tumour shape and location. The model was first tested on non-medical images which had ground truth and then studied in detail on the lung CBCT of the dataset. One patient had ground truth on the CBCT images due to the specific location of the tumour inside the lungs. This enabled the quantitative analysis to be done of the proposed models. Therefore as a result, the combined texture and level set model showed 90% shape and area similarity to the tumour shape on CBCT while illustrating 30% of tumour shrinkage for its CBCT #10.

Choosing an appropriate level set method with proper parameters is the most challenging issue in the tumour segmentation. A novel level set technique is proposed which combines two or more different level set methods in parallel. This model is inspired by vector-valued imaging that uses different information layers of the same image for segmentation. In the proposed parallel model, the input image is the same in each layer but a different level set method is applied to each layer. Alternatively, it can be the same level set method but using different parameter settings in each layer. This concept is further extended to a multi-phase level set for multi-object segmentation applications. The accuracy of this model is compared using non-medical and medical images. The proposed parallel level set methods can be formed differently but the most compatible form was compared to the conventional vector-valued image level set and proved more flexible for non-medical cases by 90%, shown in Section 4.5.3.

In this chapter, Section 1.2 provides a brief overview of RT, to illustrate the difficulties in this research. Concepts in RT are explained, which are required to better understand this work. In addition, some of the limitations in lung CBCT images that restrict clinicians' interpretations are discussed. In Section 1.3 the main objectives of this research as well as

its contribution to the literature are presented and discussed. In Section 1.4, the framework of monitoring lung cancer using a combined texture and level set model and its further potential is considered. Finally, Section 1.5 provides an overview of the thesis for the reader.

1.2 Overview of Radiotherapy Treatment

Medical imaging has been always a highly challenging and popular area of research. It began with the indistinct glow from the highly energetic electromagnetic radiation observed by Roentgen in 1895 [4]. Since then, diverse imaging technologies such as Ultrasound, CT, colour doppler ultrasound, computed radiography (CR), MRI, positron-emission tomography (PET), and 2D and 3D imaging methods have been developed. The improvement in medical imaging from planar X-ray to multi-dimensional images has greatly enhanced medical science and treatment methods. Different medical techniques are used for different purposes due to their inherent advantages and disadvantages. For example, MRI is mainly designed for imaging of soft tissues and CT is normally applied to examine more dense material such as areas of fracture, haemorrhage, calcification, and infarction. This is especially true in the field of radiation treatment and planning. RT is based on ionizing radiation, which kills cancerous cells by damaging their DNA [5]. Tumours are essentially a tissue mass that is growing out of control often with signs of swelling or edema. The treatment of cancer can be performed with radiation if the shape, magnitude, location, type and size of the tumour is well understood.

In lung tumour treatment, RT is one of the most commonly used methods and in the UK, CT modalities are used widely on planning the treatment. RT is mainly used for localized tumours to deliver specific radiation doses to the cancerous cells. The radiation particles are mostly photons which are focused on the position of the tumour inside the body during treatment [6]. Figure 1.2.a. shows the CT machine which is used for the first stage in RT. Based on the images acquired from CT, the oncologist manually delineates the tumour shape. Using this knowledge of tumour shape, size, position and type, the radiation dose is calculated and delivered via a linear accelerator (LINAC) machine. As shown in Figure 1.2.b. before starting the treatment, the patient position is adjusted by the radiographer at the LINAC so that the planned treatment isocentre is in the correct position. CBCT is an embedded imaging system on the LINAC. The LINAC has two arms that extend and rotate around the patient body. CBCT is mostly carried out once at each fraction of treatment to verify the exact set up. The flowchart in Figure 1.2.c. shows the pathway for a typical lung cancer RT:

1. Imaging for planning: Planning-CT images acquired for planning the RT.
2. Treatment planning: The stage where clinicians plan the treatment by defining the tumour shape, treatment period and dose calculation per treatment.
3. Patient set-up for treatment: The CBCT image acquisition before treatment for the purpose of adjusting patient position to receive the planned radiation therapy.
4. Imaging for verification: Checking CBCT images by the radiographer to set-up and verify the correct position of the tumour.
5. Treatment: Start of the RT using the LINAC operated by a radiographer using information supplied by the clinical team.

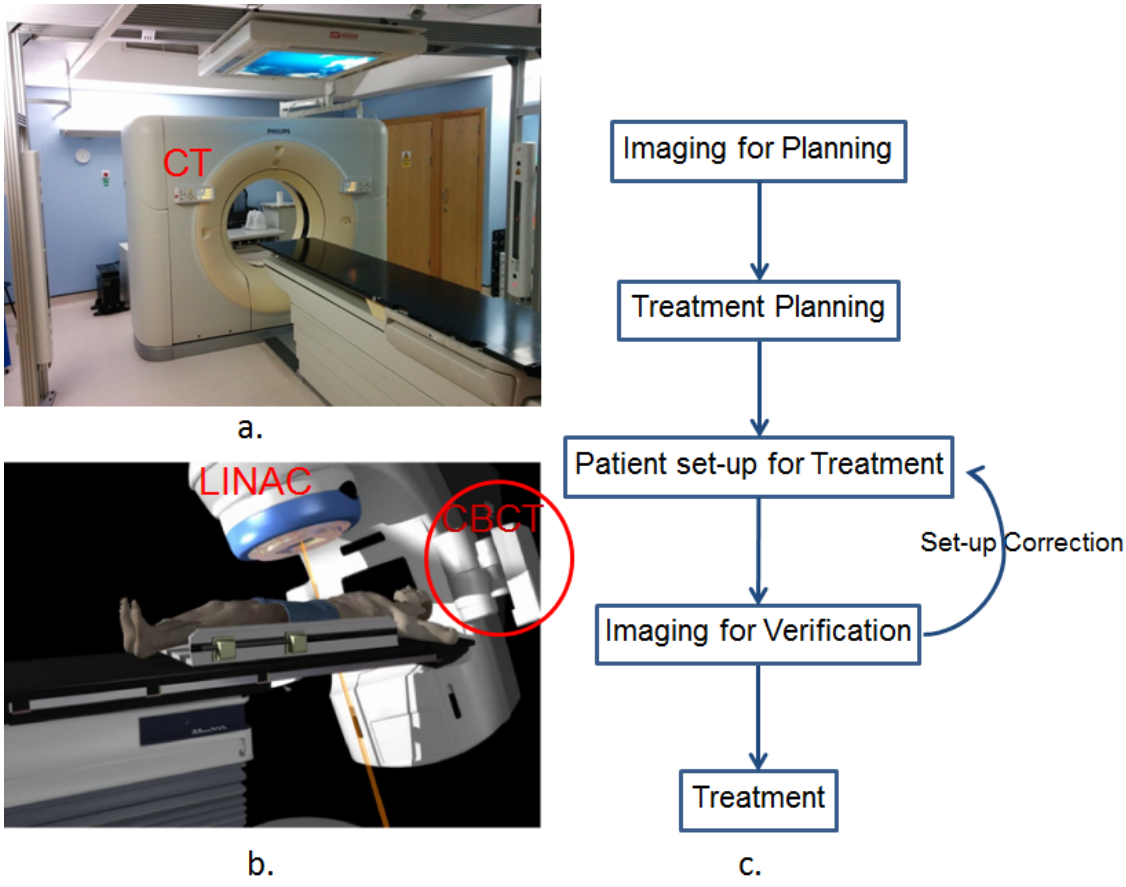

Figure 1.2: a. CT, b.LINAC and c. Pathway of a typical course of RT.

Planning the treatment based on the available LINAC for treatment differs. Conventional RT conformal RT (CRT) as shown in Figure 1.3.a. was used to radiate the tumour from different angles at constant dose. Intensity-modulated RT (IMRT) however, adjusts the delivery dosage based on the shape of the tumour. In IMRT, organs at risk (OAR) receive less radiation and the main delivery is focused on the tumour volume as in Figure 1.3.b.

In treatment planning, finding the exact shape of a tumour is the most challenging issue. The universal standards in RT were introduced by the international commission on ra-

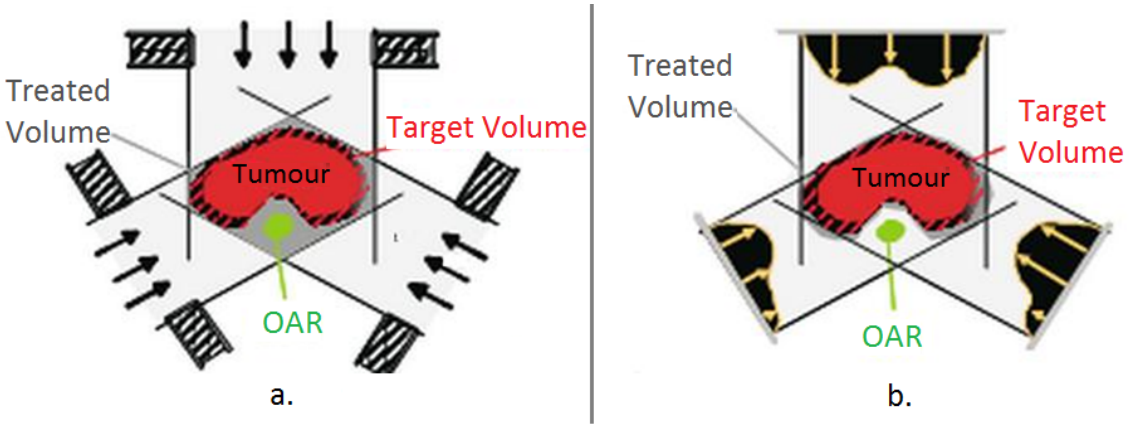

Figure 1.3: Two different RT dose delivery techniques a. CRT and b. IMRT [7, 8].

diation units (ICRU) [7, 8]. These include the GTV in Figure 1.4 and other associated planning concepts. However, it is particularly difficult to generate a generally applicable method without any prior knowledge. In practice the GTV boundaries drawn by clinicians are delineated not only by image information but also based on medical information and experience. Different clinicians may contour the GTV slightly different. As a result, most literature focuses on automatic or semi-automatic methods for certain types of cancers. In this thesis, the GTV contours available on pre-treatment images or planning-CT images generated by clinicians are taken as a starting point for the analysis of CBCT images.

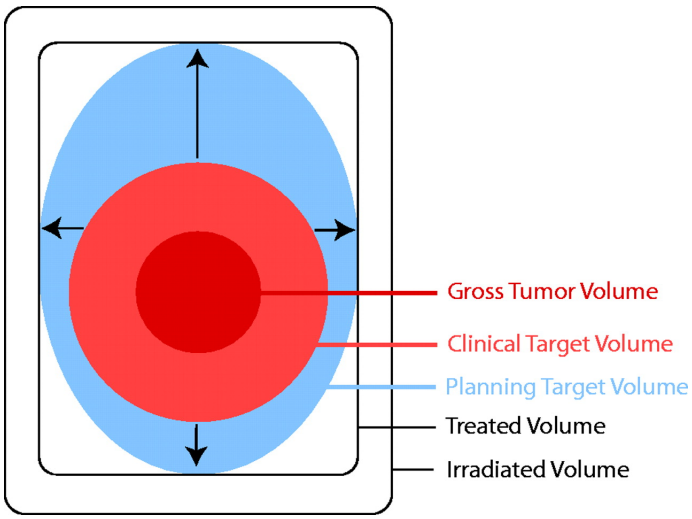

Figure 1.4: Illustrative example of GTV, CTV, PTV and their ratio (after [7, 8]).

Clinical target volume (CTV) is another term used when defining the RT boundary which contains the GTV and an estimated region around the GTV. Since the GTV is delineated on a planning-CT a few days or weeks before starting treatment, clinicians expect some movement or even growth of the tumour mass as well as estimating the breathing

movement of the patient during treatment [7]. Therefore, an even larger planning tumour volume (PTV) is the target of radiation during dose delivery. Although the dose calculation and delivery is targeting PTV, GTV is the most similar boundary to the actual tumour shape. An example ratio of PTV, CTV and GTV is shown in Figure 1.4 to illustrate their concept of treatment volume.

The planning-CT is of a sufficient quality which enables clinicians to manually delineate the GTV on each slice. This information is used in dose calculation and delivery. The oncologist knows from empirical data that the tumour will most likely shrink but there is the possibility of growth or movement inside the lungs. Treatment continues for the whole course of RT based on the first shape taken from the planning-CT. The main problems with current CBCT imaging are:

1. Smaller size compared to planning-CT images.
2. Lower quality and noisier compared to planning-CT. This complicates the comparison of these data for the same patient.

It is extremely difficult for the clinicians to see the tumour using CBCT images, hence no gold standard exists. The limitations of CBCT images combined with the lack of a gold standard by the oncologist during treatment has restricted research in this area. However it is a significant clinical problem and is the main motivation for this thesis, i.e., to improve the quality of CBCT and more accurately analyse the tumour shape during treatment thus assisting clinicians in making critical decisions that will impact on patients.

1.3 Objectives and Contributions

The objectives of this thesis reporting research on image analysis of the lung cancer treatment based on external beam RT and the contributions are:

1. The main objective is to determine the GTV boundary on CBCT. Usually in medical image analysis literature, researchers approach GTV segmentation with prior knowledge or a gold standard, but the absence of the gold standard on CBCT images in this research makes the problem extremely complicated. CBCT images are different from planning-CT images, with a poorer quality, smaller size, and shorter time of acquisition. Although CT images with their GTV are used as the primary reference, CBCT may show the changes due to RT and disease progression. Thus there is a need to pre-process CBCT images, i.e., denoising due to their poor quality and then registering them to planning-CT images to extract/transfer the primary GTV.

   The major contribution of this thesis is using texture analysis prior to level set segmentation to enhance low quality CBCT images thus producing improved lung

tumour segmentation. Prior knowledge of CT and the strength of this segmentation leads to analysis of the patient's situation during RT. The method is used not to exactly define tumour boundary as this is not possible but to indicate to clinicians and provide them with a better qualitative understanding of tumour changes during RT. The Dice coefficient was used to evaluate the changes of segmentation on CBCT compared to GTV on CT before any treatment for finding the changes. A clinical oncologist, evaluated the results for this method on twenty six patients visually and compared them slice by slice and rated the algorithm performance.

2. The second objective is to ease the usage of level set segmentation as the current models are very much dependent on their parameter setting and finding appropriate parameters is particularly challenging in the absence of any ground truth on the data.

   Therefore another contribution of this research is a new level set technique. First, the parallel level sets in vector-valued image model can choose the best force calculation in each iteration as it has two different level set models competing with each other and takes the average of their force in each iteration. This model benefits from the strength of two models and minimizes any error that could arise with a single model based technique. Second, the parallel level sets is extended in multi-phase technique which can apply different level set models or the same model with different parameters to segment different objects. The multi-phase level set model so far deals with the same level set model applied at the same time.

3. Another objective is setting the parameters of level set to the closest possible combination that enables the level set for its best segmentation performance. Training the parameters is impracticable and selecting based on trial and error is very difficult.

   The relevant contribution to this issue is done by finding the closest performance of level set on CBCT #1 to the GTV on planning-CT. At first, all possible sets of level set parameters are selected by choosing the possible range for each parameter and letting level set perform by any of these combinations. Then selecting the set with more than 90% similarity among them and GTV.

4. The last but the most important objective is helping clinicians carry out lung cancer treatment during RT.

   The contribution here is an algorithm which can be applied in medical system to monitor lung cancer evolution during RT. This method can be applied on each fraction to be used as an offline adaptive RT (ART) to correct the treatment at the next fraction.

1.4 Framework of the Thesis

The framework for this thesis is displayed in Figure 1.5. This process starts from planning-CT images and their relevant GTV, followed by CBCT images which are registered to the CT images to map the GTV from CT on them. By applying texture and level set segmentation on CBCT #1 and having GTV as the starting point, a good set of parameters can be obtained which might need few iterations by checking the similarity between the segmentation contour and the GTV on planning-CT data. Since CBCT #1 images are acquired before any RT and after the planning-CT therefore having the Dice coefficient of more than 90% would result into an appropriate set of parameters. Extending the process from here to CBCT #10 can give a reliable estimation of the tumour shape through the RT process. Therefore the same process of registration and texture analysis combined with level set model should be applied on CBCT #10 by considering the obtained set of parameters from CBCT #1. The similarity between the segmentation on CBCT #10 and GTV on planning-CT is the final analysis on CBCT #10. Since almost one third of the RT is done at this stage, a threshold value for the Dice coefficient at 70% is chosen. If the similarity is more than the chosen threshold therefore RT should be continued but if not, it can be an estimation of changes in the tumour. The proposed framework can be extended further to be used in offline ART applications.

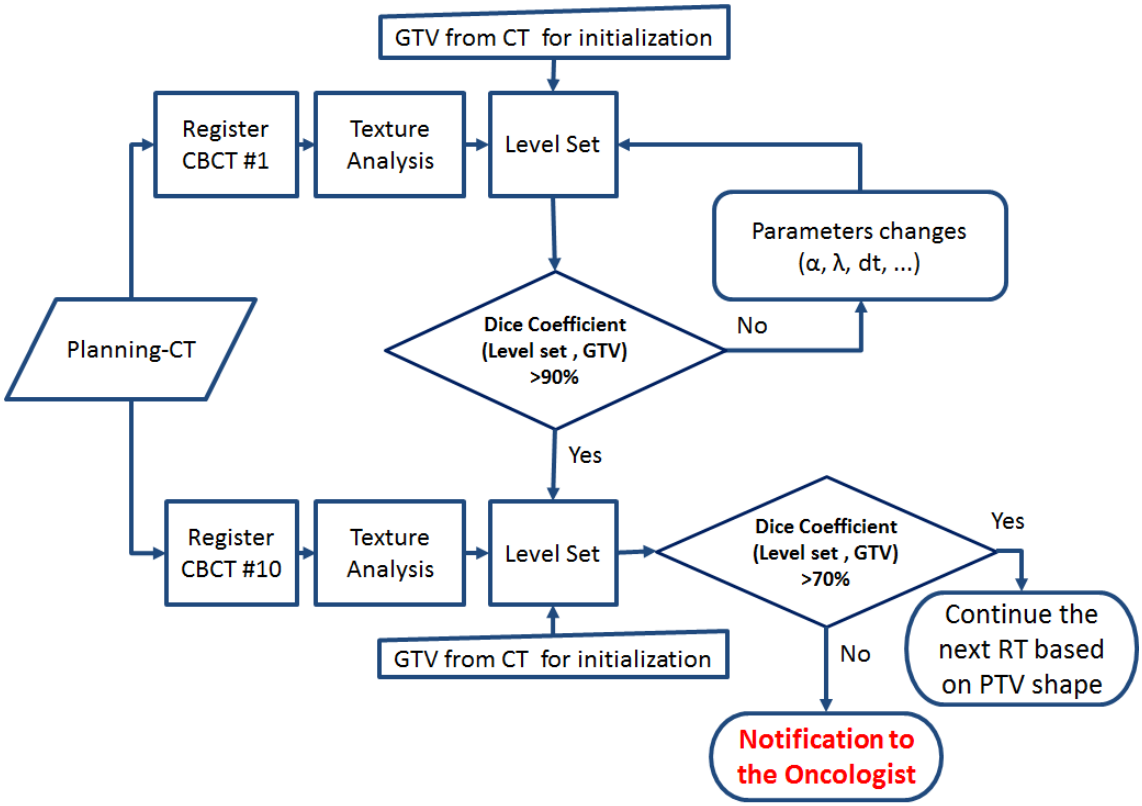

Figure 1.5: The proposed framework for monitoring lung cancer anatomical envelopment during RT using combined texture and level set model.

1.5 Outline of the Thesis

An overview of medical background related to this project is given in Chapter 2. An outline of medical image processing methods used in this work is presented in Chapter 3. Chapter 4 discusses the reasons for the selection of the methods presented in Chapter 3. In Chapter 5, one specific patient for which ground truth was available is studied. The proposed models are applied to this data to prove the efficiency of this work both quantitatively and qualitatively. As the rest of data set lacks a gold standard, using the results from Chapter 5 as a reference, Chapter 6 studies the whole dataset, processing the data step by step and providing a qualitative analysis. Finally, Chapter 7 concludes this research. Each chapter is summarized in the following paragraphs.

Chapter 2 focuses on the necessary medical background for placing this thesis in context. The RT and some relevant challenges in lung cancer treatment are summarized. Lung anatomy, cancer and its alternative treatment options, specifically RT, are explained. Commonly used DICOM (digital imaging and communications in medicine) tags/information are also introduced. Also a brief description of medical image processing fundamentals which can assist in understanding this research, various pre-processing (image conditioning) methods including re-sampling, and Dice coefficient for data analysis are discussed.

Chapter 3 explains the background studies of image processing algorithms used in this research. It discusses the fundamentals of the proposed models and current literature in level set methods. Active contours and specifically level set are discussed, also the difference between implicit and explicit models and some of the advantages/disadvantages of snakes as well as level set methods. A survey about different level set methods, the properties and applications of them are covered. Finally, texture analysis method and its usefulness for many image processing application specificity in this research is outlined.

Chapter 4 explains the selected level set and texture analysis methods from Chapter 3. It tests the popular level set methods on non-medical and medical images. Test images in this chapter include six images which are usually compared in level set papers as well as two MRI slices of the brain and two CT of the lungs. The proposed parallel level sets method in vector-valued based and multi-phase based shapes are also introduced and applied to some test images. Their performance is explained and compared with other models.

In the dataset for lung cancer only one case had a ground truth on each slice of the CBCT scan. It had a concentrated tumour shape connected to the body of the lungs, which made ground truth delineation possible by the oncologist. Therefore Chapter 5 is designed to evaluate to robustness of the proposed texture and level set model. Texture features of this case are observed and their best combination with level set method is tested quantitatively and qualitatively. Finally conclusions are drawn and compared with the proposed parallel level set method.

Chapter 6 discusses the test results and conclusions of the proposed technique of cascading texture analysis and level set methods. It uses lung cancer dataset which does not have any gold standard. This chapter introduces the characteristics of all data and registration of these images. Texture features and their combination with level set are applied and assessed by clinicians compared to the gold standard to validate the results.

In Chapter 7, conclusions of all the work presented in this thesis are made and the relevant contribution to the literature are summarized. Also, some suggestions for further work based on the discussion of the results are introduced.

Chapter 2

Background

2.1 Introduction

CT and CBCT images are acquired before, during and after lung cancer treatment in RT. They are used in tumour diagnosis, monitoring tumour progression and planning treatments. These images contain structural and electron density information which can indicate the ability of materials to absorb radiation and consequently be used to calculate the dose distribution from a given beam arrangement. Segmenting tumours on CT images is challenging due to the poor discrimination provided by CT for soft tissue when compared to MRI of tumour cells in lung cancer. Furthermore it is extremely challenging on CBCT images due to their noisy characteristics as the projection of the beams is broader than CT. The CBCT image detectors and source is a part of the LINAC and moves around the patient in a similar manner to a LINAC gantry whereas in CT the patient is moved inside the CT. CT is slower as moving the patient can not occur as quickly as moving the image source/detector in CBCT.

For the purpose of radiation treatment, having an accurate estimation of tumour size is vital. By knowing the shape and size of the tumour, external beam RT can provide a very accurate dose delivery to the tumour cells. A typical RT procedure comprises of:

1. Contouring: Delineating the tumour boundaries and organs at risk is carried out before starting RT.
2. Dose calculation: Determining the maximum dose delivery to the tumour.
3. Simulation and irradiation: Checking and delivering radiation to the tumour.

The tumour shape and boundaries are defined manually by oncologists as this cannot be achieved using automatic image processing segmentation techniques [9]. Manual contouring suffers from many disadvantages, it is tedious, not reproducible and different oncologists do not identify exactly the same tumour shape for the same patient. The RT community has acknowledged that the issue of developing automatic contouring methodologies should be given a high priority [9].

CBCT images, which are acquired during or before placing the patient on the treatment position, are even more complicated and difficult for the oncologist to contour. Therefore,

because of the lack of contour on CBCT during lung cancer RT treatment, it is more difficult to assess the response of cancer to RT. By processing the CBCT images and comparing them with CT images, a useful lung tumour contouring model is implemented in this thesis. This model has great potential as an alert process which notifies the oncologist about any change in size and shape of the tumours during the course of treatment.

This chapter explains the background of this research in medical imaging content. It provides the reader with the required terms and for lung cancer RT image analysis. In Section 2.2 lung anatomy, lung cancer and its treatment methods are briefly explained. In Section 2.3, an introduction to RT techniques and its applications are described. The fundamental definitions of medical imaging and the DICOM standards are presented in Section 2.4. CT and CBCT scanners, being the source of medical images in this work, are also mentioned in this section. Technical details in different aspects of transformation, similarity calculation, optimization and assessment are included in a short literature review of segmentation which is presented in Section 2.5.2. Also this section provides a description to re-sampling and Dice coefficient which discusses them for image conditioning and quantitative analysis.

2.2 The Lungs and Lung Cancer

Lung cancer, affecting one of the most vital organs in human body, is ranked as the second most common cancer after prostate and breast cancers for men and women respectively. Up to 17% of men and 14% of women may be affected by lung cancer regardless of being a smoker or non-smoker and almost 25% of cancer associated deaths are categorized as lung cancer [10]. The national health service (NHS) of the UK spends almost £9,000 per patient per year on lung cancer treatment [11]. Early stage treatment costs less than the advanced stages, for example the treatment of a lung cancer patient in stage 1 to stage 4 can vary from £7,952 to £13,078 [12]. The survival rate of lung cancer patients after treatment is less than 40% as shown in Figure 2.1 based on cancer research centre statistics and data provided by the cancer research centre UK [13].

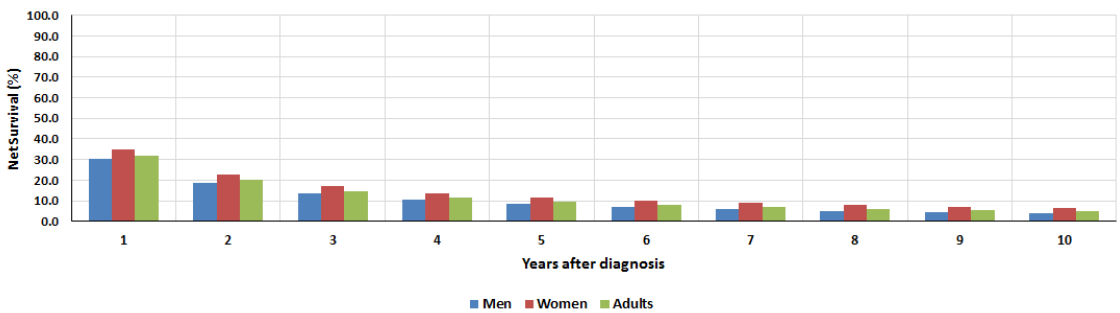

Figure 2.1: Lung cancer survival in the UK (data from [13]).

2.2.1 Overview of Lung Anatomy

Figure 2.2 illustrates cancerous lungs inside the human body. Lungs are a pair of soft tissue organs positioned within the ribcage. They cover the heart inside and are above the liver and stomach. Each of the lungs consists of two elastic bags for air to pass through their branches, so that oxygen can pass into the blood and carbon dioxide can be removed. The trachea (windpipe) is the route for air into the lungs via two main tubular branches, called bronchi. The bronchus itself consists of microscopic branches (bronchioles). In a healthy adult the two lungs, weigh approximately 1 *lb* (0.45 *kg*) each. However, the left lung embeds the heart and is about 10% smaller than the right one. Consequently, the right lung is shorter, thicker and broader. The average total lung volume, for young adults, is 6 *litres*; while only 0.5 *litre* of air is used for normal breathing.

Figure 2.2: Localized tumours in the right lung [14].

Each lung has a broad bottom part, called the base, and a narrow top, the apex. The lungs are surrounded by a double-layered membrane that encloses and protects each lung. Figure 2.3 shows the cross-sectional shape of lungs.

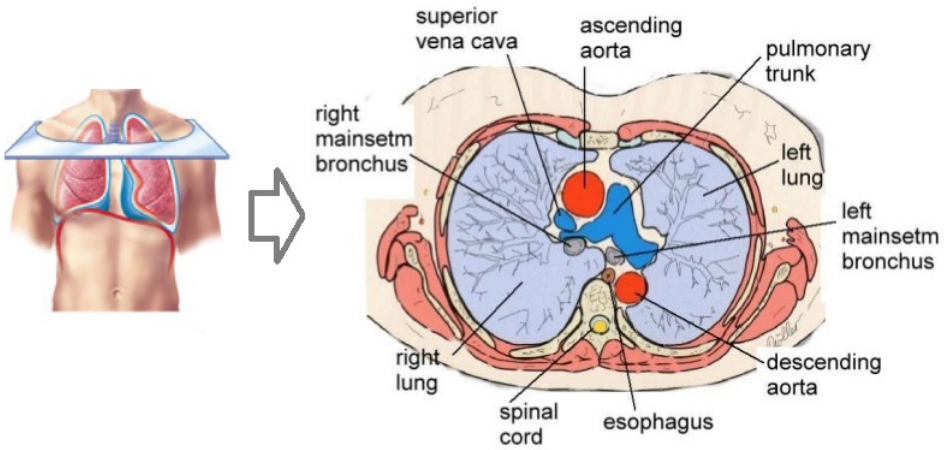

Figure 2.3: Lung anatomy cross-sectional transverse view [15].

The lungs are connected via other organs in between as shown in the cross-sectional view which also might be affected by the tumours inside each lung or affect them if they are cancerous themselves.

2.2.2 Overview of Lung Cancer Disease

In the UK, almost 1 person in every 1000 of the population is diagnosed with lung cancer each year, with older people usually being the main victims of this disease. The NHS statistics indicate that people from 70 to 74 years old are the largest cohort to suffer. Almost 90% of patients are categorized as smokers though non-smokers are also affected. Bloody coughs, continuous coughs, tiredness, dramatic weight loss and chest pains are some of the symptoms of cancerous lungs which usually manifest in advanced stages of this ailment. Lung cancer can be formed of cancerous cells only inside lungs, or can spread to other parts of the body [6].

Lung cancer severity depends on the propagation of cancerous cells in the lungs and other organs. Lungs are considerably larger than some other organs, therefore tumours can grow and spread for some time before being sensed by patients. Even when symptoms such as coughing and fatigue occur, people presume they are due to other causes. This makes it more difficult to discover the disease in its earlier stages and therefore diagnosis usually occurs in the advanced stages.

Different types of lung cancers grow and spread at different rates, usually they can be divided into two main types. The first type is the small-cell which is rare and occurs in almost 20% of patients. It is more dangerous due to its fast spreading nature within the lungs and it also spreads to other parts of the body earlier than the second type lung cancer. The oat cell or small-cells are microscopic and majority of cases they are filled with the nucleus (the control centre of cells) [12].

The second type is non-small-cell lung cancer which is more common affecting almost 80% of patients. Different stages of this type are explained by the following:

Stage I: Tumours are in the lungs only.
Stage II: The cancerous cells spread beyond the lungs and grow in the nearby lymph nodes as well.
Stage III: Cancer cells grow inside the lymph nodes and can even spread to the other lung on the other side of the body.
Stage IV: At this stage, tumour cells are widespread, growing in other organs such as the liver. It is the most progressive stage.

Figure 2.4 illustrates some levels of four stages in non-small-cell lung cancer.

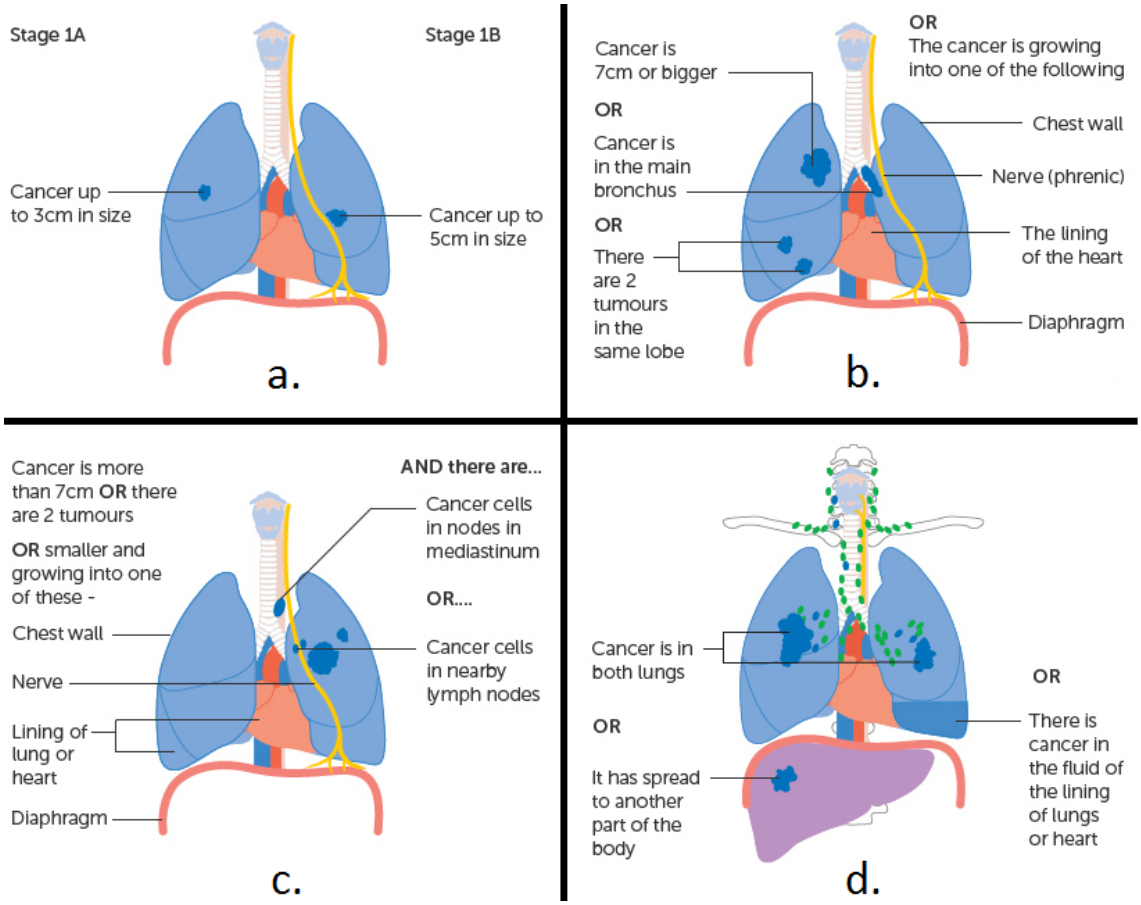

Figure 2.4: Some levels of four stages in non-small-cell lung cancer: a. Stage IA and IB, b. Stage IIB, c. Stage IIIB and d. Stage IV [16].

This research studies the second type, non-small-cell lung cancer. The dataset carries all different stages of this type. Therefore the proposed model can be tested against the different stages.

2.2.3 Overview of Lung Cancer Treatment

The treatment of lung cancer can be carried out by surgery, chemotherapy, RT or any combination of these methods. A team of clinicians decide the best treatment for each patient depending on the general health of the patient, the cancer type, stage of advancement and position of the tumour in the lungs.

Chemotherapy is a method which is usually used for tumours that have spread across lungs and other organs, typically by administering anti-cancer drugs, mostly small-cell type. Surgery in lung cancer is another method of treatment and is mostly used for localized tumours. As shown in Figure 2.5, tumour removal via surgery would cause some healthy tissue removal as well and can range from removing a wedge section to being as severe as

removing a whole lung. It is painful compared to RT, therefore some patients prefer RT to surgery. Furthermore, RT combined with chemotherapy is called chemo-RT.

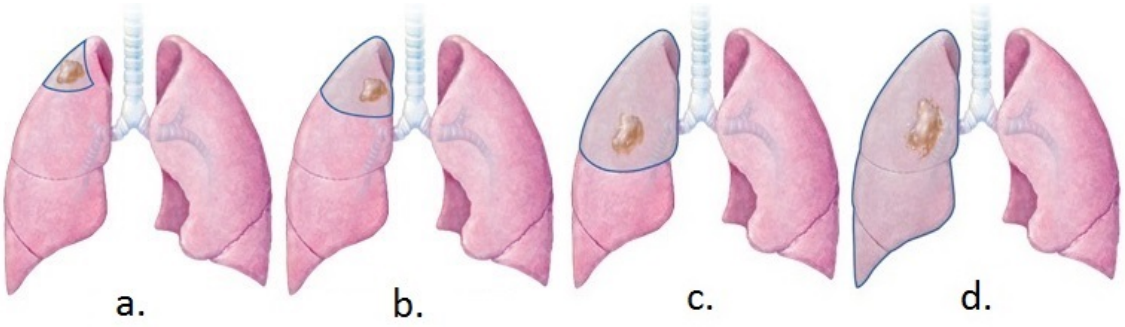

Figure 2.5: Different lung surgery section removal: a. wedge resection, b. segmental resection, c. lobectomy and d. pneumonectomy [15].

RT can be used before, after or during surgery because some cancer cells could expand during operation. The purpose of using RT before surgery is to shrink the tumour. Such a process is called neoadjuvant treatment. If it is used after surgery to kill the remaining cells which were not removed during surgery it is called adjuvant treatment. Surgery combined with RT is usually recommended for early stage small tumours, however a sole RT program is more practical if the patient is not in an appropriate condition to be operated on.

2.3 Radiotherapy

RT is the most common treatment for lung cancer. It is also used in treatment of benign tumours such as thyroid diseases as well as some blood disorders. RT is based on high-energy radiation. In RT, the cancerous cells are targeted by ionization radiation to kill them by damaging their DNA. By treating cancer in this manner, normal cells will also be affected by radiation. The treatment of lung cancer can be very challenging during RT because of movement of the chest. During the process of image acquisition as well as radiation, the patient should stop breathing. Holding of breath can affect the shape of different organs and cause very small differences in images acquired in different times. Also weight loss or gain can be another issue in the size of lungs. In treatment planning, clinicians try to estimate the tumour shape by considering all of these possibilities during treatment. RT is painless but depending on the treatment plan, the patient can go through treatment for periods of days to weeks. In the case of lung cancer, IMRT or IGRT is usually performed in 20 to 36 sessions/fractions which can last from four to seven weeks, or three treatments each day for about twelve days. Stereo-tactic body RT (SBRT) which

carries the radiation from different angles around the body usually delivered in three to eight fractions [17].

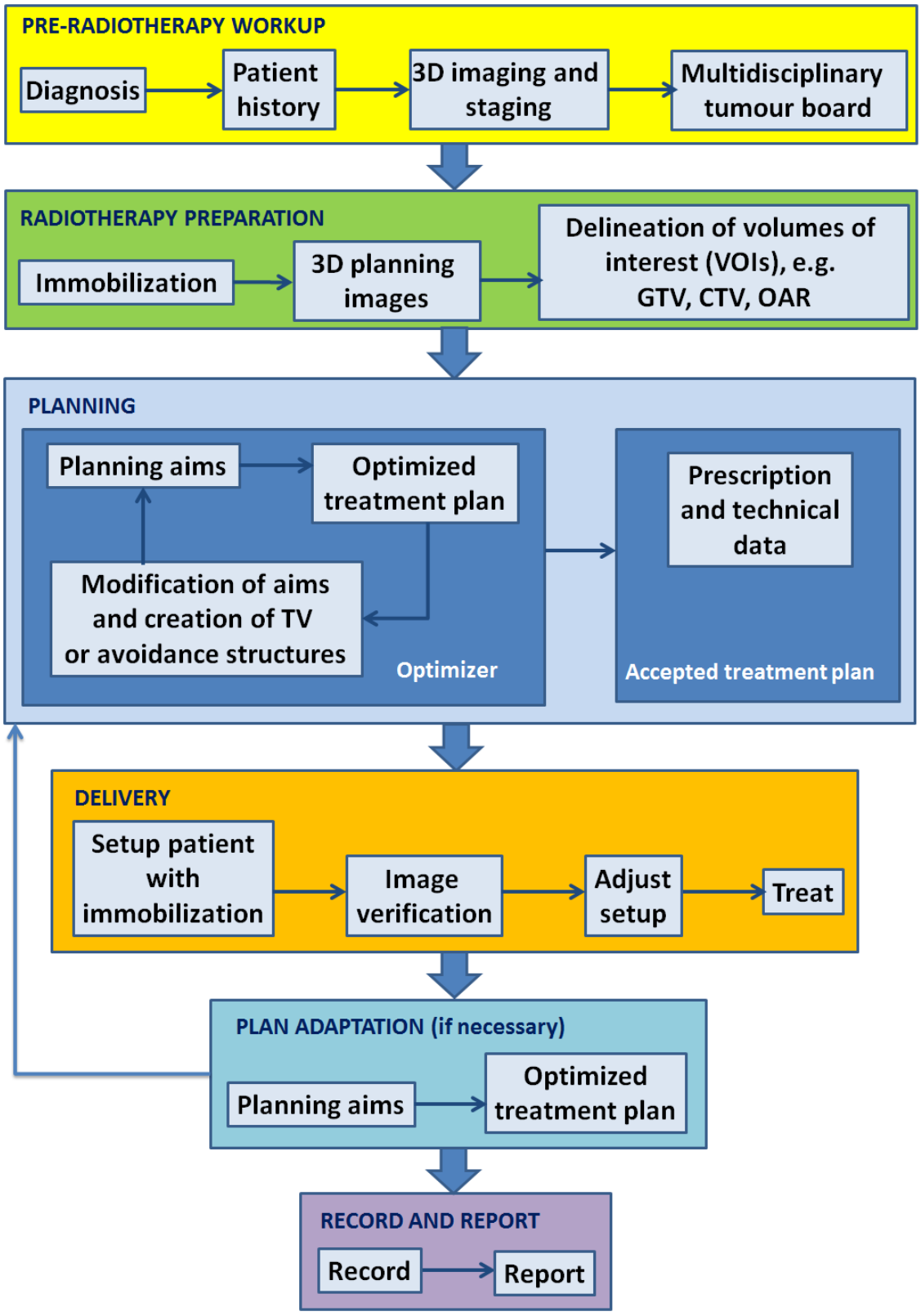

Figure 2.6: Flow chart of a typical course of RT (after [8]).

A flow chart of a typical course of RT is shown in Figure 2.6 [8]. It illustrates the main path of RT as:

1. Pre-RT: The pre-RT is the stage of decision making by clinicians to plan the treatment.
2. RT preparation: Tumour delineation by the oncologist on the planning-CT images acquired before RT treatment.
3. Planning: Optimizing the treatment plans by modifying the tumours shape and dosage calculation.
4. Delivery: Started by image acquisition such as CBCT to adjust patient for treatment and finally delivering radiation.
5. ART (Not necessary): This stage is not used in all RTs. It can be online or offline. In online ART, before starting each session of treatment, some modification can happen on the current treatment plan. For example, a new set of images is acquired and processed to define a new volume of interest. In offline ART, the information can be used in future sessions of RT while clinicians have more time to plan and modify the future treatment.
6. Reporting: Recording and reporting the patient treatment information.

RT is either performed inside the body (internal RT) or outside the body (external RT). Internal RT or brachytherapy is carried out by placing a radioactive material inside the body near cancerous cells for a temporary period. This type of RT differs for different patients based on the location and size of tumour. External RT, also known as external beam RT (EBRT), radiates tumour cells in a patient body from an external source. The radiation elements can be of anything from electrons and photons (X-rays or gamma-rays) to heavier elements such as protons and neutrons. The beam source depends mainly on the machine used for the treatment.

External RT takes place in a LINAC, which targets a beam at the volume of interest as seen in Figure 2.7 [18]. LINAC was invented in 1928 by accelerating charged particles. The charged particles release a little amount of energy while travelling through the body but their peak release should happen while reaching the tumour. Delivering the highest dose to cancerous tissues with the least amount of radiation to healthy tissues is very important in dose calculation, therefore targeting PTV properly as well as accurate dose calculation related to the volume and position of tumour is highly important.

In this regard, different technologies in RT have been developed such as image guided RT (IGRT), SBRT and intensity modulated RT (IMRT). IGRT is an RT which uses the information from images such as CT or MRI for radiation. This technology greatly helps in radiating a lower dose to healthy tissues. Inside IGRT some image processing methods can be performed, such as noise removal, motion correction and registration to improve treatment analysis. SBRT uses different radiation beams around the patients which are

focusing on the tumour from different angles which increases the dose delivery to the tumour.

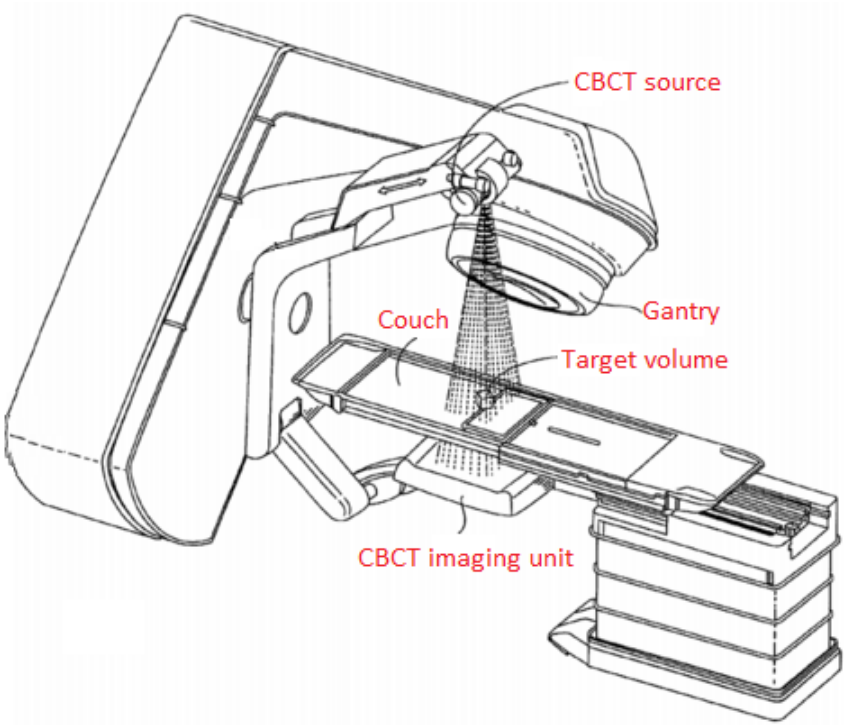

Figure 2.7: Linear accelerator with embedded CBCT imaging mechanism [18].

IMRT is the advanced version of 3D conformal RT (3DCRT) shown in Figure 2.8. These techniques dynamically reshape radiation beams based on tumour shape as shown in Figure 2.9. The beams can be formed to match the expected PTV by giving the proper shape to the multi-leaf collimator. It also changes the dose delivery to each voxel from different angles of radiation.

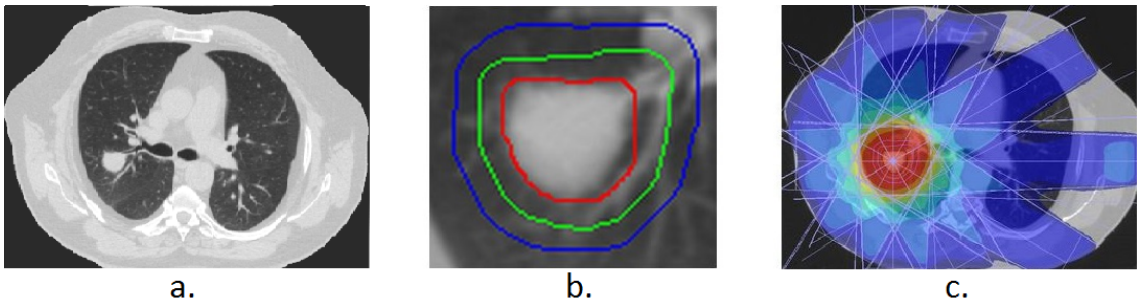

Figure 2.8: Treatment planning through simulation of the radiation: a. a CT image b. planning-CT with GTV in red, CTV in green and PTV in blue contours shown and c. treatment planning through simulation of the radiation [19].

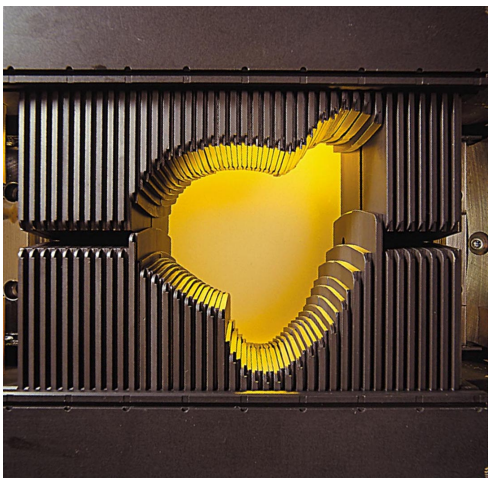

Figure 2.9: Varian 80-leaf collimator for shaping a radiation beam [20].

During treatment the tumour may shrink, indeed that is the aim of the treatment, but there are possibilities of expansion or movement of the tumour inside the lungs due to progression of the disease. Therefore having some information regarding the progression of disease can be vital for the patients who do not respond well to RT. Generally, there is no MRI or CT imaging available during treatment. Due to lack of time, high cost and other difficulties associated with MRI, this imaging technique is not performed. On the other hand, CT might expose the patient to more X-ray radiation. Also sometimes the time between two treatments is so short that it does not provide clinicians with another opportunity to reconsider the tumours shape during treatment. CBCT images often available during treatment, and are used to position the patient on the LINAC couch to identify the patient isocentre. This ensures that the exact position of tumour in the body is irradiated. Therefore, in general, the only modalities of images available for lung cancer treatment are CT and CBCT. As CBCT quality is poor, they are not used by clinicians for analysis of soft tissue but to set up the patient.

In planning, the extent of the tumour is defined as the radiation target (GTV, CTV and PTV); after the target is defined a dose delivery calculation will be made based on the form of the treatment, for example curative or palliative. After the plan is finalized a simulation is carried out to verify that the radiation set-up and dose will be delivered appropriately. After the physical dose, delivery quality control needs to be implemented to assure that the outcome of the treatment meets expectations. Since this thesis studies image analysis for GTV definition, in this section RT planning has been detailed, with an emphasis on the impacts and challenges brought by the recent introduction of IMRT.

2.4 Medical Imaging Fundamentals

To aid understanding of medical imaging modalities, some fundamentals in medical imaging need to be described first. The first and foremost concepts are pixels in 2D imaging and voxels in 3D volumes. Pixels, which are usually square units in imaging, are the smallest quantity in an image. Their physical size can vary depending on the application and resolution of acquisition device. Voxels are the pixel concept extended into 3D. In medical imaging they are usually presented in $millimetres^3$ (mm^3) on an image. The image pixel values are known as intensity or gray-scale values which represent the amplitude of each pixel.

The image size defines the number of pixels in the x and y directions. The image resolution, which does not define its physical size, is usually presented as pixel spacing in DICOM information. For example, a 200×200 image defines the width and height of the image which are both 200 pixels (and the image size is 40k pixels), it means if the image is 2 inches wide and 2 inches high with a resolution of 100 pixels per inch (PPI). Also, a $200 \times 200 \times 100$ image in 3D refers to 200 pixels per width and height and 100 layers of images (slices in medical imaging) but they do not define the voxel and size. Medical images can be acquired through different planes in the body such as sagittal plane, coronal plane and transverse plane as shown in Figure 2.10.

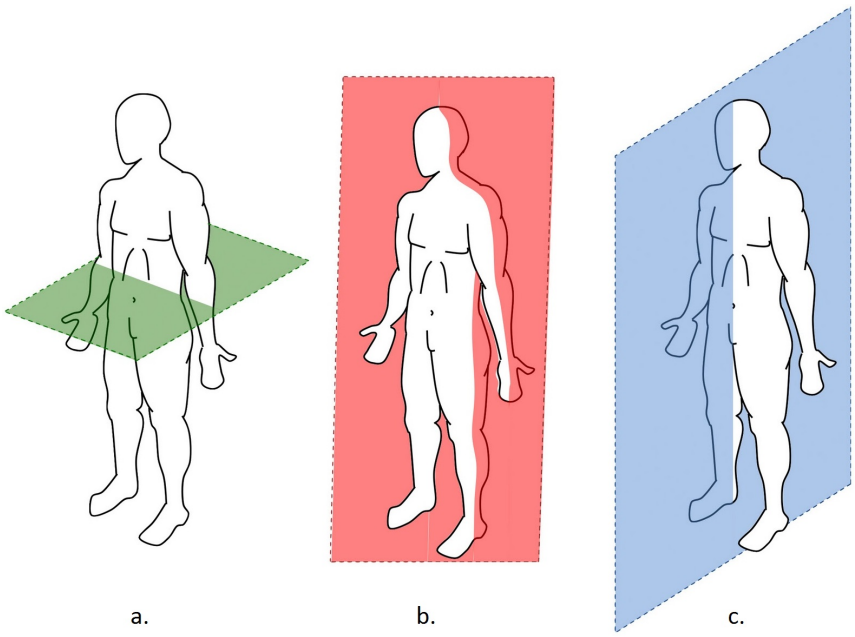

Figure 2.10: Planes of notion in CT image acquisition a. transverse plane: plane that runs through the body and horizontally divides it into upper and lower portions, b. frontal or coronal plane: plane that runs perpendicular to the transverse plane and divides the body into anterior and posterior (front and back) portions and c. sagittal plane: plane that runs side by side through the body, dividing it into left and right portions [21, 22].

The images of CT and CBCT acquired for this research are all taken from the sequence of transverse mode as shown in Figure 2.11. This montage illustration of tumour slices does not show much about tumours but illustrates the sampling frequency of imaging per 3*mm* thickness in the transverse cross-sectional direction.

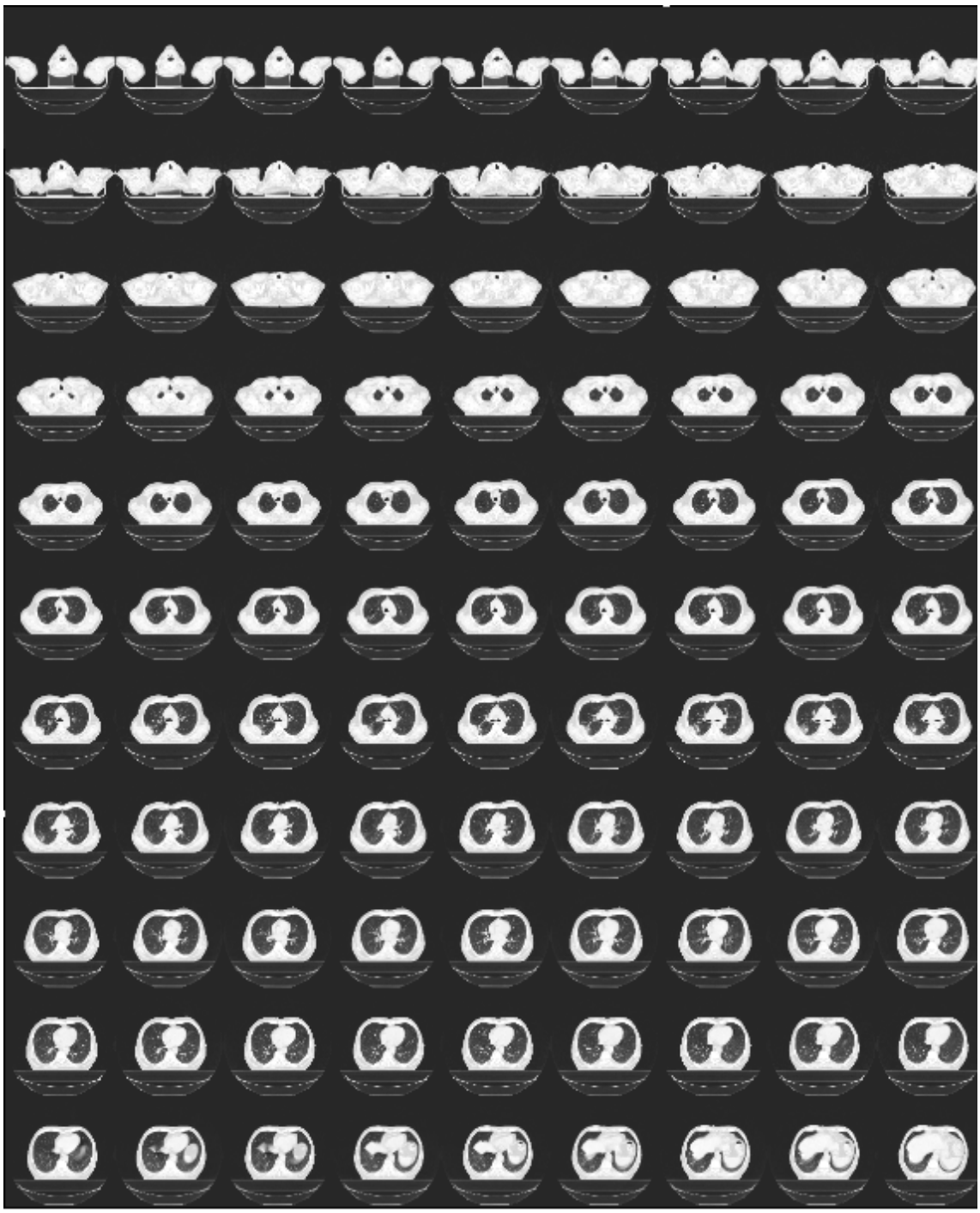

Figure 2.11: Lungs montage illustration of planning-CT slices for Patient 25. There are 130 slices for this patient acquired on 10-05-2011 at Western General Hospital, Edinburgh, UK.

In medical imaging, the images are in standard DICOM format and embed the information of patient, disease, treatment, date and information needed for further processing of the image [23]. Some information is sequential for the same patient which should be considered during the treatment. Some convey different transformation data required between the patient-based system and image-based system. These data are very important in the registration procedure which is required in RT treatment, motion correction, 3D shape reconstruction and re-sampling of the data. Important parameters can be read from DICOM information directly including:

1. Pixel Spacing: This information shows the physical pixel size in an image in millimetres (mm) and is usually the same in x and y coordinates.
2. Slice Thickness: This information represents voxel size, the distance between each slice. It is also represented in *mm* but it is usually larger than the pixel spacing.
3. Image Position Patient: This information presents the position of a patient during the image acquisition as the origin of the patient-based coordinate system.
4. Image Orientation Patient: This is also like patient position and is based on coordinates which represents the angle of the patient or imaging/RT device from the origin in the medical space/domain. It is very important if the patient changes the angle of lying on the bed.
5. ROI Contour Sequence: The structure file which carries the information for clinical contours delineated by the oncologist.
6. Registration Sequence: These are the registration parameters set by radiographers to find the reference coordinate between CT and CBCT or any two different data sets which need registration.

This DICOM information is used during pre-processing CBCT images in lung cancer. Especially in image registration these DICOM data can be very useful. The difficulties of CBCT over CT are due to its image generation mechanism, difference in time of acquisition and gray-levels. Figure 2.12 illustrates the difference between a CT and its relevant CBCT slice.

The two slices of CT and CBCT of the same patient after registration illustrate the quality of CBCT declined compared to CT. The red boundary illustrates the GTV on both images and the blue rectangle refers to the ROI. The CBCT slice in this figure was acquired one week after the CT and its histogram shows a large difference of the same ROI. The RIO is chosen from an area containing both soft and hard tissues where their difference is very feasible on CT histogram while not very well separated on CBCT histogram. These differences are explained further in the following subsections.

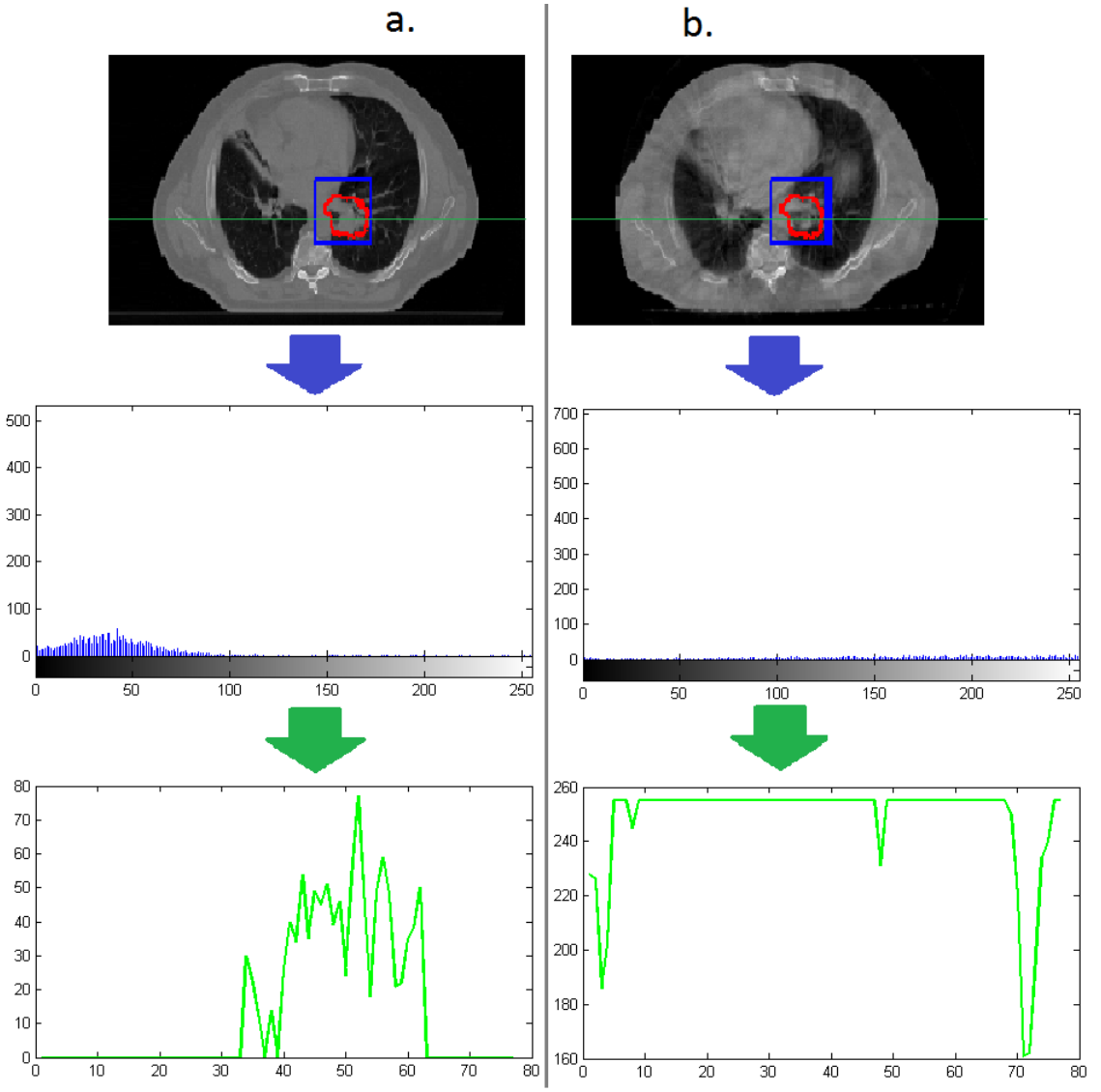

Figure 2.12: Relevant CT and CBCT slices differences, Patient 26 Slice 58, a. CT image and b. CBCT image relevant to CT image on the left side. Both images are followed by the histogram of the cropped part in blue colour and an intensity plot of the line drawn in green colour along the cropped boundary. The red boundary illustrates the GTV on both images.

2.4.1 CT

CT or X-ray CT involves a scanner to visualize anatomical elements using X-rays to capture images from different angles to build cross-sectional (topographical) images of different depth and resolution. In CT, the beam travels across the human body to generate tomographic images. Therefore it can be harmful, increasing the risk of cancer by almost 3% to 5% as the X-ray may damage the healthy tissues while scanning procedure is in progress [24].

CT can visualize broken bones, injured organs, blood disease and strokes amongst other ailments. The imaging procedure using CT scanners is painless and less costly compared than other modalities. It is usually a doughnut shaped machine, open from both ends, with the patient lying on the bed while the bed moves into the hole. An X-ray tube source rotates around the patient and sends narrow beams of X-rays through the patient. Normal CT scans send a sequence of X-ray beams toward the patient from one side. The size of beam is between $1mm$ and $10mm$ wide, that makes a sequence of slices for different depths within the body. On the other side of the patient, there are X-ray fan-shaped detectors to detect the amount of X-ray passing through different organs and tissues of the body. This recorded data can combine different slices of CT images by reconstructing them into digitally reconstructed radiograph (DRR) images which defines the patient position during the RT process.

CT lung cancer scans take less than a minute while patients hold their breath in order to obtain better images due to fewer movements in the chest. More movements cause images to be more blurry and therefore require additional processing for motion correction. The radiographer, doctor or technician who is in charge of capturing the CT scan prepares the patient and leaves the room so as not to be affected by the X-ray. They monitor the patient from another room by controlling the couch movement toward the CT scanner.

In CT, differences between tissues that differ in physical density by less than 1% can be distinguished. The quantitative scale for describing radio-density is measured in Hounsfield units (HU) representing the relative intensity of the organ of interest. The HU scale relates the voxel attenuation coefficients (the quantity that describes the fraction of a beam of X-rays or gamma rays that is absorbed or scattered per unit thickness of the absorber, μ) of different tissues to water and air as shown by the equation 2.1. The coefficient of 1000 is to magnify the values and can be changed but it is chosen to be 1000 for most of scanners.

$$H = 1000 \times \frac{\mu_X - \mu_{water}}{\mu_{water} - \mu_{air}} \tag{2.1}$$

As μ_{air} is almost zero, it can be ignored and the scanner can be calibrated with reference to water. In Table 2.1, different intensities for various organs and tissues are listed.

Substance	HU
Bone	+700 (cancelous bone) to +3000 (dense bone)
Soft Tissue, contrast	+100 to +300
Liver	+40 to +60
White matter	+20 to +30
Grey matter	+37 to +45
Muscle	+10 to +40
Blood	+30 to +45
Kidney	+30
Water	0
Fat	-100 to -50
Lung	-500
Air	-1000

Table 2.1: Different intensities of some typical materials in a CT image [25].

Figure 2.13 also illustrates the different densities for different tissues in lung CT image.

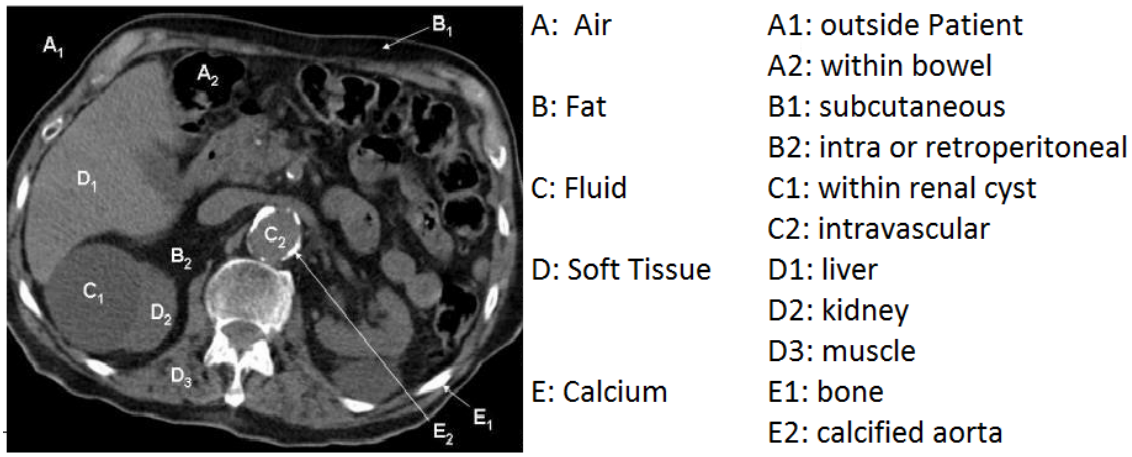

Figure 2.13: Different tissue densities shown in a CT image [25].

This information is very useful for clinicians to contour GTV. Based on their experience they estimate the presence of different tissues in different sections of lungs, and use this to delineate the abnormalities as cancerous tissues.

2.4.2 CBCT

CBCT is a type of CT with conical shape instead of fan shape. It is mostly used in dental imaging but also a component part of a LINAC for interventional radiology (IR) and more recently IGRT. CBCT image quality is much poorer than CT images because of the wider projecting of each beam of X-rays. Their resolution and image size is smaller and they take longer time to acquire. Therefore they are noisier than CT images due to patient breathing as well as their image projection shape. The time of CBCT is at least 5 breaths and it exposes the patient to less radiation compared to CT. CBCT scanners on a LINAC are designed for the purpose of finding the proper position of the patient and tumour before radiating the tumour cells. After putting the patient on the LINAC bed, the CBCT arms extends from the LINAC and rotates around the patient. One arm sends the X-rays and the other arm detects them. The process usually happens before RT treatment and helps the radiographer to find the exact position of the tumour inside the body and target the most precise point. CBCT images are available for all different days of RT treatment and named by fraction. Usually patients will have approximately thirty days of treatment in almost one month.

2.5 Overview of Medical Image Processing

Image enhancement, denoising, registration and segmentation are the main image processing steps used in many medical imaging applications. As previously discussed, the images of CT and CBCT are noisy and blurry in lung cancer RT although the medical acquisition software that processes these images specialises in noise removal and motion correction. Denoising is well studied as the noises are known, as is motion correction since the movement direction of lungs are predictable. But image segmentation still requires the effort of clinicians. There are many models developed which assist clinicians. By clearly identifying a better region of interest to clinicians, patients will have less exposure to radiation and the diagnosis will be faster and more accurate. Medical image segmentation is difficult due to the inhomogeneity in the intensity of the images which can be due to sensitivity of modality (e.g. MRI-soft tissue and CT-bones), noise, faulty devices and human movement. Segmentation also helps in estimating the size, position, shape and volume of tumours [26]. This section provides some description about image conditioning used in this thesis as re-sampling for the follow up registration purposes, then image segmentation is briefly discussed and finally Dice coefficient as the quantitative analysis tool used in this thesis is explained.

2.5.1 Re-sampling of Images

Different modalities usually carry different dimensions and slice thicknesses as well as number of slices. For example, in this study the planning-CT data for fifty different patients involved on average 100 slices and for the CBCT data almost fifty slices. Before applying any image processing algorithm, re-sampling the test data is necessary. In this work up-sampling and down-sampling are both applied. Up-sampling is the process of rescaling an image into a larger size and down-sampling is the reverse.

In this work, the first step before registration of CBCT images to planning-CT images was applying a first-order interpolation (bilinear interpolation) to expand the dimensions of the CBCT image to CT image dimensions and smooth intensity values by re-sampling them. Figure 2.14 and Equation 2.2 illustrate this concept, that the final intensity value for each pixel is the summation of four neighbouring pixels.

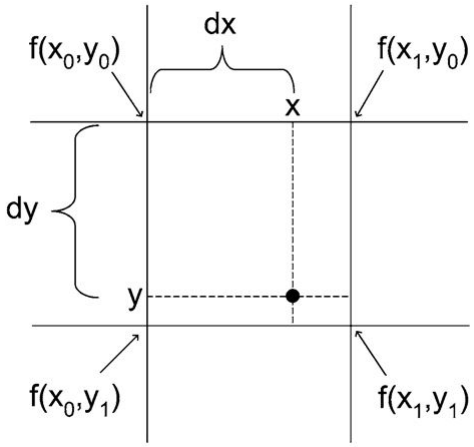

Figure 2.14: The general view of bilinear interpolation of a 2D example with (x,y) the target point.

$$\begin{aligned} g(x',y') = f(x_0 - y_0).(1-dx).(1-dy) \\ +f(x_1 - y_0).dx.(1-dy) \\ +f(x_0 - y_1).(1-dx).dy \\ +f(x_1 - y_1).dx.dy \end{aligned} \tag{2.2}$$

where g is the new intensity of (x,y) point on the image. The area of the square where (x,y) is located is 1. Each square is divided into four sub-regions and the area of each one of them multiplied by the closest neighbour's intensity value to define the new intensity value.

2.5.2 Image Segmentation

Image segmentation can be divided into two main techniques: one is discontinuity based and the other is similarity based. Discontinuity based techniques are designed to detect edges, lines and isolated points, whereas similarity based algorithms are designed to detect thresholding, region growing and region splitting/merging. Edge detection involves detecting discontinuities in the image, the region boundaries being well defined by edge detection due to steep variations in the intensity in object edges. Thresholding is the simplest technique to partition the image by defining a threshold value, which is generally based on image histogram values. Popular models of thresholding are Ostsu's model which is based on maximum variance and K-means clustering. The K-means algorithm is a recursive technique that partitions the image into K clusters. In similarity based techniques, which are more powerful than discontinuity based ones, region growing is one of the simplest models. It is based on initialization of a seed point in an image and growing a region through pixel based image segmentation. It classifies the neighbourhood region of the seed by determining if it is a part of the region or not and it moves until it reaches the object boundaries based on its defined classification growth. Partial differential equation-based methods, variational models and general optimization algorithms are popular methods which are getting used more and more due to their flexibility. Partial differential equation-based methods or PDE-based methods use numerical schemes to solve curve propagation. The basic idea of PDE based model is to minimize the cost function or an energy functional defined for a curve. Parametric methods such as snake models were one of the first models introduced based on PDE which are actually Lagrangian techniques. Level set is another model of this category which considers curve propagation in an implicit manner. Fast marching models are also used widely in PDE models as they permit both a positive and speed propagating speed in an approach called the generalized fast marching method [26].

A great deal of research using many different methods has already been performed [27–30]. Further examples exist in 3D shape recovery of the tumour in brain, lung and other organs, tumour segmentation based on 2D contours [31, 32] as well as 3D contours [33, 34] which have generated considerable interest. There are a number of different approaches proposed for tumour segmentation and volume estimation using techniques such as fuzzy-connectedness in MRI [35], Markov random field [36], support vector machine [37], graph shifts algorithm [38] and Bayesian method [39]. Many active contour models (explicitly snakes and implicitly level set methods) have been proposed and implemented for tumour segmentation over the past twenty years [33, 40]. Many different segmentation techniques have been tested in tumour segmentation, particularly level set methods due to their shape adjustment capability regardless of the objects form.

As the quality of CT and CBCT are different and also CBCT images lack the presence of ground truth therefore choosing the proper segmentation model is an essential. A good segmentation model which can converge to the tumour boundaries with the least amount of prior knowledge is the main concern in this selection. Based on literature review level set models are tested widely and are well performers on medical images in the present or absent of ground truth.

Level set methods are a form of active contour which have the freedom of movement inside an image until it converges to the desired boundary/region. The level set needs to be initialized as a boundary. Figure 2.15 illustrates the movement of level set contour in a period of time from left to right until it converges to the correct boundary. Level set methods can handle complex geometry and topological changes with numerical stability. The initial contour position is arbitrary, it can be anywhere in the image regardless of the location of desired segmentation.

Figure 2.15: An example of level set propagation from left to right using Chan-Vese level set method.

Chapter 3 reviews different level set techniques, implements different models of level set and Chapter 4 discusses their performance in medical imaging for the purpose of tumour segmentation in lung cancers and the follow-up after RT. Also proposed model is cascading texture analysis and level set methods on lung data using CBCT images to estimate the tumour position and size during treatment.

2.5.3 Ground Truth Comparison to Algorithms Output

Qualitative analysis for the medical dataset was done by the expert oncologist and the quantitative analysis was carried out using the Dice coefficient. The Sorensen index or Dice coefficient was developed by Sorenson and Dice as a measure of a comparison. The Dice coefficient can measure the level of similarity between two closed sets, A and B, Figure 2.16.

$$D = \frac{2|A \bigcap B|}{|A| + |B|} \tag{2.3}$$

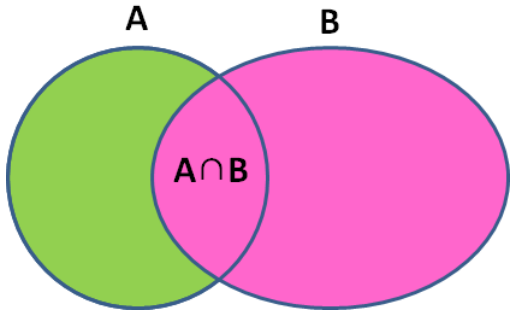

Figure 2.16: Intersection of two closed sets of A and B.

2.6 Chapter Summary

In this chapter, the essential medical background of lung cancer treatment presented to address the problem studied in this thesis. The main issues in the available modalities in lung cancer were discussed as well as the difficulties of developing automatic contouring algorithms for RT planning. CT, CBCT and RT are described with their advantages and disadvantages with respect to lung cancer. An anatomy of the human lungs is presented, with an emphasis on lung cancer. The process of GTV contouring, difficulties in the procedure and the need for assisting clinicians to decrease the time required for treatment planning discussed which not only has significant influence on the productivity of the RT process as a whole, but has great potential to be part of IGRT process to increase the accuracy of PTV definition. A review of medical imaging, image conditioning, image analysis and a short introduction to level set compared to other segmentation models were discussed which would be better studied in next chapters.

Chapter 3

Level Set and Texture Analysis

3.1 Introduction

Image segmentation is the process of partitioning the image into meaningful regions. It is one of the most important techniques in modern imaging for shape reconstruction, volume estimation, object detection and classification. Many different algorithms have been proposed to solve image segmentation problems. Those based on partial differential equations (PDE), began with the Snake technique introduced by Kass in 1987 [41]. The snake model is based on minimization of an energy term to halt the growth of evolving contours at edges or boundaries. Another popular image segmentation method is the level set, introduced in 1988 by Osher-Sethian [42] to overcome the shortcomings of the Snake such as its topological problem such as topological issues as well as accurate prior knowledge for their initialization. Since level set models are independent of prior knowledge, they are very robust segmentation models when there is no ground truth available. Level set methods are used extensively and have many different applications. As a result there is often considerable investigation into the performance of several level set methods for a given problem. It would therefore be helpful to know the characteristics of a range of level set methods before applying any to a given segmentation problem. Several review papers on level set segmentation are available but each is focused on one area or specific aspect of imaging applications. Some of these topics are:

Region-based algorithms; Cremers in 2005 [27], Jiang in 2012 [44].

Medical imaging; Suri in 2001 [45], Elsa Angilini in 2005 [46].

Inverse Problems and Optimal Design; Burger and Osher in 2005 [47].

Piecewise constant application; Tai and Chan in region based methods in 2004 [30].

Deformable models in general; Montagnat in 2001 [48], Suri in 2002 [49].

Short general review; Bhaidasna in [50], Vineetha in 2013 [29].

This chapter reviews a range of level set methods and their application to image segmentation work and explains in detail their properties for practical use. Popular models

were applied to segment synthetic images with defined ground truth and to analyse their performance. The advantages and disadvantages of each model are discussed and their properties and limitations when dealing with different images are compared to show the reasons for choosing the specific level set methods adopted in this research. Also, texture analysis studies are reviewed for the purpose of pre-processing the images prior to segmentation as part of this research.

3.2 Active Contours

Active segmentation models are popular due to their ability to iteratively fit a curve to an image. In general, active contours are growing boundaries/regions for segmenting different objects or regions in an image. These sort of curve evolution models within the image can begin by defining an initial curve, which has the ability to move (expand or contract) until it reaches the object boundaries. The curve movement can be parametric/polygon/explicit or geometric/continuous/implicit. Figure 3.1 illustrates the concept of geometric and parametric algorithms where geometric curves are continuous and parametric curves are polygons. Geometric contours are stored as coefficients of some function and sampled before each iteration. Each sample moves explicitly in each iteration to calculate the new coefficients. However, parametric contours are stored as vertices which all move iteratively. Geometric active contours in general are topologically more flexible as they implicitly move the curve.

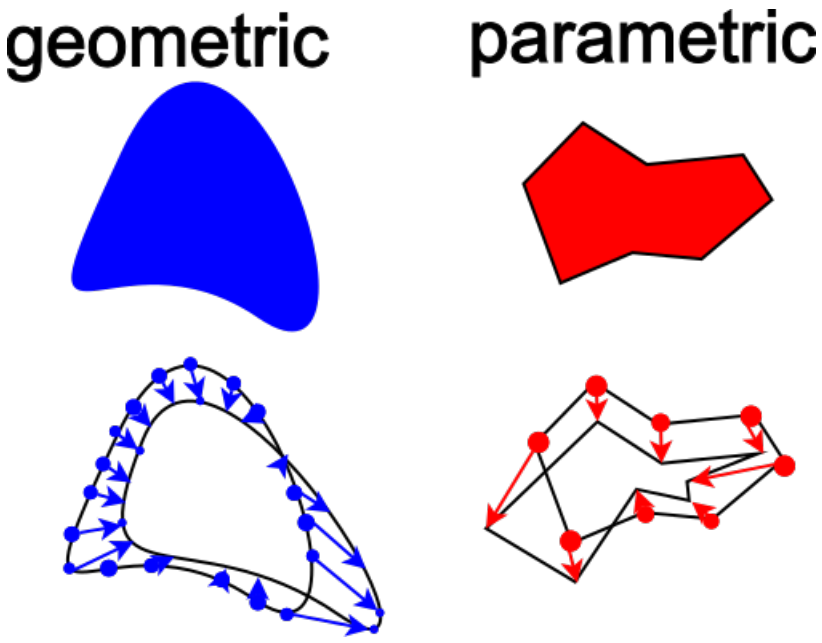

Figure 3.1: Movement of geometric vs. parametric contours.

In Figure 3.2 the black boundary represents the contour C moving with speed F and in the normal direction N perpendicular to the interface, any tangential component will have no effect on the position of the front. F depends on local properties L such as curvature and normal direction, global properties G such as shape and position of the front and independent properties I that do not depend on the shape of the front (some physical energies and properties such as heating an either side of the interface or fluid mechanical effects) [43, 51]. In general, the force is the negative value of the energy field, $F = -\nabla E$. If the curve moves inward, then the force value would be negative $F < 0$ and if it moves outward, it would be positive $F > 0$.

$$F = F(L,G,I) \tag{3.1}$$

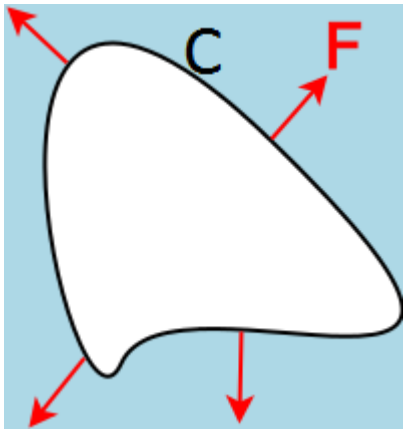

Figure 3.2: Contour evolution with speed of F in normal direction to the contour C.

Active contour model, also called snake is one of the first introduction to an explicit energy minimization contour. A snake model evolves a contour by dividing it into markers/points (parametrising the contour/getting a number of samples of it). Its contour C is shaped based on tracking point positions in a Lagrangian framework that move with the value of the energy field (energy between the inside and outside of the contour).

Snake can be formulated by minimizing an energy functional consisting of an internal elastic energy term $E_{internal}$ as well as an external edge-based energy term $E_{external}$ while C represents the 2D contour of segmentation as $C(s) = (x(s), y(s))$, s=0,..,1 which should be initialised first by the user close to the edges of interest:

$$E_{Snake} = E_{internal} + E_{external} \tag{3.2}$$

The internal energy defines the length of each contour which adjusts the deformations made to the snake. It controls the stiffness, rigidity and elasticity of the curve. The external

energy helps in minimizing the high-gradient areas in the image, it controls the contour to be better fitted onto the image. Equation 3.2 can be expanded into Equation 3.3, where the first two derivative terms refer to the internal energy and the final term represents the external energy.

$$E_{Snake} = \alpha \int_0^1 |C^{'}|^2 ds + \beta \int_0^1 |C^{''}|^2 ds + \gamma \int_0^1 |\nabla I(C)|^2 ds \tag{3.3}$$

where I represents the image in $x-y$ plane, C represents the contour of segmentation, $C^{'} = \frac{dC}{ds}^2$ the first derivative and $C^{''} = \frac{d^2C}{ds^2}^2$ the second derivative. α and β are a composition of the continuity and the smoothness of the contour which are defined by the user. α which can control the continuity of the curve by defining the distance between sampling points in the curve. A larger value of α can stretch the curve more. β controls the amount of curvature, a large value of it can lead into less oscillations in the contour. γ is the weight of external energy or the edge functional which is based on the image gradient which is set to -1.

Snake model suffer from numerous shortcomings that level set method overcomes:

1. Dealing with topological changes: In situations where the curve merges with another curve or splits into two or more segments their performance is poor.
2. Self intersection and overlap: The explicit definition of a snake limits its re-gridding or re-parametrisation process and causes overlaps or self-intersection during the evolution.
3. Dependency on initialization: Their sensitivity to the first estimation of contour position and shape which is because the non-convexity characteristic in energy functional restricts further shape deformation.
4. Extension: Snake models are not able to be developed into other further segmentation applications using colour, texture or motion.
5. Sensitivity to noise: Snake performs weakly in a noisy gradient field as its main formulation does not use region-based statistics whilst level set does.

3.3 Fundamentals of Level Set

The level set was initially designed as an Eulerian formulation of a propagating front, which grows with the speed F perpendicular to the curve. Level set implicitly provides the propagation of the contour with good tracking of the topological changes. In other words, level set embeds a curve in 2D while growing in 3D, shown in Figure 3.3, where the z axis represents values of function $\phi(x,y,t)$ to match the evolution of the interface. The reason of having another dimension compared to snake is for better tracking of parametrisation points that collide in snake. However, level set can stand at each point (x,y) and adjust

the height of the z function which vanishes the topological problem. Such a level set is a growing or shrinking contour based on curvature-dependent speed for propagating fronts. It uses Hamilton-Jacobi equations to reconstruct complex shapes.

$$z = \phi(x, y, t) \tag{3.4}$$

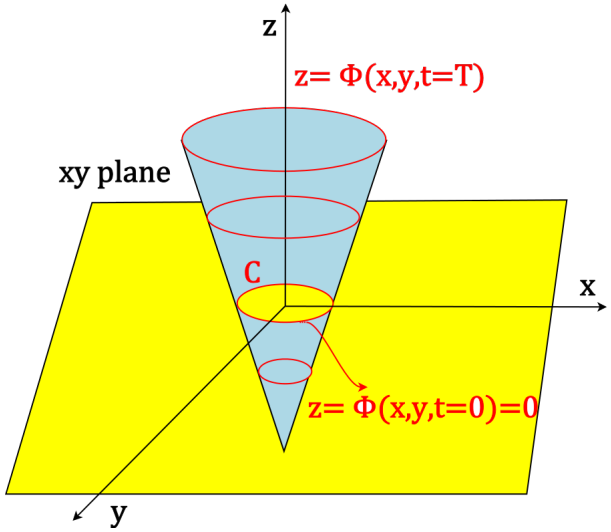

Figure 3.3: Level set function in blue, and zero level set surface in yellow.

In this framework, at any time t, the front $\Gamma(t)$, implicitly defined by Equation 3.5, which shows that at each iteration, the new level set would be relocated at zero level again (called re-initialization). This is easily performed by recalculating the distance, $z = 0$, of every point from the contour, however it is computationally expensive.

$$\Gamma(t) = \{(x, y) | \phi(x, y, t = 0) = 0\} \tag{3.5}$$

Figure 3.3 illustrates the formation of level set function. It defines the propagating boundary/region as the zero level set, $\phi(x, y, t = 0)$, of a higher dimension on function $\phi(x, y, t)$, where t is time as the curve is evolving. The height (z axis) corresponds to the minimum distance from each point in a rectangular coordinate (image plane) from the contour C, based on the signed distance d from each point on (x, y) to the initial front, choosing a positive distance from outside the region and a negative direction from inside.

$\phi(x, t = 0)$ is required as the initial value (initialization) to start. Level set can be initialized automatically or semi-automatically in two or more phases depending on the decision of the user on how many different batches of segmentation are expected in an image. The two-phase level set method segments the image into two regions. Wherever three or four-phase level set methods exist, they can divide into three or four categories respectively

by applying two separate level set functions at the same time. By considering only one level set function in 3.4.a. the yellow region represents the level set front at $t = 0$ which is mapped to 3.4.b. on a contour on the 2D image. The inner parts of the contour represented with negative values which the decrease when they get farther from the zero level set and the outer points have positive value.

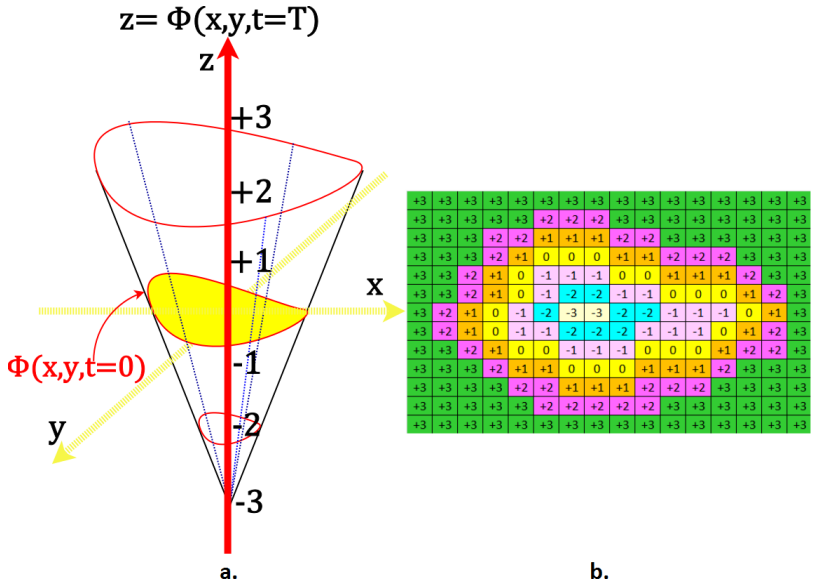

Figure 3.4: Level set and its mapping in image plane.

In order for the points to always move/ride on the edge of the interface, level set should be re-initialised to zero level in each iteration of movement, Equation 3.6.

$$\phi(x(t), y(t), t) = 0 \tag{3.6}$$

Since, the interface always corresponds to the place where $\phi = 0$, therefore outside of the edge $\frac{d\phi,t)}{dt} = 0$. For better understanding this, consider tracking a particle $\vec{x} = (x, y, z)$ on the surface in 3D over time:

$$\frac{d\phi(\vec{x}, t)}{dt} = 0 \tag{3.7}$$

from the chain rule, Figure 3.5 illustrates this:

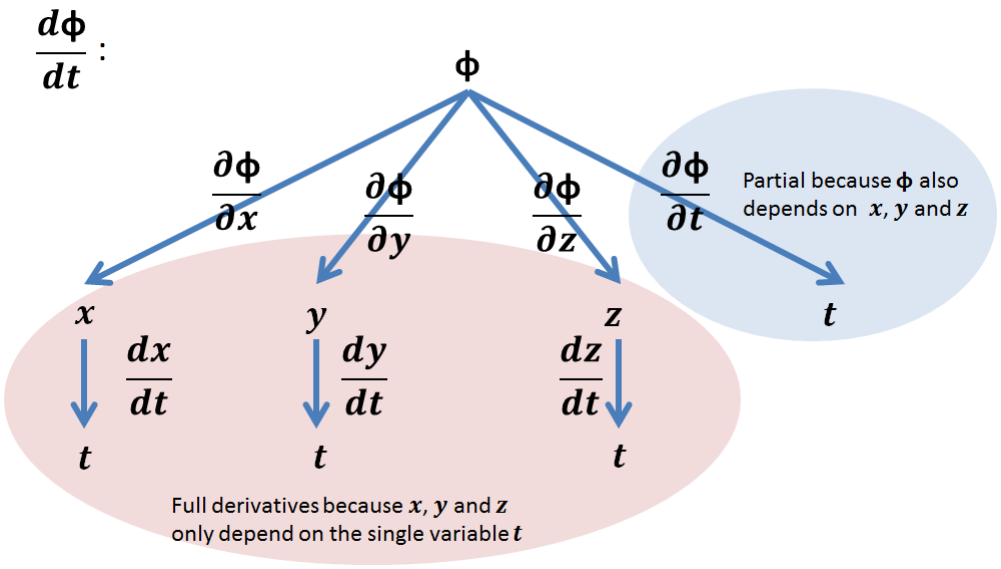

Figure 3.5: The chain rule demonstration of tracking a particle $\vec{x} = (x, y, z)$ on the surface in 3D over time.

then,

$$\frac{d\phi}{dt} = 0 \longrightarrow \frac{\partial \phi}{\partial x} \cdot \frac{dx}{dt} + \frac{\partial \phi}{\partial y} \cdot \frac{dy}{dt} + \frac{\partial \phi}{\partial z} \cdot \frac{dz}{dt} + \frac{\partial \phi}{\partial t} = 0 \tag{3.8}$$

when, the directional derivative of a function $\nabla f(x, y, z)$ is:

$$\nabla f = \frac{\partial f}{dx}\vec{x} + \frac{\partial f}{dy}\vec{y} + \frac{\partial f}{dz}\vec{z} \tag{3.9}$$

and the derivative of a vector $\vec{x} = (x, y, z)$ is:

$$\frac{d\vec{x}}{dt} = \frac{dx}{dt} + \frac{dy}{dt} + \frac{dz}{dt} \tag{3.10}$$

thus Equation 3.8 becomes:

$$\nabla \phi d\vec{x} + \frac{\partial \phi}{dt} = 0 \tag{3.11}$$

Since the signed distance of the level set at each point is required, therefore the surface normal at each point on the evolving front to its new position is necessary to be considered. $\frac{d\vec{x}}{dt}$ is also known as the speed function $\vec{F}$ that defines the speed of the level set function and how it evolves. It may also be written as $\vec{F}$, while it comprised of the normal and tangential components.

$$\vec{F} = F_N\vec{N} + F_T\vec{T} \tag{3.12}$$

As shown in Figure 3.6, F_N and F_T are scalar terms specifying the speed in the normal and tangential direction. The vector F is the sum of the normal F_N, and tangential F_T, $F = F_N + F_T$.

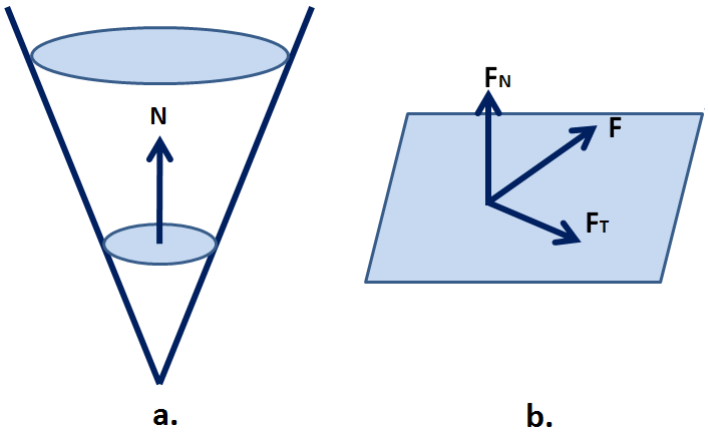

Figure 3.6: Specifying the speed in the normal and tangential direction of a. level set in 3D and b. a surface in 2D.

thus, 3.11 may be written as:

$$\frac{\partial\phi}{\partial t} + \nabla\phi \cdot \vec{F} = 0 \tag{3.13}$$

which is a linear partial differential equation. Expanding 3.13:

$$\frac{\partial\phi}{\partial t} + \nabla\phi(F_N\vec{N} + F_T\vec{T}) = 0 \tag{3.14}$$

As stated in [52], the tangential component has no effect, it vanishes into leading the scalar term F_N to only specify the speed function in the normal direction. Equation 3.14 thus becomes:

$$\frac{\partial\phi}{\partial t} + \nabla\phi V_N\vec{N} = 0 \tag{3.15}$$

also normal is the gradient scaled in unit length:

$$\vec{N} = \frac{\nabla\phi}{|\nabla\phi|} \tag{3.16}$$

substituting Equation 3.15 into Equation 3.16:

$$\frac{\partial \phi}{\partial t} + \nabla \phi F_N \frac{\nabla \phi}{|\nabla \phi|} = 0 \tag{3.17}$$

$$\frac{\partial \phi}{\partial t} + F_N \frac{\nabla \phi^2}{|\nabla \phi|} = 0 \tag{3.18}$$

replacing $\frac{\partial \phi}{\partial t}$ with ϕ_t, therefore:

$$\phi_t + F_N |\nabla \phi| = 0 \tag{3.19}$$

Re-initialization is repeated during evolution to prevent the occurrence of sharp corners and prevent flatness by calculating new ϕ values depending on the specified speed function. Therefore each iteration grows already knowing the old level set and the penalty value defined.

$$\phi(x,y,t+1) = \phi(x,y,t) + \Delta\phi(x,y,t) \tag{3.20}$$

Osher-Sethian designed the motion based on magnitude of the gradient and mean curvature flow, which solves the level set geometry problem as a PDE. Curvature plays the role of smoothing the level set to smooth the contours with the front symbolizing the boundary of the object when the propagation comes to a halt. The speed in the neighbourhood of the contour controls the motion of the front and should stop the propagation by tending towards zero at the limit of propagation. The speed is expressed as:

$$\frac{\partial \phi}{\partial t} = |\nabla \phi(x,y)|(\nu + \varepsilon k(\phi(x,y))) \tag{3.21}$$

where ν is a fixed parameter used to control the shrinkage or expansion and ε balances the regularity, robustness of evolution and $k(\phi(x,y))$ is the mean curvature of the level set function that stops leakage into small noisy parts. This can be calculated from:

$$k(\phi(x,y)) = div(\frac{\nabla \phi}{|\nabla \phi|}) = \frac{\phi_{xx}\phi_y^2 - 2\phi_x\phi_y\phi_{xy} + \phi_{yy}\phi_x^2}{(\phi_x^2 + \phi_y^2)^{3/2}} \tag{3.22}$$

where ϕ_x and ϕ_y represent the first-order PDEs of x and y respectively and ϕ_{xx} and ϕ_{yy} denote the second-order PDEs of each for the level set first function $\phi(x,y)$. This model is the initial representation of the level set presented by Osher-Sethian, which exploits information from the curvature to increase the performance of the stopping point of the growing contours. Computation time as well as parameter setting and adjustment are the key limitations of this model.

The Key advantages of level set are:

1. The process can be fully-automatic or semi-automatic.
2. They do not need parametrisation of the contour.
3. They are less sensitive to noise.
4. They are easily extendible to higher dimensions.
5. Level set methods can easily segment sharp corners and change topological structure (topological flexibility) during propagation [43].
6. Good numerical stability.

The growth of a level set is simple and can be listed as follows:

1. Initialization of the level set by initializing the front.
2. Calculating the level set force and growing model.
3. Iterate.
4. Matching the stopping criteria.

The differences between the various level set methods are mostly in the second step that will be explained and discussed in greater detail in the following sections.

3.3.1 Initialization

There are three main ways of initializing an active contour or level set:

1. Naive initialization.
2. Manual initialization.
3. Automatic initialization.

Naive initialization is when any random or simple geometric shape is chosen as the initial contour/boundary anywhere in the image. This method is easy and fast to initialize but it can result in lengthy convergence to the desired boundary and might take many iterations to calculate the proper segmentation. It can also converge to the wrong object in an image and lead to divergence. Manual initialization would be when the user chooses to initialize the contour or interior point manually. This model can be time-consuming and difficult for the user but is faster for propagation to reach the desired boundary. This model fails in high dimensional imagery because of the user's limitation in visualization. Automatic initialization can be performed in different ways, one major model is called centres of divergence (CoD) [53]. The other automated methods are force field segmentation (FFS) [54] and poisson inverse gradient (PIG) initialization [55]. In this thesis, the initialization models chosen are either naive or manual.

3.3.2 Parameter Setting

The parameter setting of each model defines a specific range for each parameter, therefore it is usually based on the model as well as the images used, each model presents different parameters for different images. Some evolutionary algorithms applied with level set for better parameter settings are based on genetic algorithm [56], particle swarm optimization [57], or ant colony optimization [58]. None of these methods can be used in this research due to lack of ground truth in medical images as well as their computational complexity on large data. Here the proposed parameter setting was mostly done by experimentation and comparison to the previous contours which was illustrated in Section 1.4 and will be explained further in Section 4.6.

3.4 Different Level Set Methods

Since its introduction, level set has developed in different categories and for different applications. These categories are discussed below.

3.4.1 Osher-Sethian Model

Geodesic Active Contours- In this model, first introduced by Caselles in 1997 [59], the level set stops at high-gradient locations by attenuating the speed and the propagation is faster at smooth locations. This is achieved by adding an addition term to Osher-Sethian's model, $g(|\nabla I|)$, which relates the speed term to the inverse of the gradient of the image. More formally:

$$\frac{\partial \phi}{\partial t} = |\nabla \phi| g(|\nabla I|)(div(\frac{\nabla \phi}{|\nabla \phi|}) + \nu) \tag{3.23}$$

where ν is always positive and,

$$g(|\nabla I(x,y)|) = \frac{1}{1+|\nabla G_\sigma(x,y) * I(x,y)|^2} \tag{3.24}$$

where G_σ is a Gaussian convolution filter with standard deviation σ.

Shape Modelling with Front Propagation- Maladi, Sethian and Vemuri in 1995, improved the early Osher-Sethian level set method by calculating the speed function based on the entropy-satisfying upwind finite difference and solving level set PDE function as a Hamilton-Jacobi type equation of motion [60]. In this model, the speed function's stopping criteria is a fulfilment of Osher-Sethian's method. In 2000, Leventon introduced a model based on a combination of prior shape information and level set methods [61].

The deformable shapes as well as the probability distribution were presented over the variances of a set of training shapes. At each iteration of the level set, an estimate is made based on prior shape information.

3.4.2 Region-Based Level Set

In the 1990s Chan-Vese developed Osher-Sethian's model by applying an energy minimization model instead of PDE, which allows automatic detection of interior contours [62, 63]. This is performed by using a piecewise constant and piecewise smooth optimal approximations proposed by Mumford-Shah [64]. They also proposed a two-phase level set method without edges that could segment the image into two regions and developed their model further to deal with vector-valued images, which performed robustly in the presence of noise. In 2002, they presented a multi-phase level set method that uses the log numbers of the level set function to separate n phases by using piecewise constant [65].

The Chan-Vese method shows that triple junctions and complex topologies can avoid vacuum and overlap in front propagation. This model assumes that in each level set region the intensity values are steady for all points. As a result it may not perform as well for objects with inhomogeneous intensities such as medical images. The model consists of two main components, which are minimal partition problems of Mumford-Shah and variational level sets. Mumford-Shah introduced an energy minimization method for segmentation [64]:

$$E^{MS}(u,C) = \int_{\Omega}(u-u_0)^2 d_x d_y + \mu \int_{\Omega\setminus C}|\nabla u|^2 d_x d_y + \nu|C| \tag{3.25}$$

Where μ and ν are positive weight values, C is the contour or closed subset in Ω and u is an approximation of the image u_0 in the optimal piecewise smooth shape. This model can be simplified by considering u as the piecewise constant function of c_i inside of each connected Ω_i ($\Omega = \bigcup_i \Omega_i \bigcup C$) and $c_i = mean(u_0)$ in Ω_0.

$$E(u,C) = \sum_i \int_{\Omega_i}(u_0 - c_i)^2 d_x d_y + \nu|C| \tag{3.26}$$

The problem of segmentation based on the Mumford-Shah model is that it is not easy to use due to the unknown value of C and also the problem is not convex.

Two-Phase Chan-Vese without Edges

Chan-Vese proposed the two-phase level set method without edges firstly. The main improvement in this version of the Chan-Vese method is the simplification of the energy functional which is based on the mean intensity values in each region of the level set (inside or outside in two-phase), c_1 and c_2, which are defined as:

$$c_1 = \frac{\int_\Omega (1 - H(\phi(x,y)))(I(x,y))d_x d_y}{\int_\Omega 1 - H(\phi(x,y))d_x d_y} \tag{3.27}$$

$$c_2 = \frac{\int_\Omega (H(\phi(x,y)))(I(x,y))d_x d_y}{\int_\Omega H(\phi(x,y))d_x d_y} \tag{3.28}$$

H is the Heaviside function,

$$H(x) = \begin{cases} 1 & \text{if } x \geq 0 \\ 0 & \text{otherwise} \end{cases} \tag{3.29}$$

At each iteration the values of c_1 and c_2 change and must be recalculated based on the level set of a new region to calculate a new speed function as:

$$\begin{aligned} F(c_1, c_2, \phi) = \quad & \int_\Omega (u_0 - c_1)^2 H(\phi) d_x d_y \\ & + \int_\Omega (u_0 - c_2)^2 (1 - H(\phi)) d_x d_y \\ & + \int_\Omega |\nabla H(\phi)| \end{aligned} \tag{3.30}$$

The Chan-Vese level set evolution equation is as follow where δ represents a one-dimensional Dirac function.

$$\frac{\partial \phi}{\partial t} = \delta(\phi)[\nu div(\frac{\nabla \phi}{|\nabla \phi|}) - (u_0 - c_1)^2 + (u_0 - c_2)^2)] \tag{3.31}$$

One of the benefits of this model is that the initialization is based on characteristics of the region. However it is not stable for the inhomogeneous images and the necessary re-initialization makes it computationally expensive.

Vector-Valued Image Chan-Vese Method

In this model, Chan-Vese extended the two-phase method to a vector-valued image in 2000 [63]. This model is widely used in colour imaging and video imaging for motion of objects and texture images.

$$\begin{aligned} F(c^+, c^-, \phi) = \quad & \mu.L \\ & + \int_{inside(C)} \frac{1}{N} \sum_{i=1}^{N} \lambda_i^+ |u_{0,i} - c_i^+|^2 dxdy \\ & + \int_{outside(C)} \frac{1}{N} \sum_{i=1}^{N} \lambda_i^- |u_{0,i} - c_i^-|^2 dxdy \end{aligned} \tag{3.32}$$

and the PDE is:

$$\begin{aligned} \frac{\partial \phi}{\partial t} = \quad & \delta_\varepsilon [\mu.div \frac{\nabla \phi}{|\nabla \phi|} \\ & - \frac{1}{N} \sum_{i=1}^{N} \lambda_i^+ |u_{0,i} - c_i^+|^2 dxdy \\ & + \frac{1}{N} \sum_{i=1}^{N} \lambda_i^- |u_{0,i} - c_i^-|^2 dxdy] \end{aligned} \tag{3.33}$$

where λ^+ and λ^- are weighting parameters and c_i^+ and c_i^- are the mean value of i^{th} component of the vector image inside and outside of the contours. The advantage of this model is its ability to converge on edges with or without significant gradient. [27, 66, 67].

Multi-Phase Chan-Vese without Edges

Chan-Vese extended the two-phase method to a multi-phase method by using n level sets to segment 2^n regions in an image [65]. Figure 3.7 and the following equations demonstrate this model for four-phase which consist of two level sets. They are initialized separately but the same level set function is applied for both initializations. The mapping plane shows this growth concept in four-phase clearly.

$$
\begin{aligned}
F(c,\phi) = \quad & \int_{\Omega}(u_0-c_{11})^2 H(\phi_1)H(\phi_2)d_xd_y \\
& + \int_{\Omega}(u_0-c_{10})^2 H(\phi_1)(1-H(\phi_2))d_xd_y \\
& + \int_{\Omega}(u_0-c_{01})^2 (1-H(\phi_1))H(\phi_2)d_xd_y \\
& + \int_{\Omega}(u_0-c_{00})^2 H(\phi_1)(1-H(\phi_2))d_xd_y \\
& + \int_{\Omega}|\nabla H(\phi_1)| \\
& + \int_{\Omega}|\nabla H(\phi_2)|
\end{aligned}
\tag{3.34}
$$

$$
\begin{aligned}
c_{11} &= mean(u_0) \in \{(x,y) : \phi_1(t,x,y) > 0, \phi_2(t,x,y) > 0\} \\
c_{10} &= mean(u_0) \in \{(x,y) : \phi_1(t,x,y) > 0, \phi_2(t,x,y) < 0\} \\
c_{01} &= mean(u_0) \in \{(x,y) : \phi_1(t,x,y) < 0, \phi_2(t,x,y) > 0\} \\
c_{00} &= mean(u_0) \in \{(x,y) : \phi_1(t,x,y) < 0, \phi_2(t,x,y) < 0\}
\end{aligned}
\tag{3.35}
$$

Therefore,

$$
\begin{aligned}
\frac{\partial \phi_1}{\partial t} = \quad & \delta(\phi_1)[\nu div(\frac{\nabla \phi_1}{|\nabla \phi_1|}) \\
& - \Big((u_0-c_{11})^2 + (u_0-c_{01})^2)\Big)H(\phi_2) \\
& + \Big((u_0-c_{10})^2 + (u_0-c_{00})^2))\Big)(1-H(\phi_2))]
\end{aligned}
\tag{3.36}
$$

$$
\begin{aligned}
\frac{\partial \phi_2}{\partial t} = \quad & \delta(\phi_2)[\nu div(\frac{\nabla \phi_2}{|\nabla \phi_2|}) \\
& - \Big((u_0-c_{11})^2 + (u_0-c_{01})^2)\Big)H(\phi_1) \\
& + \Big((u_0-c_{10})^2 + (u_0-c_{00})^2))\Big)(1-Hs(\phi_1))]
\end{aligned}
\tag{3.37}
$$

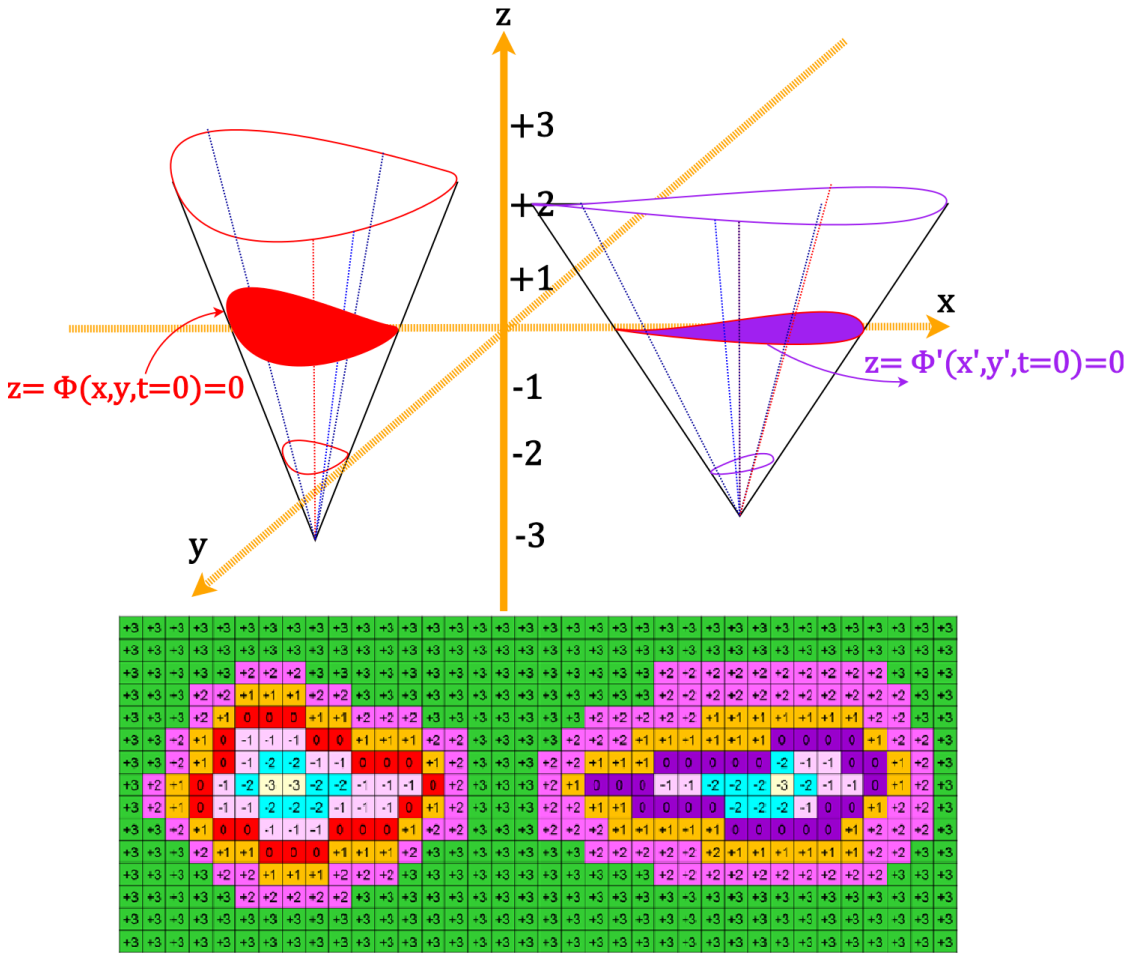

Figure 3.7: Multi-phase level set and its mapping in image plane.

Other Chan-Vese Based Methods

Zhang improved the Chan-Vese method by replacing magnitude of gradient instead of image intensity as the evolution term [68].

$$\frac{\partial \phi}{\partial t} = \delta_\varepsilon(\phi)(I' - \frac{u+v}{2}) \tag{3.38}$$

later Zhang further improved his model and defined the energy function as [69]:

$$\frac{\partial \phi}{\partial t} = \frac{\alpha \delta_\varepsilon(\phi)(I' - \frac{u+v}{2})}{\max|I' - \frac{u+v}{2}|} \tag{3.39}$$

Zhang [70] proposed a local image fitting model by considering image local characteristics to improve the Chan-Vese method, more advanced than local binary fitting introduced by Li [71]. To prevent re-initializations at each iteration, Zhang used a Gaussian smoother to regularize the level set function. In this work, the local fitted image fitting function is defined:

$$I^{LIF} = m_1 H_\varepsilon(\phi) + m_2(1 - H_\varepsilon(\phi)) \tag{3.40}$$

$$m_1 = mean(I \in (x \in \Omega | \phi(x) > 0 \cap W_k(x))) \tag{3.41}$$

$$m_2 = mean(I \in (x \in \Omega | \phi(x) < 0 \cap W_k(x))) \tag{3.42}$$

where $W_k(x)$ is the rectangular window filter, e.g., a constant window.

$$E^{LIF} = \frac{1}{2}\int_\Omega |I(x) - I^{LIF}(x)|^2 dx, dx \in \Omega \tag{3.43}$$

Liu [72] improved the Chan-Vese method by considering the local characteristic named local region-based Chan-Vese designed for inhomogeneous images. The Energy function is designed as:

$$\begin{aligned} E^{LBF}(\phi, f_1(x), f_2(2)) = \quad & \lambda_1 \int_\Omega \int_\Omega g(x-y)(I(y) - f_1)^2 H(\phi(y))\, dy\, dx \\ & + \lambda_2 \int_\Omega \int_\Omega g(x-y)(I(y) - f_1)^2 H(\phi(y))\, dy\, dx \\ & + \mu \int_\Omega \delta(\phi(x)) |\nabla \phi(x)|\, dx \\ & + \nu \int_\Omega \frac{1}{2}(|\nabla \phi(x)| - 1)\, dx \end{aligned} \tag{3.44}$$

$$f_1(x) = \frac{\int_\Omega g_k(x-y)(H(\Phi(x,y)))(I(x,y))d_x d_y}{\int_\Omega g_k(x-y) H(\Phi(x,y)) d_x d_y} \tag{3.45}$$

$$f_2(x) = \frac{\int_\Omega g_k(x-y)(1 - H(\Phi(x,y)))(I(x,y))d_x d_y}{\int_\Omega g_k(x-y)(1 - H(\Phi(x,y)) d_x d_y)} \tag{3.46}$$

where $f_1(x)$ and $f_2(x)$ are the image approximate intensity means inside and outside the contour C and g represents the Gaussian Kernel filters.

Xiao-Feng Wanga [73] introduced a local Chan-Vese (LCV) consisting of three terms: global, local and regularizer.

$$\begin{aligned} E^{LCV} = \quad & \alpha \cdot E^G + \beta \cdot E^L + E^R \\ & = \alpha \int_{(inside(C))} |I - c_1|^2 \, dxdy \\ & + \alpha \int_{(outside(C))} |I - c_2|^2 \, dxdy \\ & + \beta \int_{(inside(C))} |g_k * I - I - d_1|^2 \, dxdy \\ & + \beta \int_{(outside(C))} |g_k * I - I - d_2|^2 \, dxdy \end{aligned} \tag{3.47}$$

where E^G is the global energy, E^L is the Local, E^R represents the regularizing term, g_k is the averaging convolution operator and d_1 and d_2 are the approximate intensity means inside and outside of the contour with respect to the difference image, $g_k * I - I$.

Lankton and Tannenbaum proposed a new robust region based segmentation model using level set which considers local rather than global statistical characteristics [74]. This model shows a great improvement in the case of inhomogeneous images.

$$\begin{aligned} E(\phi) = \quad & \int_{\Omega_x} \delta\phi(x) \int_{\Omega_y} \beta(x,y).F(I(y),\phi(y))d_x d_y \\ & + \lambda \int_{\Omega_x} \delta(\phi(x))||\nabla\phi(x)||d_x \end{aligned} \tag{3.48}$$

where,

$$\beta(x,y) = \begin{cases} 1 & \text{if } ||x-y|| \leq r \\ 0 & \text{otherwise} \end{cases} \tag{3.49}$$

therefore,

$$\begin{aligned} \frac{\partial\phi}{\partial t}(x) = \quad & \delta\phi(x) \int_{\Omega_y} \beta(x,y).\nabla\phi(y)F(I(y),\phi(y))d_y \\ & + \lambda\,\delta\phi(x) div\left(\frac{\nabla\phi(x)}{|\nabla\phi(x)|}\right) \end{aligned} \tag{3.50}$$

The authors compared their model with three other region based level set methods and demonstrated an improvement with their algorithm, the other models compared were uniform modelling energy as introduced by Chan-Vese [62], the means separation energy by Yezzi and Tannenbaum [75] and the histogram separation energy by Michailovich and Tannenbaum [76].

Pereyra and McLaughlin exploited information theory to define the Riemannian structure of the statistical manifold associated with the Chan-Vese active contour [77]. They used the Fisher information matrix to form the natural gradient metric of the statistical mani-

fold which converges much faster than the Euclidean gradient descent algorithm. In this algorithm, they defined log-likelihood for information geometry.

$$\begin{aligned} log(p(I;\phi)) = \quad & -\Sigma_{i=1}^{N}\frac{1}{2}(I_i-c_1)^2H(\phi_i) \\ & -\Sigma_{i=1}^{N}\frac{1}{2}(I_i-c_2)^2H(-\phi_i) \\ & -\frac{N}{2}log(2\pi) \end{aligned} \tag{3.51}$$

The natural gradient matrix is defined as:

$$G_\varepsilon(\phi)_{(i,j)} = |\delta'_\varepsilon(\phi_i)|(c_1-c_2)^2\text{if i=j and 0 otherwise} \tag{3.52}$$

where $\delta'_\varepsilon(x) = \frac{-2\varepsilon x}{\pi(\varepsilon^2+x^2)^2}$, therefore the re-initializer is based on:

$$\phi^{t+1} = \phi^t + \eta^t H G_\varepsilon^{-1}(\phi^t)\delta_\varepsilon(\phi^t)((I_i-c_1)^2-(I_i-c_2)^2) \tag{3.53}$$

where η^t is the time step at iteration t and H is the spatial smoothing operator of Hessian. For convergence they used the difference between energy functional of each iteration and the previous one.

In 2012, Yuan represented L^2+ Soblev gradient to improve the Chan-Vese method for calculating the energy function. This work presents the L^2 gradient for minimizing external energy and Soblev gradient for the internal energy which represents length of curve and produces the result in one iteration [78].

In 2008, Cheng proposed a model based on the Chan-Vese level set method that uses shape prior knowledge for liver segmentation [79]. A training set for prior shape is computed based on statistical models and in contrast to the previous shape prior of models this model allows the prior shape to be scaled, rotated or translated by applying an affine transformation. In general shape prior knowledge enables the process to be speeded up due to detecting the location of tumour/object first followed by measurement of the intensity values.

Bernard introduced a continuous representation of a level set based on B-Spline on medical images [80].

Shi introduced a fast two-cycle algorithm for the approximation of level-set-based curve evolution [81].

In 2001, Droskey [82], presented a multi-grid level set method for 3D medical image processing. By applying inter-active modulation for the speed function this model can

deal with non-sharp boundaries.

In 2011, Bara [83], used variational models for solving level set based on Mumford-Shah and level set methods. Also, Samir applied Dempster-Shafer theory for a surface convolution model to overcome the problem of topology of front prorogations in Mumford-Shah and level set methods. This model is very much dependent on initial contour and the convergence may not be fast in terms of compute time.

In 2003, Ho introduced a software package for level set by applying gradient based and region competition level set methods [84].

In 2003, Lefohn et al [85], proposed a fast level set algorithm based on GPUs which enables the user to tune the parameters while solving the PDE of level set to control the shape of model during evolution in real time.

In 2004, Lin [86], introduced a new model based on a new speed function. Using the image region intensity instead of the gradient value. The idea behind this model is to find the intensity range that classifies the tissue type. Leakage, which happens in the presence of connected components, is prevented in this model by the smoothness of the propagating surface. This model prevents topology changes and overlaps via the smooth evolving contour.

In 2008, Cao [87], presented a new energy functional for variational level set approach for SAR images that take account of speckle noise statistical in the energy functional. Segmentation is based on minimization of the energy functional via level set which is suitable for SAR images due to their characteristics.

In 2010, Zhang, [88] developed a variational multi-phase level set for segmenting boundaries on MR images. The process of this model is to find the intensity values based on different Gaussian distributions which vary in means and variances, and transforms the result to other dimensions by using a sliding window to resist the overlap of different tissues. In the new domain, Zhang defined the maximum likelihood for each point, which unified in the whole domain to construct the variational level set evolution.

In 2010, El Hadji, [89], introduced a variational and shape based level set in medical images. This work considers firstly a penalty factor to push the level set to reach a signed distance function that prevents the re-initialization process. A Hausforff measure is also applied to improve visualization of the boundaries and shape. This is followed by a weighted area term for fast convergence/growth of the level set contour based on Mumford-Shah functional energy.

3.4.3 Snake-Based Level Set Methods

Li developed an edge based level set method based on gradient flow for solving the inhomogeneity in intensity, which previous methods had difficulty solving [71, 90, 91]. This model uses the energy minimization technique, similar to the Snake model, by reducing the fitting energy in image segmentation. This energy is:

$$E(\phi) = \mu P(\phi) + \lambda L(\phi) + \nu A(\phi) \tag{3.54}$$

where,

$$P(\phi) = \int_{\Omega} \frac{1}{2}(|\nabla\phi| - 1)d_x d_y \tag{3.55}$$

$$L(\phi) = \int_{\Omega} g(I)\delta(\phi)|\nabla(\phi)|d_x d_y \tag{3.56}$$

$$A(\phi) = \int_{\Omega} g(I)H(-\phi)d_x d_y \tag{3.57}$$

and

$$g(I) = \frac{1}{1 + |\nabla G^{\sigma} * I|^p}, p \geq 1 \tag{3.58}$$

$P(\phi)$ is a penalty term in the energy functional that is used to level set periodical during evolution. The stopping operator, g is based on a Gaussian Kernel that forces the level set to converge to zero when approaching the edges. σ is the standard deviation, L represents the length of the contour with respect to the stopping operator of g as its weight and A is the speed controller of the evolution which makes the contour to shrink if the ν is positive and tends to expand when the ν is negative.

The level set PDE function in this model is based on the Gateaux derivative which is:

$$\frac{\partial\phi(x,y)}{\partial t} = -\frac{\partial E}{\partial\phi} \tag{3.59}$$

This equation can be expanded further as:

$$\begin{aligned} \frac{\partial E}{\partial\phi} = \quad & -\mu(\Delta\phi - div(\frac{\nabla\phi}{|\nabla\phi|})) \\ & -\lambda\delta(\phi)div(g(I)\frac{\nabla}{\phi}|\nabla\phi|) \\ & -\nu g\delta(\phi) \end{aligned} \tag{3.60}$$

therefore,

$$\begin{aligned}\frac{\partial \phi}{\partial t} = \quad & \mu(\Delta\phi - div(\frac{\nabla\phi}{|\nabla\phi|})) \\ & + \lambda\delta(\phi)div(g(I)\frac{\nabla}{\phi}|\nabla\phi|) \\ & + \nu g\delta(\phi)\end{aligned} \tag{3.61}$$

where μ is the penalizing coefficient, λ is the coefficient for length and ν refers to the area. The ratio of λ and ν defines the stopping point of level set evolution because both of these terms contain edge information. The length term keeps the contour tight and the area helps the expansion of the contour.

Geodesic active contours, introduced by Kichenassamy [75] and Caselles [59] are based on Snake. In these models, the speed function is calculated by applying minimal distance curves in a Riemannian space derived from the image. Given an image, I, and for a given differentiable curve, $C(p), p \in [0,1]$, they define the energy as:

$$E(C) = \int_0^1 g(|\nabla I(C(p))|)|C^{'}(p)|dp \tag{3.62}$$

The PDE functional calculated via derivation of the Euler-Lagrange system is therefore:

$$\frac{\partial C}{\partial t} = g(|\nabla I|)\kappa\vec{N} - (\nabla g(|\nabla I|).\vec{N})\vec{N} \tag{3.63}$$

Threshold Level Set, Taheri applied a threshold level set method for brain tumour segmentation in 3D which does not depend on density function estimation by using a global threshold for the speed function [33]. This semi-automatic model requires a user's input to initialize the threshold value for the level set based on information from a region inside a tumour. For convex tumours, a spherical surface is chosen as the initial level set located in the middle of the tumour. For concave tumours several spheres are required due to the complexity of the shape. The threshold updates at every iteration during the evolution which should decrease as it gets closer to the boundaries while the contrast between tumour (foreground object) and non-tumour (background) is increasing. The threshold in this model can be calculated based on

$$T_{i+1} = \widehat{\mu}_i - k\widehat{\sigma}_i, i \geq 0 \tag{3.64}$$

$$\widehat{\mu}_i = \frac{1}{n}\sum_{j=1}^{n} x_{ij} \tag{3.65}$$

$$\widehat{\sigma}_i = \frac{1}{n-1}\sum_{j=1}^{n} (x_{ij} - \widehat{\mu}_i)^2 \tag{3.66}$$

In this model T_{i+1} is the threshold which is approximated in each iteration of $(i+1)^{th}$ based on a tailed confidence interval, k represents the confidence level, μ and σ are mean and standard deviation respectively and n is the number of samples (x_{ij}) up to the i^{th} iterations [33]. Therefore, Taheri's level set PDE is:

$$\frac{\partial \phi(x,y,t)}{\partial t} + F(x,y,t)\|\nabla \phi(x,y,t)\| = 0 \tag{3.67}$$

$$F = F_0 \cdot F_I^{(i)} - \varepsilon k_\phi \tag{3.68}$$

where F_0 is the constant propagation determined by a positive number and $F_I^{(i)}$ is based on image characteristics in the $(i+1)^{th}$ iteration. Propagation stops when a boundary is reached. k_ϕ is the smoothness parameter. The threshold level set specifies the F_I for each sample based on the diversity between the threshold values. Therefore, the larger diversity leads to faster propagation/speed.

$$F_I^i(x,y,z) = \frac{\Delta}{2}[\frac{1+sgn(\Delta)}{max(\Delta)} - \frac{1-sgn(\Delta)}{min(\Delta)}] \tag{3.69}$$

where Δ is equal to $I(x,y,z)$ and sgn represents the sign function which defines whether the speed function of F_I^i is inside or outside of the tumour and classed as positive or negative respectively for initializing the level set. This process tends to stop near the boundary of tumours when threshold variation becomes negligible.

The Table 3.2 summarizes the discussed papers using level set in this chapter. In Chapter 4 it would be better discussed the selection of level set models for this research.

Published on	Author(s)	Paper	Specification	Pros and Cons
1987	Kass	[41]	snake as an active contour to improve image segmentation.	locks into edges and lines by getting advantage of image forces.
1988	Osher-Sethian	[42]	level set method was introduced to improve snake by adding another dimension to get implicit information of the curve.	level set can detect sharp corners, break apart, and merge together the interfaces which snake was failed.
1997	Caselles	[59]	this method has the advantage of geodesics or minimal distance curves in a Riemannian space to improve Sethian's level set model by adding a new term to the curve evolution.	Better detection of boundaries with large differences in their gradient as well as less dependency to parameter setting.
1995	Kichenassamy	[75]	modified version of snake on gradient flows relative to specific new feature-based Riemannian metrics.	good convergence based on the desired features that lie at the bottom of a potential well.
1999	Chan-Vese	[62]	simplified the leve set energy functional based on mean intensity values using curve evolution of Mumford-Shah functional.	this model detects the boundaries which are not necessarily defined by the gradient.
2000	Leventon	[61]	this model uses the prior information about the intensity and curvature from a training set of images and boundaries while the curvature acts as a regularization term.	this model can take longer time of convergence as at each iteration of the level set, an estimate is made based on prior shape information.
2001	Droskey	[82]	presented a multi-grid level set method for 3D medical image processing.	this model is capable of handling with non-sharp boundaries well.

2003	Ho	[84]	Introduced a software package for level set by applying gradient based and region competition level set methods.	a great guidance for the clinicians and speeds over any manual segmentation.
2003	Lefohn et al	[85]	a new level set model based on interactive rates on commodity graphics cards (GPUs) for medical image segmentation.	this model provides the user immediate feedback on the parameter settings and let the user to tune them separately in real time.
2004	Lin	[86]	a new level set model based for medical image segmentation on new speed function by considering the region intensity information, instead of the image gradient information.	the proposed speed function governs the deformation of interface.
2008	Zhang	[68]	improved the Chan-Vese method by replacing magnitude of gradient instead of image intensity in medical image applications.	this model is mainly designed for special surgery instruments in CT images for minimal invasive spinal surgery.
2008	Li	[71]	a new model was designed based on region-based snake model which draws the intensity information in local regions at a controllable scale.	this model can overcome the difficulties caused by intensity inhomogeneities
2008	Lankton	[74]	a new model using level set which considers local rather than global statistical characteristics.	this model shows a great improvement in the case of inhomogeneous images.
2008	Shi	[81]	Introduced a fast two-cycle algorithm for the approximation of level-set-based curve evolution.	suitable for real-time implementation.

2008	Cao	[87]	a new energy functional used for variational level set approach for SAR images by considering the statistical model of speckle noise.	accurately and automatically extracts the regions of interest in SAR images.
2008	Cheng	[79]	a new model based on Chan-Vese level set model which developed an algorithm based on shape prior knowledge for liver MR imaging segmentation.	this model improved liver segmentation and can be refined liver perfusion curve without respiration affection.
2009	Bernard	[80]	introduced a continuous representation of a level set based on B-Spline on medical images.	the smoothness in this model can be explicitly controlled via the chosen B-spline kernel.
2010	Zhang	[88]	used a variational multi-phase level set in medical imaging.	tissue segmentation and bias correction are simultaneously achieved via a level set evolution process.
2010	El Hadji	[89]	a variational and prior shape based level set in medical images by less reâĂŘinitialization due to considering a penalization term that forces the level set to be close to a signed distance function (SDF).	this model detects tumour boundaries in medical imaging while they are not silent and it performs well in both prior and nonâĂŘprior shape based image segmentation.
2010	Wang	[73]	a new Chan-Vese model which formed based on the techniques of curve evolution, local statistical function and level set method.	good segmentation performance on images with intensity inhomogeneity.

2010	Zahng	[70]	this model introduces a new local image fitting (LIF) energy to use the image local information of the image for the application in inhomogeneous images.	more computationally efficient than Li model in local binary fitting (LBF) energy.
2010	Taheri	[33]	a threshold level set method for brain tumour segmentation in 3D which does not depend on density function estimation by using a global threshold for the speed function.	better performance compared to region-competition based method.
2011	Bara	[83]	using variational models for solving level set based on Mumford-Shah and level set methods.	this model is independent to the digital image grids.
2012	Yuan	[78]	this model uses Soblev gradient to improve Chan-Vese model for calculating the internal energy.	computationally more efficient than its traditional models.
2012	Liu	[72]	improved the Chan-Vese method by considering the local characteristic named local region-based Chan-Vese.	effectiveness and robustness on images with intensity inhomogeneity.
2013	Pereyra	[77]	Exploited information theory to define the Riemannian structure of the statistical manifold associated with the Chan-Vese active contour.	very fast convergence compared to any other level set model.

Table 3.2: Comparison of different relevant level set works.

3.5 Texture Analysis

Texture can be considered to be repeating patterns of local variation of pixel intensities. Generally, texture analysis is used to measure different features in an image such as roughness, smoothness, or variations of intensity of different parts which are result of the physical surface properties. Texture analysis plays a very important role in image classification, segmentation, compression, feature extraction and shape reconstruction from texture. Figure 3.8 shows some repeated patterns in different objects which shows the concept of texture.

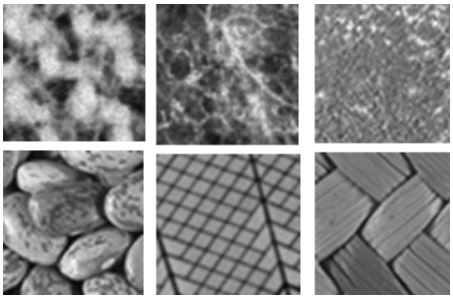

Figure 3.8: Different examples of some textured surfaces [92].

The repeated patterns are considered to be related to each other. They present the same region/object and can help in finding the relationship of pixels. Texture analysis can be grouped as geometrical, statistical, model based and signal processing (transformation) methods. In this thesis, texture analysis was used as a pre-segmentation aid to improve the region of interest before applying the main segmentation model based on the level set. Both first and second-order based features were used which are explained in the following subsections although second-order statistical models were chosen finally for the proposed model in this thesis.

In medical imaging the texture of healthy tissues should be different from the cancerous tissues while the texture should change during the course of treatment during the changes happening. Therefore texture analysis can be a great indicator of tracking changes of images during treatment to be compared with each other. As first-order statistical models lack the special information, therefore second-order statistics using gray-level co-occurrence matrix (GLCM) would be a great indicator of changes in respect to the pixel position.

3.5.1 First-Order Statistical Models

These models are histogram intensity based features to analyse the statistical information contained in the image. They are are calculated by having the probability density of the intensity levels in the image. Central moments such as mean, variance, skewness and Kurtosis are the main texture features in first-order models. Energy and entropy are also two other popular models in this range. Although first-order features can be easily calculated, they are of great value in texture analysis. Their disadvantage compared to second-order features however, is that they do not convey any information regarding the position of pixels with respect to others. The features used in this thesis are:

Local Range

The local range of an image simply calculates the range of variation in the neighbourhood locally around the pixel. It is the difference between maximum and minimum in the neighbourhood.

$$R = max(x) - min(x) \tag{3.70}$$

Local Standard Deviation

This method is also very similar to local range; it calculates the standard deviation throughout the whole neighbourhood. It quantifies the amount of variation of the image.

$$\sigma = \sqrt{\frac{1}{N}\sum_{i=1}^{N}(x_i - \mu)^2} \tag{3.71}$$

where N is the neighbourhood size and μ is the mean value:

$$\mu = \frac{1}{N}\sum_{i=1}^{N} x_i \tag{3.72}$$

Entropy

First-order entropy calculates the degree of disorder or lack of predictability of a pixel in an image.

$$H(x) = -\sum_{i} p(i) log(p_x(i)) \tag{3.73}$$

where x is the pixel neighbourhood , $p(i)$ is the probability of pixel i^{th} of x. The more the possibility of the occurrence of a pixel, increases logarithmically with higher values of intensity.

3.5.2 Second-Order Statistical Models

The second-order histogram is defined as a GLCM proposed by Haralick in 1979 is a statistical method that is used to calculate second-order texture features. These second-order methods use two pixels to estimate the image properties where first-order ones were using only one. These models calculate spatial relationships based on the number of occurrences of two pixels relative to each other in specific directions. In other words, GLCM represents the distance and angular spatial relationship in an image/sub-image. Each value can occur either horizontally, vertically or diagonally to adjacent pixels.

GLCM scales the intensity values to a number of gray-levels. The number of gray-levels should be integers, for example two for binary images or eight for numeric. Eight gray-levels limit the pixel intensity values from one to eight by normalising them between their minimum and maximum values. Also considering different offsets (distance and direction) between the pixel of interests can results in different GLCMs.

Figure 3.9 shows the array offsets of [0 1; -1 1; -1 0; -1 -1], which refers to distance one between two pixels in only one direction (not symmetric). If it is symmetric, it considers back and forth directions.

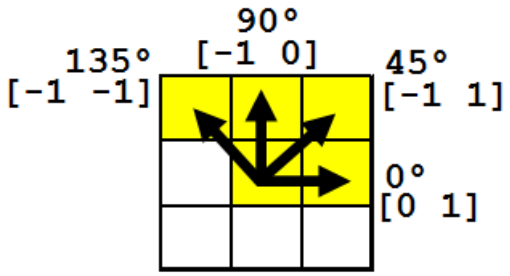

Figure 3.9: GLCM offsets.

Haralick Features

In this part, fourteen Haralick features are explained briefly, where:

$p(i,j)$ is $(i,j)^{\text{th}}$ entry in a normalized gray-tone spatial-dependence matrix, $= \frac{P(i,j}{R})$. $p_x(i)$ is ith entry in the marginal-probability matrix obtained by summing the rows of $p(i,j)$, $= \sum_{j=1}^{N_g} P(i,j)$ and N_g is the number of distinct gray levels in the quantized image respectively.

F1. Angular Second Moment

$$f_1 = \sum_i \sum_j \{p(i,j)\}^2 \tag{3.74}$$

F2. Contrast

$$f_2 = \sum_{n=0}^{N_{g-1}} \{ \sum_{|i-j|=n}^{N_g} \sum_{i=1}^{N_g} \sum_{j=1} (p(i,j)) \} \tag{3.75}$$

F3. Correlation

$$f_3 = \frac{\sum_i \sum_j (ij) p(i,j) - \mu_x \mu_y}{\sigma_x \sigma_y} \tag{3.76}$$

where μ_x,μ_y, σ_x and σ_y are the means and standard deviations of p_x and p_y, respectively.

F4. Variance

$$f_4 = \sum_i \sum_j (i-\mu)^2 p(i,j) \tag{3.77}$$

F5. Inverse Difference Moment

$$f_5 = \sum_i \sum_j \frac{1}{1+(i-j)^2} p(i,j) \tag{3.78}$$

F6. Sum Average

$$f_6 = \sum_{i=2}^{2N_g} i p_{x+y}(i) \tag{3.79}$$

F7. Sum Variance

$$f_7 = \sum_{i=2}^{2N_g} (i-f_8)^2 p_{x+y}(i) \tag{3.80}$$

F8. Sum Entropy

$$f_8 = -\sum_{i=2}^{2N_g} p_{x+y}(i) log(p_{x+y}(i)) \tag{3.81}$$

F9. Entropy

$$f_9 = -\sum_i \sum_j p(i,j) log(p_{x+y}(i)) \tag{3.82}$$

F10. Difference Variance

$$f_{10} = \text{variance of} p_{x+y} \tag{3.83}$$

F11. Difference Entropy

$$f_{11} = -\sum_{i=0}^{N_{g-1}} p_{x-y}(i) log(p_{x-y}(i)) \tag{3.84}$$

F12 and F13. Information measures of Correlation

$$f_{12} = \frac{HXY - HXY1}{max\{HX, HY\}} \tag{3.85}$$

$$f_{13} = (1 - exp[-2.0(HXY2 - HXY)])^{0.5} \tag{3.86}$$

$$HXY = -\sum_i \sum_j log(p(i,j)), (HX \text{ and } HY \text{ are entropies of } p_x \text{ and } p_y) \tag{3.87}$$

$$HXY1 = -\sum_i \sum_j p(i,j) log(p_x(i) p_y(j)) \tag{3.88}$$

$$HXY2 = -\sum_i \sum_j p_x(i) p_y(j) log(p_x(i) p_y(j)) \tag{3.89}$$

F14. Maximal Correlation Coefficient

$$f_{13} = (\text{second largest eigenvalue of Q})^{0.5} \tag{3.90}$$

$$Q(i,j) = \sum_k \frac{p(i,k) p(j,k)}{p_x(i) p_y(k)} \tag{3.91}$$

Figure 3.10.a illustrates calculating GLCM by considering only one direction offset [0 1], which only takes the right adjacent pixel into account. GLCM(1,1) refers to the number of occurrence of (1,1), when number 1 is the right adjacent to any pixel carries value 1 itself in the whole scaled image which resulted three occurrences.

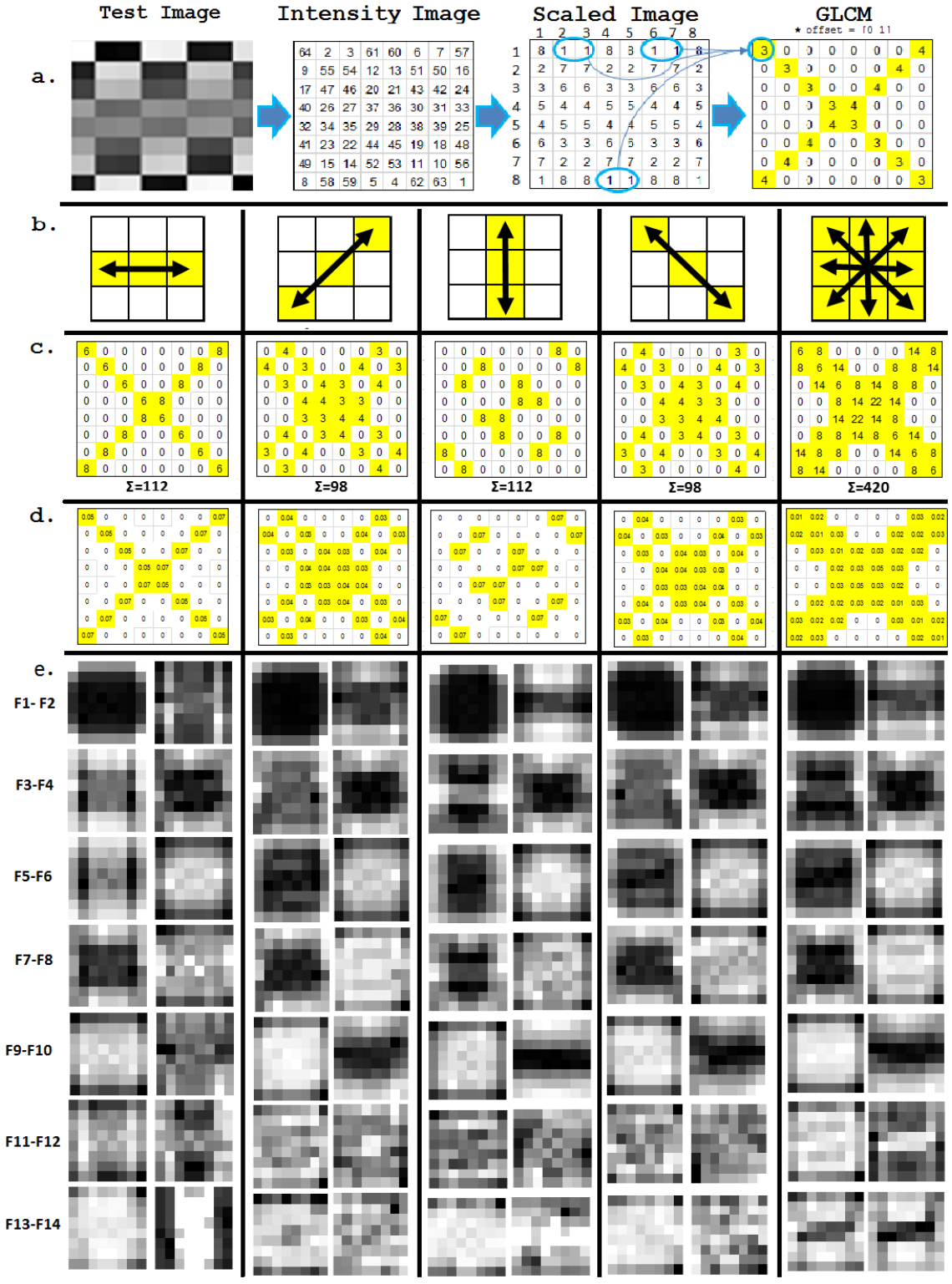

Figure 3.10: Example for calculating the GLCM by using 8 gray-levels: a. a randomly generated test image b. symmetric offsets, from left to right [0 1], [-1 1] [-1 0],[-1 -1] and all, c. calculated GLCM with respect to their above offsets, Σ refers to the sum of the elements (zero entries are marked in white and the highest value of each matrix is marked in yellow), d. normalized GLCM and e. fourteen texture features in Section 3.5.2 based on each GLCM in row b, F1: angular second moment, F2: contrast, F3: correlation, F4: variance, F5: inverse difference moment, F6: sum average, F7: sum variance, F8: sum entropy, F9: entropy, F10: difference variance, F11: difference entropy, F12 and F13: information measures of correlation, F14: maximal correlation coefficient.

Figure 3.10.b shows 5 different symmetric offsets, from left to right [0 1], [-1 1] [-1 0],[-1 -1], all and their relevant GLCMs are shown in Figure 3.10.c while Figure 3.10.d displays their relevant normalized GLCM. Figure 3.10.e illustrates the results of all fourteen Haralick features of the test image in Figure 3.10.a based on the calculated probability matrix in 3.10.d In Figure 3.10.c, the zero entries are marked in white and the highest value of each matrix is marked in yellow, it shows that calculations in single directions lead to sparse matrices compared to all directions. For example, considering contrast textured image for the sample image in 3.10.a with respect to the GLCMs in 3.10.c, it returns a measure of the intensity contrast between a pixel and its neighbour over the whole image. It defines the local variations from 0 for a constant image up to the square value of GLCM row or column size. Contrast is the difference moment of the probability values over GLCM. The variation in contrast values over different GLCMs can show the variation toward different directions in the image.

3.6 Chapter Summary

In this Chapter, a review of level set methods was presented. Level set methods are propagating fronts which are widely used in shape and contour evolution which led to several developments in 2D and 3D image segmentation. The literature review shows that there are still some problems in level set image segmentation. For example in region-based methods, they cannot converge to objects boundaries perfectly. In general, they gradually converge to zero after a large number of iterations, the segmentation result depends on the initial contour placement, shape and the choice of its parameters. Also, different level set methods can perform very well for different imaging applications, although they are very much dependent on the parameter settings. In this thesis parametrisation is one of the main issues as it is impossible to make it automatic for CT/CBCT scans of the lungs since there is no reference for training them. The challenges focused and the proposed model are investigated further in the next chapters. This chapter also provides information about the basics of texture analysis needed for the proposed method.

Chapter 4

Performance Assessment of Level Set Methods

4.1 Introduction

In Chapter 3 the performance of texture analysis with different level set methods for image segmentation applications was reviewed. All level set methods can perform well assuming the most appropriate parameters for specific images in particular applications are selected; for example the Chan-Vese model might work better in blurry environments but the Pereyra-McLaughlin model can perform better for real time segmentation. Therefore choosing a model with fewer difficulties in parameter tuning as well as better accuracy for lung CBCT images is the goal of this thesis. Although the time required by analysis selected model is also important, the goal of this study was not real time operation. Consequently comparatively slower models are also considered as the focus is more on the quality of the model. Another issue with the lung dataset is the absence of gold standards for CBCT images which makes it a particularly challenging problem to find the best parameters. Therefore a model which has comparatively fewer difficulties in parameter tuning is a better approach for this research.

In this chapter, the performance of chosen level sets is considered on medical and non-medical images to help in finding the most appropriate method. While the aim is lung CBCT image segmentation, other medical and non-medical images are also used to aid understanding of different algorithms and evaluating them in regards to parameter setting as ground truth is available for these scenarios. Section 4.2 shows the characteristics on test images. In Section 4.3, different level set methods are compared for selecting the most compatible one for the proposed model in combination with texture features. In Section 4.4 Chan-Vese and Li models are used as they are very robust models which can perform very well in combination with texture analysis for lung CBCT images. Applying first-order and second-order texture features as a pre-segmentation step, Haralick features are chosen for texture analysis and used in different combinations with the level set. In this section, the strength of these models and reasons for selecting them is explained. Section 4.5 describes the second contribution of this thesis, a new level set method by combin-

ing existing models together. This contribution implies that instead of re-initializing the same model for level sets in vector-image or multi-phase applications, combining the two best performing models or the same model with different parameters can result in better performance. The proposed model is beneficial for multi-region segmentation but not for the lung CBCT images as two regions of segmentation is sufficient. In Section 4.6, the parameter settings and the relevant difficulties are discussed, also the proposed parameter tuning technique for lung dataset in the absence of any knowledge about GTV on CBCT images is illustrated and explained.

4.2 Test Images

The non-medical images were chosen from the level set segmentation literature as shown in Figure 4.1. The gourd, gradient-ball and spiral in Figure 4.1.a., b. and c. respectively is not very textured. These simple images are useful in illustrating the performance of different level set methods on low detail images. The gradient-ball is chosen to compare the performance of different methods on a simple inhomogeneous image. The Europe-night (Figure 4.1.d.) is very textured image which is good to test on the outcomes of level set for its length of convergence in different methods. The shapes and paper-spiral in Figure 4.1.e. and f. respectively are good examples of noisy images which can illustrate the performance of level set methods in an environment. The resolution of the images is 57×77 for the gourd, 128×128 for the gradient-ball and spiral, 187×216 for the shapes, 128×103 for the paper-spiral and 256×243 for the Europe-night shown in Figure 4.1.

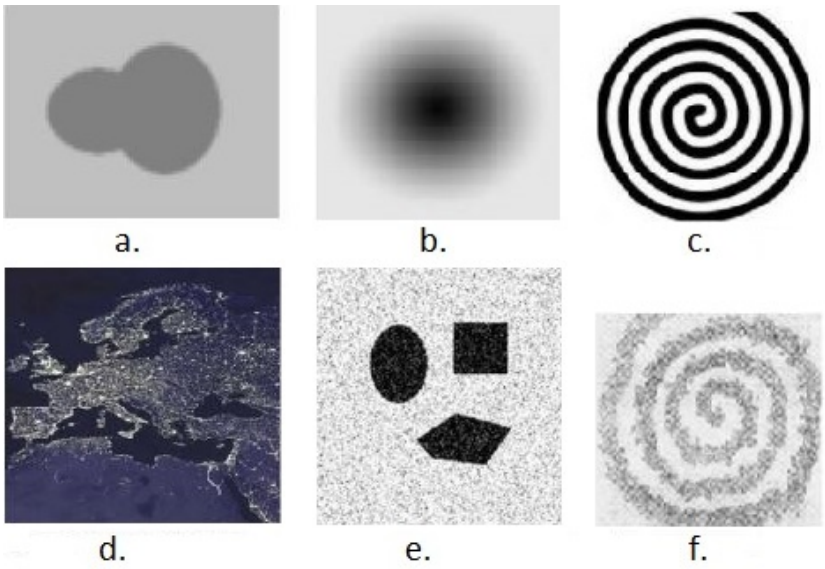

Figure 4.1: Non-medical test images: a. gourd, b. gradient-ball, c. spiral, d. Europe-night, e. shapes and f. paper-spiral.

Also medical images are used to consider the suitability of these models. The medical images consist of brain MRI and lung CT. Figure 4.2.a. shows the images of two different MRI slices of different brain cancer patients with a glioblastoma, highlighted by their relevant GTV and PTV highlighted in red and blue respectively. Similarly in part b. two lung CTs sampled from the main dataset for this thesis showing non-small cell lung cancer of different types. This data specifies the main challenge of this thesis, which is the absence of GTV on CBCT images and will be discussed further in chapters 5 and 6. In the following section, the selection of level set method is discussed and the performance obtained on the test images discussed.

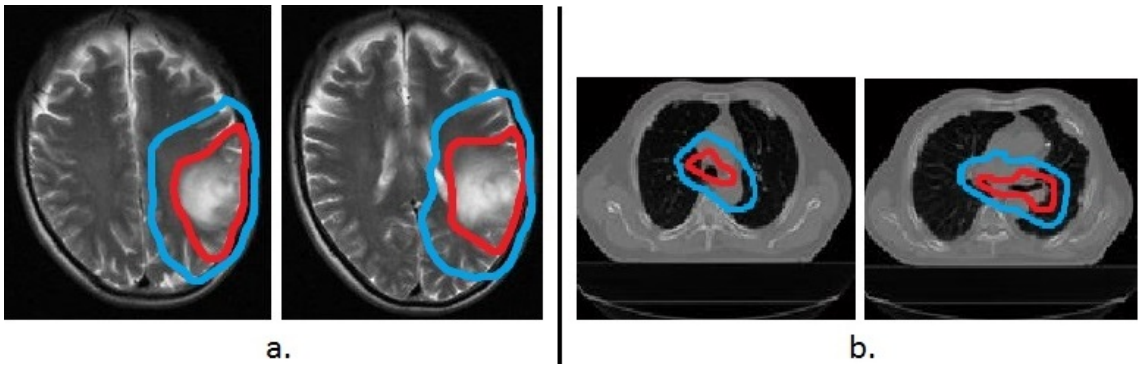

Figure 4.2: Medical test images with GTV in red and PTV in blue colour: a. two different MRI slices of brain cancer and b. two different CT slices of lung cancer.

4.3 Level Set Method Selection

In order to choose the most appropriate level set method, some of the most popular models with good performance in medical imaging were tested. In Figure 4.3, the level set segmentation of different models for the images in Figure 4.1 are illustrated. Each row shows the performance of one of the popular methods on different test images: a. test images, b. Pereyra-McLaughlin [77] c. two-phase Chan-Vese [62], d. multi-phase Chan-Vese [65], e. two-phase Li [90], f. multi-phase Li [71], g. Bernard [80], h. Shi [81] and i. Lankton[74]. The time of execution and the number of iterations of the different methods for these images is listed in Table 4.1. Also, Figure 4.4 illustrates the results for the medical images of Figure 4.2 for more models in addition to Table 4.1. These experiments were ran on Dell Inspiron 17R SE (Model 7720) with specifications of 3rd Gen Intel Core i7 quad core processors, 8 GB of DDR3 memory and Windows 8.

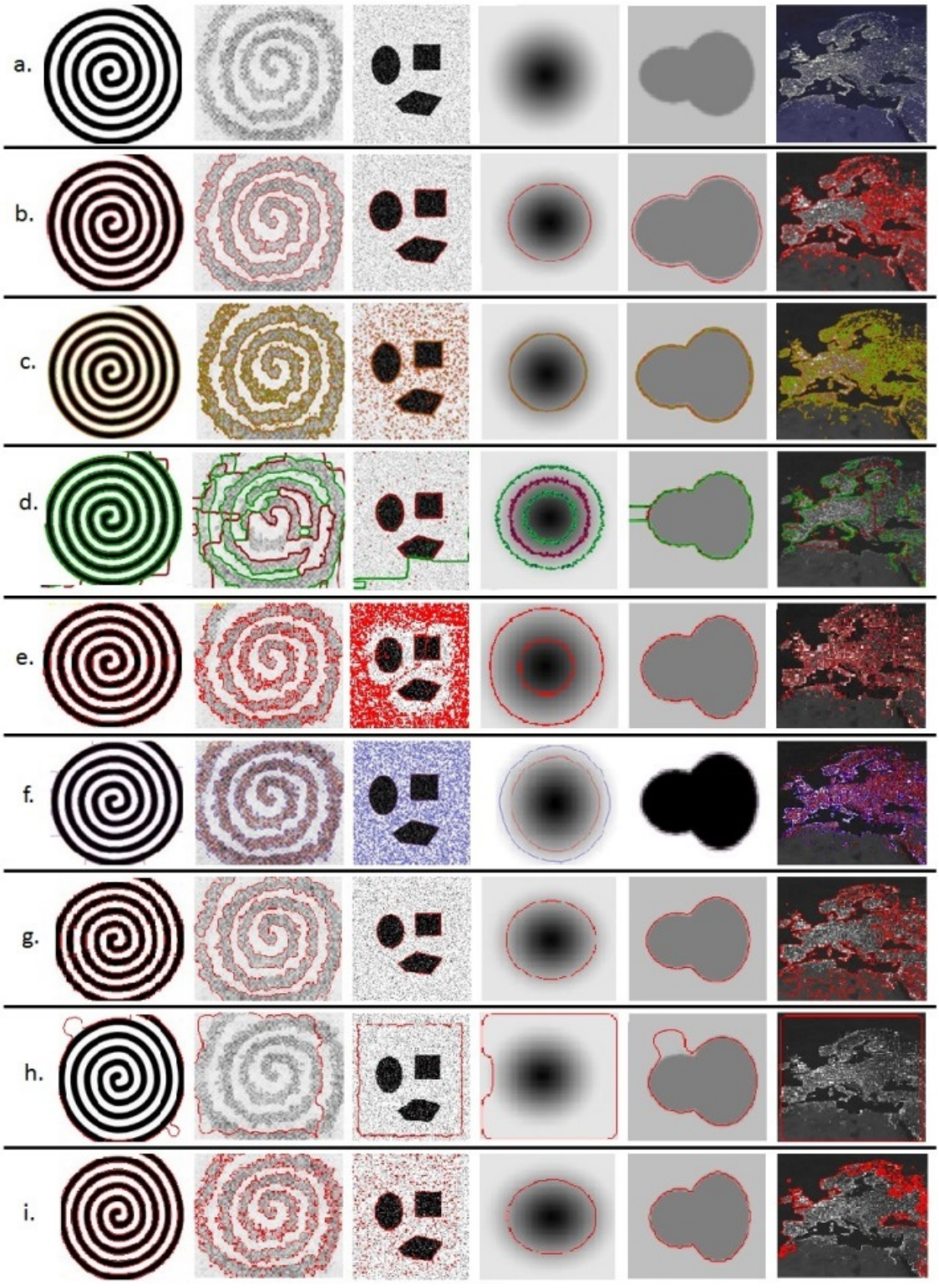

Figure 4.3: Non-medical images segmentation with different level set methods: a. test images from Figure 4.1, b. Pereyra-McLaughlin [77] c. two-phase Chan-Vese [62], d. multi-phase Chan-Vese [65], e. two-phase Li [90], f. multi-phase Li [71], g. Bernard [80], h. Shi [81] and i. Lankton[74].

Table 4.1 compares the number of iterations for different images while considering the time of convergence using different level set models. For example, Pereyra-McLaughlin model converges in two iterations in 0.45 second for a good segmentation while two-phase Chan-Vese converges in 85.22 seconds while having 4124 iterations.

Non-Medical Test Images	Pereyra-McLaughlin	Two-phase Chan-Vese	Multi-phase Chan-Vese	Two-phase Li	Multi-phase Li
gourd	0.59/2	1.08/104	106.1/1000+	1.83/90	2.93/99
gradient-ball	0.47/3	8.08/1042	64.78/2000+	10.4/500+	14.55/500+
spiral	0.49/2	5.59/517	46.72/2000+	10/100	18.01/500+
Europe-night	0.77/2	91.68/1453	138.53/2000+	41.87/114	208.73/500+
shapes	0.59/2	104.89/1353	534.07/1000+	200/500+	338.92/500+
paper-spiral	0.45/2	85.22/4124	45.43/2000+	10/100	56.72/498

Table 4.1: Time of execution (s)/number of iterations for non-medical image segmentation with different level set methods (Pereyra-McLaughlin [77], two-phase Chan-Vese [62], multi-phase Chan-Vese [65], two-phase Li [90] and multi-phase Li [71]).

In Figure 4.3 and Figure 4.4, the Pereyra-McLaughlin model, performs very well for simple images but is not as accurate for the more complicated medical images. The experiment achieves results in two iterations which makes this model suitable for fast implementation. This model converges faster than most level set methods but it does not work well for detailed and blurry medical images, performing very effectively locally but not globally due to lower image intensity range. The two-phase Chan-Vese model performs well for simple images as it only segments two regions. The first and second columns in Figure 4.4 for each model illustrate results on brain MR images which are more complex and the level sets do not show particularly good segmentation results. Figure 4.4.d and e show the result of applying the Chan-Vese model in two and four-phases for different medical images. The improvement of the four-phase level set compared to two-phase is obvious and results from considering more regions of interest. The problem of this model is the convergence time which is lengthy compared to other models. The Li model is another very robust and popular model, it has been used in the literature in many applications and it is faster than Chan-Vese as it does not require to be re-initializated as frequently. The Bernard model performs well for non-medical images and is a fast method. The Shi model performs satisfactorily for non-medical images but the lack of suitability for medical images is obvious. The Lankton model needs tuning at all times because without proper tuning it does not perform well on any of the images tested. The results demonstrate that two-phase segmentation is sufficient for medical imaging. Therefore, two-phase Li and two-phase Chan-Vese are selected as the most stable models.

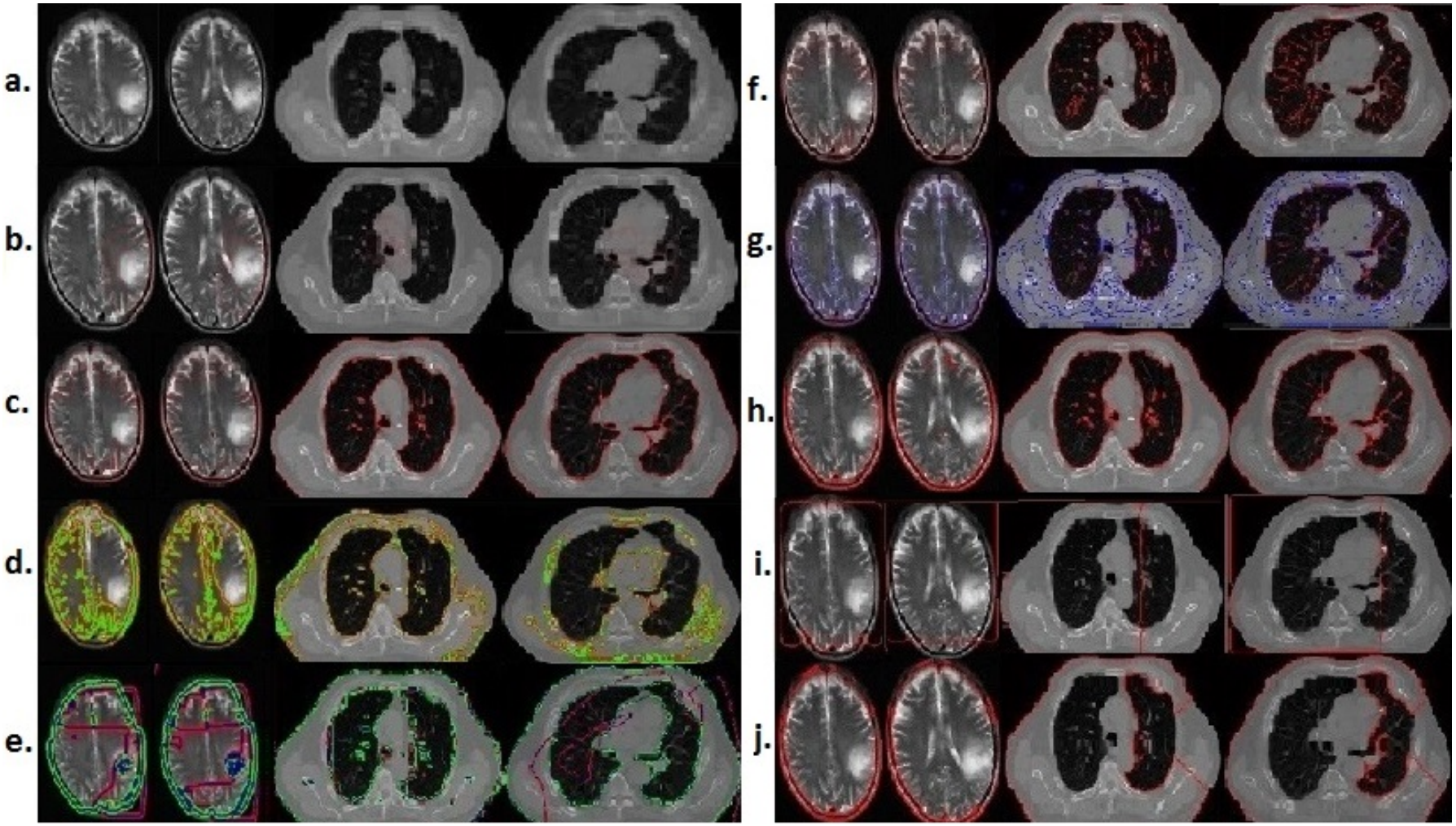

Figure 4.4: Medical images segmentation with different level set methods: a. test images, b. GTV (ground truth) by the oncologist, c. Pereyra-McLaughlin [77] d. two-phase Chan-Vese [62], e. multi-phase Chan-Vese [65], f. two-phase Li [90], g. multi-phase Li [71], h. Bernard [80], i. Shi [81] and j. Lankton[74].

4.4 Proposed Combined Texture and Level Set Model

Level set methods were applied first without any texture analysis on the lung dataset with limited success. The lack of sharpness of these images requires more image enhancement before image segmentation. Several experiments were conducted to find the best order of combining these two techniques. Fourteen combinations of them were implemented by considering different parameters as well as different initializations for level set methods, as shown in Figure 4.5.

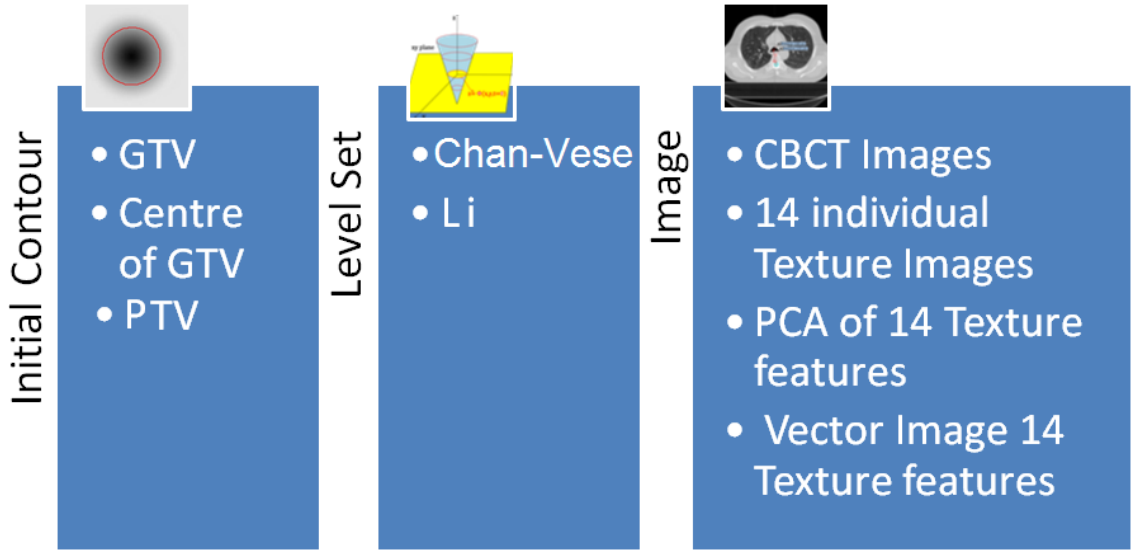

Figure 4.5: Different level set combinations applied on the lung dataset. Initialisation is chosen in three different ways, level set models are either Chan-Vese, Li or both models. Images are either CBCT or pre-processed and replaced by their single texture images, PCA or using all of texture images in vector valued imaging level set concept.

To obtain the optimum performance there were four stages in the procedure:

1. Selection of level set method.
2. Selection of texture features.
3. Combining steps 1 and 2.
4. Initialization of level set.

Section 4.3 narrowed the level set selection to the two-phase Chan-Vese and two-phase Li models. For texture analysis, first and second-order statistical features were tested. In first-order texture features, entropy, local range and local standard deviation were used. Figure 4.6 illustrates these three first-order textures combined with different level set methods. Entropy performs well when it is combined with a level set; it can detect the texture of tumours. The level set performs better on entropy images than the original lung CT, it is because of using the texture information of entropy as an advantage to solely depending on intensity values of the original CT. This is because the local range which is based

on variations in the neighbourhood of each region/pixel does not perform very well at showing the textures of tumours but when it is combined with level set, it still detects all the boundaries. Local standard deviation also performs similarly well to local range, the level set performs better but still does not detect the tumours.

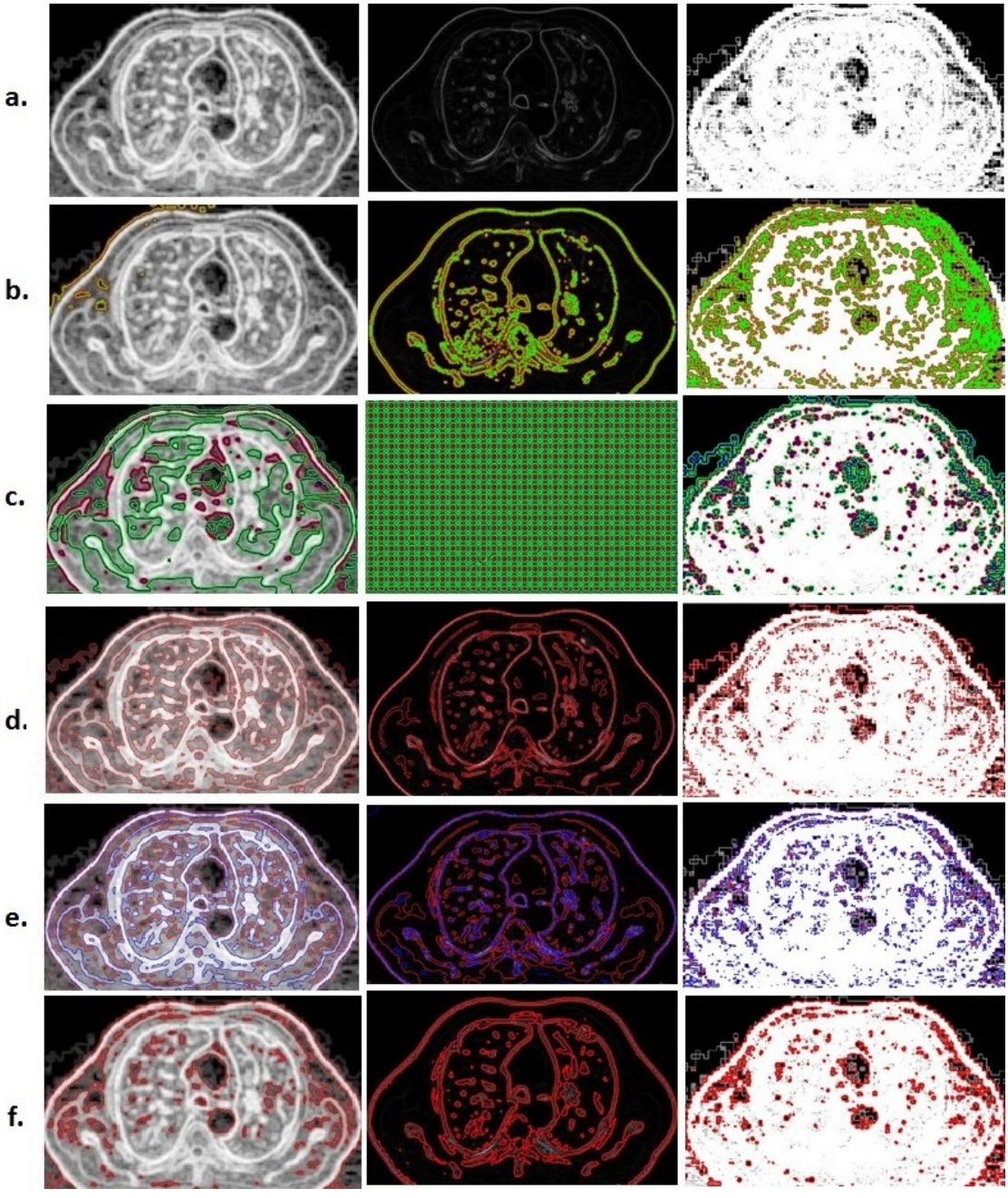

Figure 4.6: First-order texture features combined with different level set methods; a. texture images (left column: entropy, middle column: local range and right column: local standard deviation), b. two-phase Chan-Vese [62], c. multi-phase Chan-Vese [65], d. two-phase Li [90], e. multi-phase Li [71] and f. Pereyra-McLaughlin [77].

Second-order texture of Haralick features which were presented in Section 3.5.2 were applied and are shown in Figure 4.7. This figure illustrates the texture segmentation of a slice of CT from lung dataset, although some of texture features are redundant for this purpose.

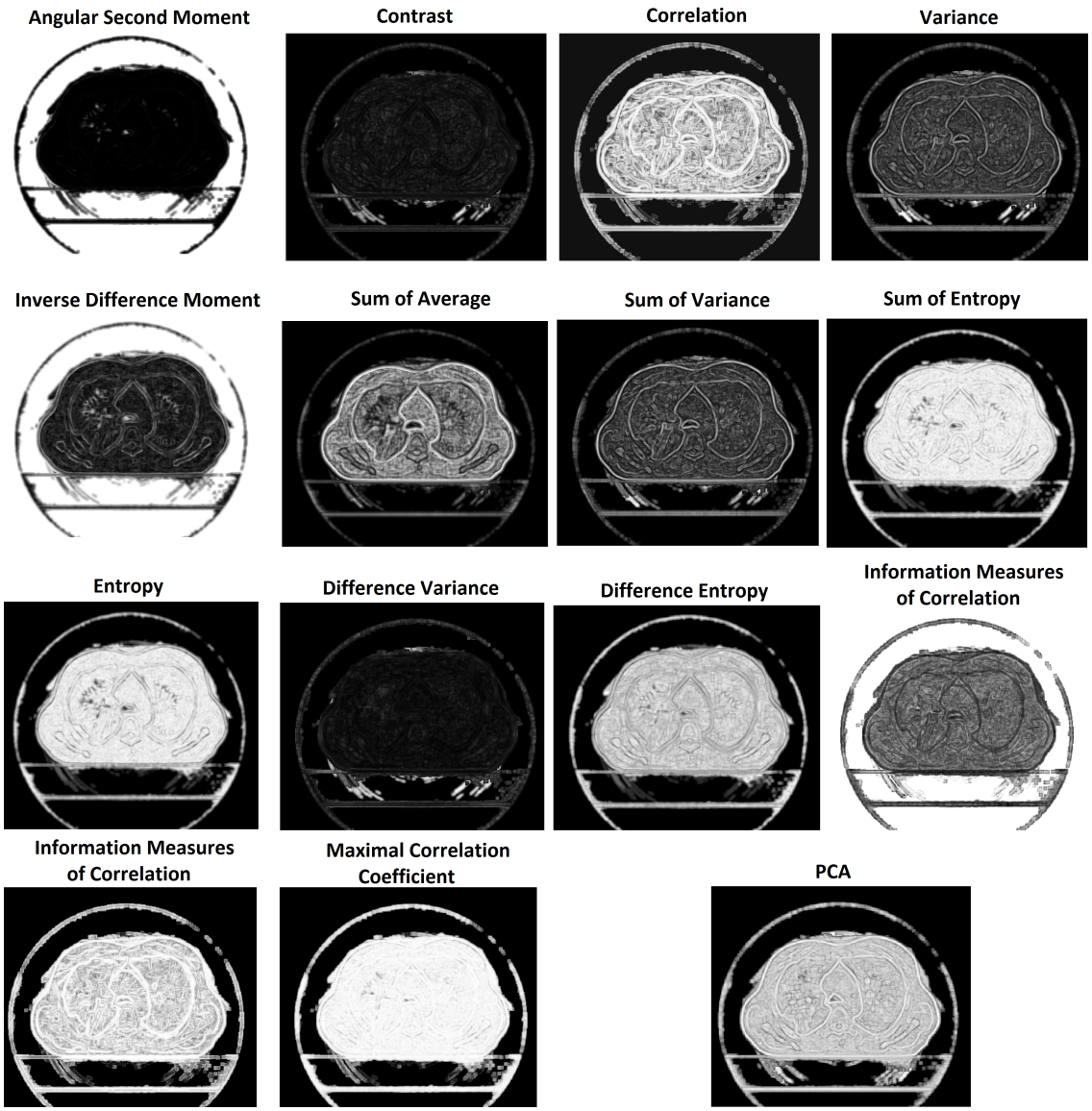

Figure 4.7: Haralick second-order texture features and their PCA of a lung CBCT #1 image for Patient 25 Slice 58.

The result of combining Haralick features and a level set is shown in Figure 4.8. The CT on the right has the GTV in blue and the level set segmentation outcome in red. The performance of the Li model is applied on all fourteen Haralick features. This clearly shows that second-order texture features are more robust than the first-order. Among second-order features, the combination of the sum variance followed by a level set shows much better results compared to the other combinations.

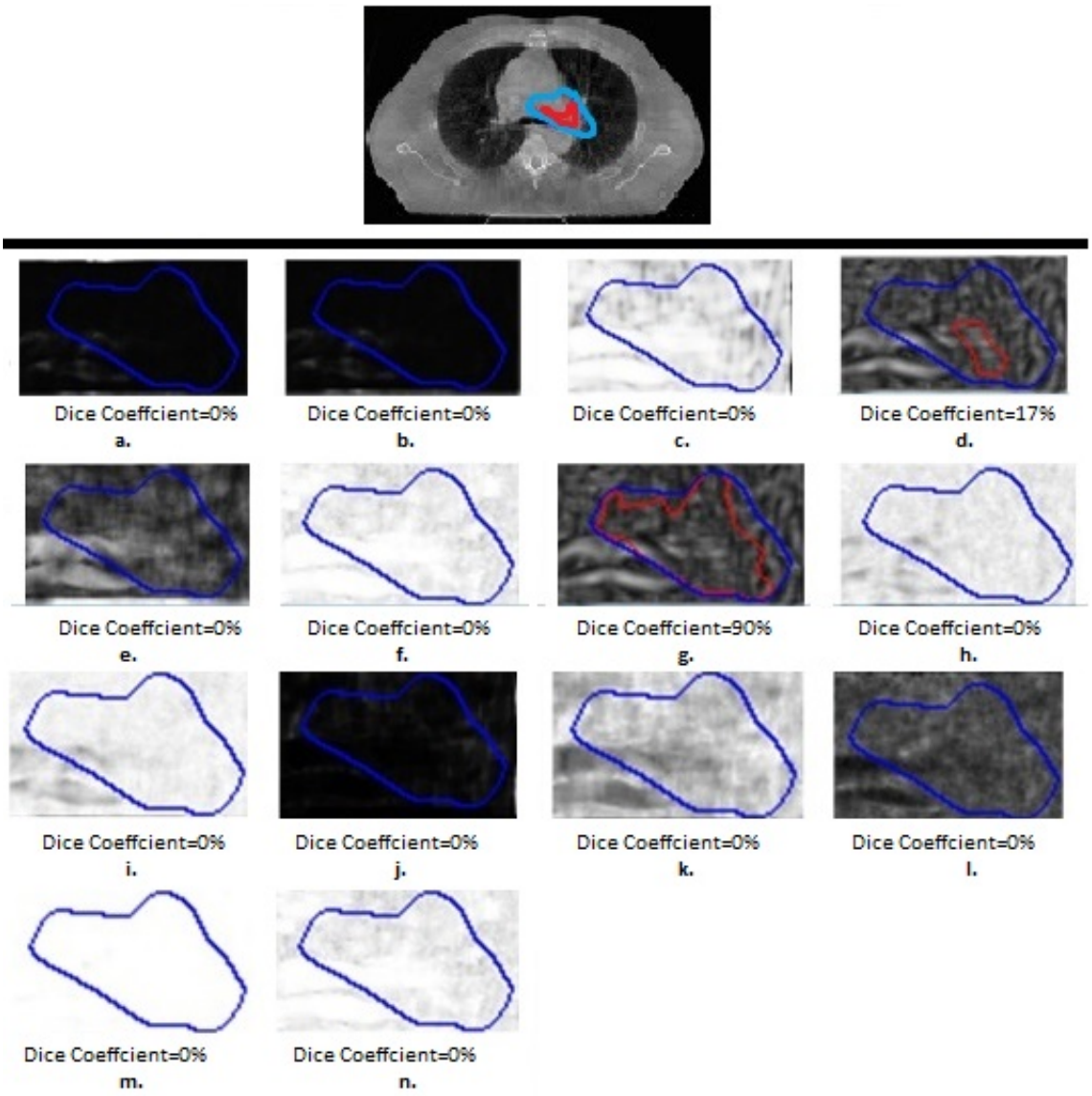

Figure 4.8: Li method on different Haralick features of a CBCT image of Patient 3, the blue contour is the GTV/initialization of level set and the red contour is the level set segmentation, a. angular second moment, b. contrast, c. correlation, d. variance, e. inverse difference moment, f. sum average, g. sum variance, h. sum entropy, i. entropy, j. difference variance, k. difference entropy, l. information measures of correlation, m. information measures of correlation and n. maximal correlation coefficient.

At this stage, combining texture features with level set methods is carried out in three different ways:

1. Chan-Vese and Li models applied on all features separately.
2. All fourteen Haralick features were considered as a vector-valued image and Chan-Vese model applied on it.
3. Chan-Vese and Li models applied on the principal component analysis (PCA) of the fourteen features.

The best combinations were from first and second methods while the third combination based on PCA completely failed due to the large differences among all fourteen images as shown in Figure 4.7.

Initialization was also performed on different orders which affected the parameter setting of level set:

1. GTV by setting the parameters to lead the level set inward or outward from the contour.
2. Setting the centre of GTV as the initial contour by choosing parameters to always lead the level set outward.
3. PTV by forcing parameters to move the level set inward.

As the different initializations preserved more difficulties in the parameter settings and also, since images and texture image settings could differ, the GTV with limited freedom of choice for parameters was selected as the best option.

4.5 Proposed Level Set Method

There are many different level set techniques, every method is designed to be more efficient in calculating propagation characteristics compared to previous versions. The literature review in Chapter 3 showed that every approach is robust to a specific application but not for all kinds of images. This highlights the importance of parameter setting to tune each model to handle more images or not relying on only one technique when the dataset consists of different images. Exploiting the existing models with less computation difficulties could lead to a more efficient segmentation method. This section proposes two new compositions of the existing level set methods.

4.5.1 Proposed Parallel Level Sets in Vector-Valued Image Model

A new level set configuration was designed based on the concept of vector-valued imaging was introduced in Section 3.4.2. The concept of a vector-valued image in level set is introduced first by applying the two-phase Chan-Vese method at the same time on different images, such as different RGB channels or different texture images, and averaging the force value in each image at each iteration as shown in Figure 4.9.

The success of the vector-valued Chan-Vese is in using different features of an image. It needs pre-processing of the image to obtain the features, before applying the same two-phase Chan-Vese on all layers.

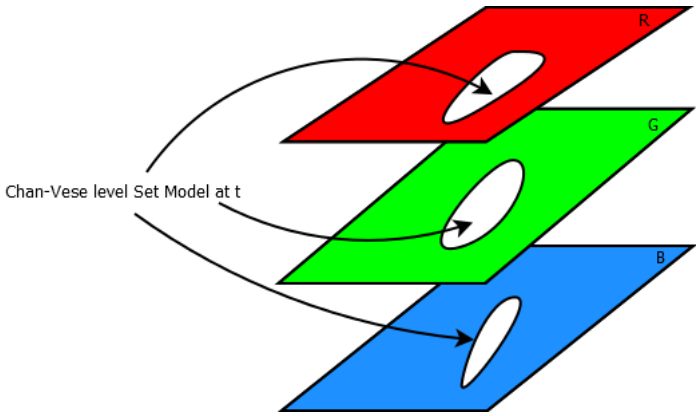

Figure 4.9: Vector-valued Chan-Vese on RGB channels.

The proposed vector-valued image model in this thesis does not require different features of an image but it applies different level sets on the same image at each iteration. This parallel implementation of different level sets on the same image takes advantage of the original image while engaging with the other level set performance by averaging their forces in each iteration. The proposed model is illustrated in Figure 4.10 and Equations 4.1 to 4.4.

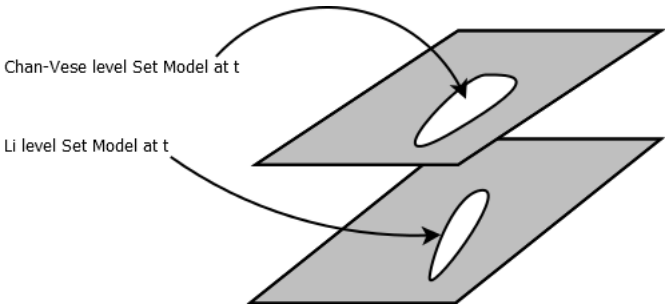

Figure 4.10: Proposed parallel level sets in vector-valued image.

In the proposed approach, the combination of the Chan-Vese and the Li models were used but any other models can be used. The reason is to exploit the advantages of both techniques in each iteration, for example the Chan-Vese model works well for blurred edges while the Li model for sharp ones. Different level sets can also be used but with different sets of parameters. This implementation is beneficial when the user does not know the best set of parameters to tune the model. The force of level set is modified in each iteration by calculating the average forces of both methods.

$$
\begin{aligned}
F_{CV} = \quad & \int_{\Omega} (u_0 - c_1)^2 H(\phi) d_x d_y \\
& + \int_{\Omega} (u_0 - c_2)^2 (1 - H(\phi)) d_x d_y \\
& + \int_{\Omega} |\nabla H(\phi)|
\end{aligned} \tag{4.1}
$$

$$
F_{Li} = \mu P(\phi) + \lambda L(\phi) + \nu A(\phi) \tag{4.2}
$$

Equation 4.1 and Equation 4.2 are the forces for Chan-Vese and Li level set models which are explained in Chapter 3 in more details.

$$
F = \frac{1}{2}(F_{Li} + F_{CV}) \tag{4.3}
$$

Equation 4.3 defines the averaging equation for forces which happens in each iteration that new forces are obtained from each model. Finally, to reinitialise level set, new ϕ should be calculated from Equation 4.4.

$$
\phi(x, y, t+1) = \phi(x, y, t) + \Delta t . F \tag{4.4}
$$

where Δt is the step size.

4.5.2 Proposed Parallel Level Sets in Multi-Phase Method

The proposed parallel level sets model in Section 4.5.1 can be extended to a multi-phase model. The current multi-phase models usually apply the same model twice with a different initialization for the same model. The original multi-phase level set method can fail after a large number of iterations because detected regions from different phases can become the same as the level set characteristics and parameters for different phases are the same. Also, as different objects in an image are expected to have different specifications, different level sets can detect them better than the same model. Figure 4.11, Equation 4.5 and Equation 4.6 illustrates this model.

This model also can use the same methods such as the Chan-Vese but with a different set of parameters like the proposed model in Section 4.5.1. It is actually less complex to use the same model with different initialization and different parameters. In this case each level set and the different regions can be calculated in a similar fashion to Equations (3.34) and (3.35) but different parameters of each level set in PDE can define the new level set differently.

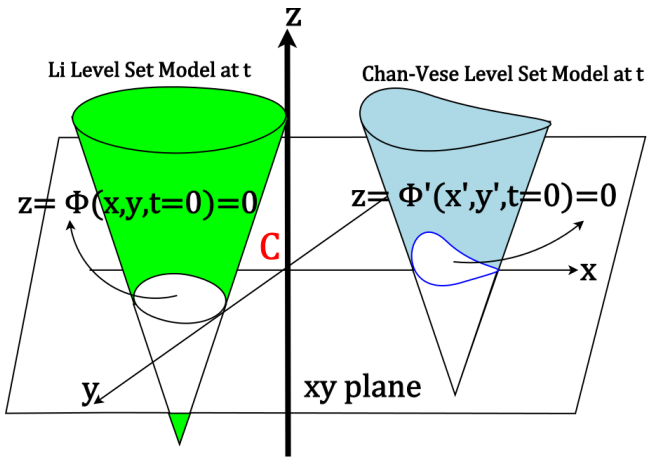

Figure 4.11: Proposed parallel level sets in multi-phase shape.

$$\begin{aligned}\frac{\partial \phi_1}{\partial t} = \quad & \delta(\phi_1)[\nu_1 div(\frac{\nabla \phi_1}{|\nabla \phi_1|}) \\ & - \Big((u_0 - c_{11})^2 + (u_0 - c_{01})^2)\Big) H(\phi_2) \\ & + \Big((u_0 - c_{10})^2 + (u_0 - c_{00})^2))\Big)(1 - H(\phi_2))]\end{aligned} \tag{4.5}$$

$$\begin{aligned}\frac{\partial \phi_2}{\partial t} = \quad & \delta(\phi_2)[\nu_2 div(\frac{\nabla \phi_2}{|\nabla \phi_2|}) \\ & - \Big((u_0 - c_{11})^2 + (u_0 - c_{01})^2)\Big) H(\phi_1) \\ & + \Big((u_0 - c_{10})^2 + (u_0 - c_{00})^2))\Big)(1 - Hs(\phi_1))]\end{aligned} \tag{4.6}$$

where ν_1 and ν_2 are weighting parameters that has been selected differently but their values are the same in Equations 3.36 and 3.37.

4.5.3 Discussion of Proposed Parallel Level Sets

The main purpose of proposing this model was lung CBCT image segmentation, on which level set selection and parameter settings were a problem. This model helps in using both Chan-Vese and Li model where both models provide satisfactory results. Also since parameter setting is so challenging, it can take advantage of different set of parameters to reduce the penalty in the case of suboptimal parameters selection. Figure 4.12 shows the implementation of combined Chan-Vese and Li models on non-medical images in Figure 4.1 and medical images in Figure 4.2.

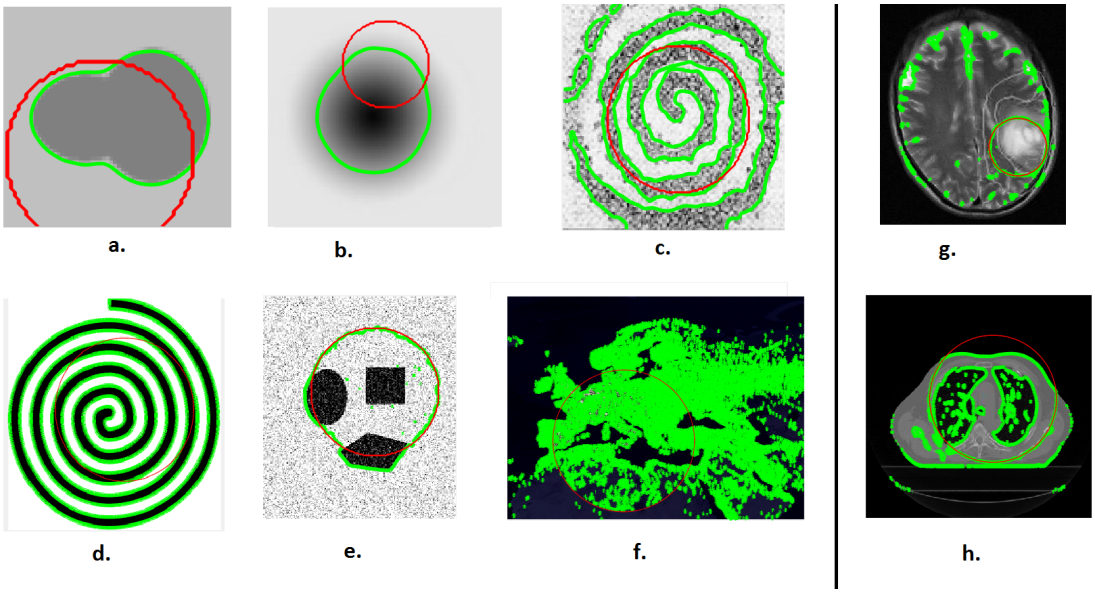

Figure 4.12: Testing proposed parallel level sets in vector-valued imaging on test images (red is the initial level set and green is the level set segmentation): a. gourd, b. spiral, c. paper-spiral, d. shapes, e. gradient-ball, f. Europe-night e. brain MRI and g. lung CT.

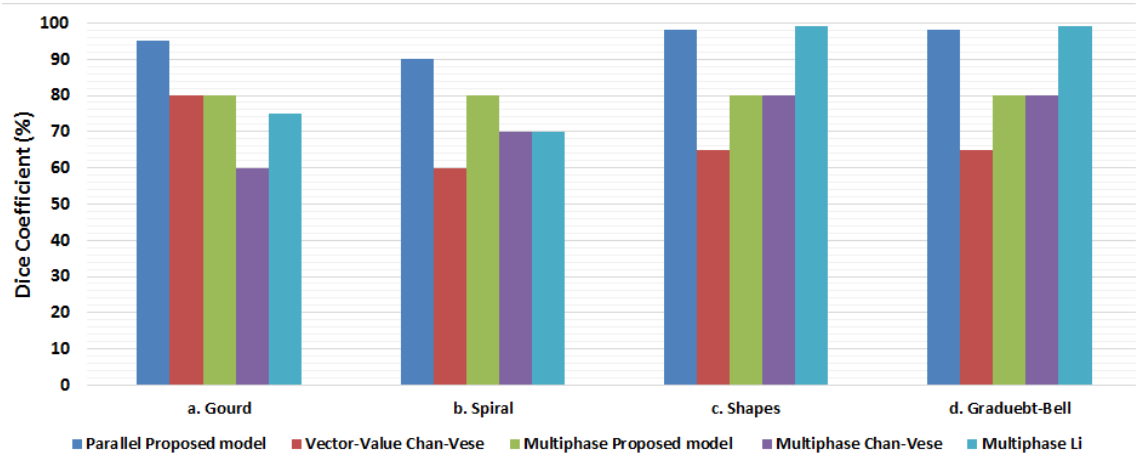

Figure 4.13: Testing proposed parallel level sets in vector-valued and multi-phase level set on test images with ground truth: a. gourd, b. spiral, c. shapes and d. gradient-ball.

Comparing Figure 4.12 with Figure 4.3 shows the proposed configurations of the level set in this Section can perform better than other multi-phase and vector-valued image models. For instance, combining Chan-Vese and Li models can be compared to an individual approach using either method while having the same set of parameters. Medical images can be combined for a different set of parameters of each model on their texture feature or smoothing image in parallel with original image while applying same level set method with slightly different set of parameters. Figure 4.13 illustrates the performance of proposed model combining Chan-Vese and Li models compared with vector-valued

and multiphase Chan-Vese as well as multiphase Li. Four non-medical images which have ground truth are chosen and its similarity with the level set segmenting of them was compared by Dice coefficient. The results illustrate the success of the proposed model over its original forms as parallel level set can perform over 90% accurate for all of these images. The poor performance of other models can be due to low contrast of these images. Other images in Figure 4.12 were not assessed qualitatively as their ground truth is not very accurate. The results for these images appear to be subjective assessment through satisfactory compared to the original models shown in Figure 4.1 and Figure 4.2.

4.6 Tuning Level Set Parameters

The absence of ground truth for lung CBCT dataset makes the importance of parameter setting based on trial and error more problematic. Since in external diagnostic imaging the real ground truth would never be available due to their low quality and difference of opinion among clinicians therefore understanding the characteristic of parameters is the most important part in any medical image analysis algorithm.

In general, the approach of variational or optimization problems is to assign a cost function to each element to see how this cost solves the problem, where a low score is a good match and a high score is a bad match. Once the cost function is designed, the configuration of the lowest cost if the cost is not convex, can make it difficult to find the minima. Gradient descent or steepest descent methods work by initializing and then descending at each instance, the direction is checked by the derivative the slope or the curve. By respecting this rule and trying to keep the optimization equations always in a convex form, the parameter setting in active contours and level set methods is simpler. By finding the most relevant parameters, the level set methods can be tuned to converge to appropriate boundaries. As previously pointed out, the lack of gold standard for lung/medical imaging makes finding the optimal parameters more challenging, requiring a greater depth of image analysis.

In the Li and Chan-Vese models, the parameters of α, λ, ε and σ can be chosen in many possible combinations. In this thesis, μ which is mostly fixed as one tenth of a time-step in the literature [65] and [71], defines the coefficient of the distance regularization term $R(\phi)$,the parameter for identifying the regularizer's coefficient that has a great impact on the smoothness. For the number of iterations which had one inner parameter and one outer parameter, values were chosen from small to large to give more freedom in convergence of the level set. λ defines the coefficient of the weighted length term $L(\phi)$. The importance of λ can be shown in the following figures, which employ amounts very high and low amount for λ. λ can control the smoothness of the optimization, it should not be negative because it would stop convexity and also would favour (remove) smoothness. α, coefficient of

the weighted area term $A(\phi)$ gives better results for negative values in medical images. ε, specifies the width of the Dirac Delta function. σ is the variance value for Gaussian distribution. Time constant or step size which would be better if the value is smaller but the calculation would be more costly time-wise.

Figure 4.14 shows the flow chart for the parameter setting for level set methods on CBCT #10 based on their CBCT #1 image.

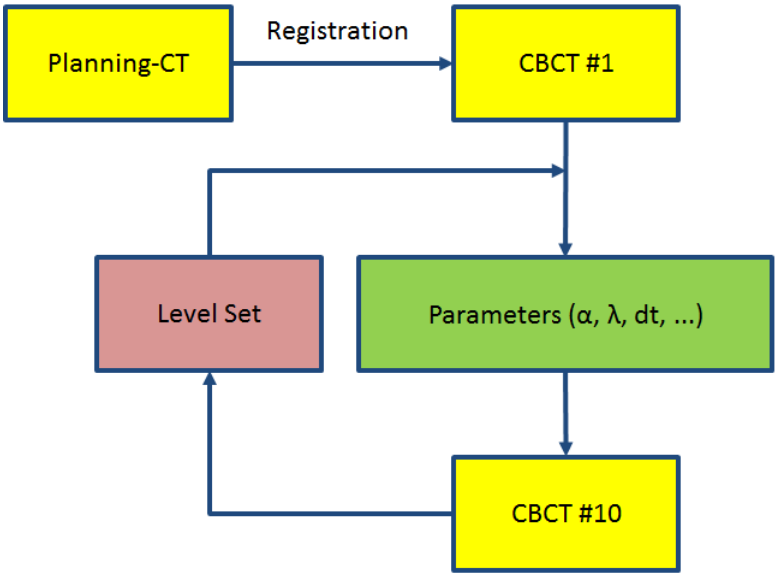

Figure 4.14: Scheme diagram for parameter settings for lung data.

Although parameters are found in iteration loops, this framework makes the parameter setting more reliable for the user and faster as the parameter sets are defined for each iteration. For instance Figure 4.15 is one good example of this kind of automatic parameter setting.

Figure 4.15 shows some of the results for different parameters for lung CT and CBCT images with further results in Appendix B. These figures illustrate the performance of Chan-Vese and Li models on CBCT images as well as on texture image (sum variance) by randomly setting different parameters. The blue contour represents the GTV, delineated by clinicians, the red contour is the centre of GTV which is used in some cases as the initial level set to set the parameters in growing always mode and finally the green contours are the level set results which vary in different images. In some cases that there is no green contour, which means that the level set could not segment. The best choice of parameters can lead to an accurate segmentation. This will be studied in greater detail in Chapter 6 .

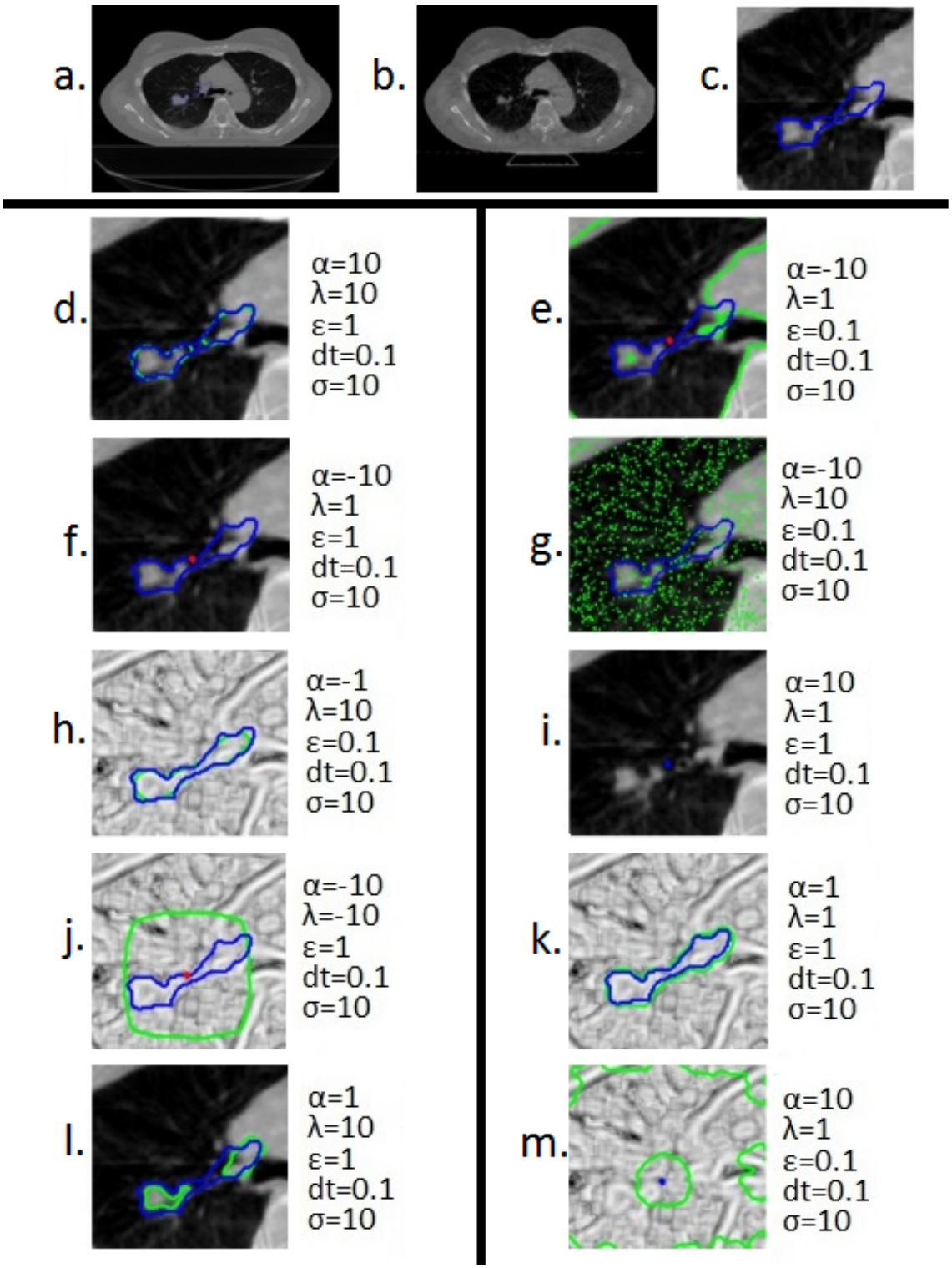

Figure 4.15: Performance of different combinations with different parameters for lung CBCT image tumour segmentation, Patient 2-Slice 41: a. planning-CT, b. CBCT #1, c. cropped part of of part c with clinical GTV, d. Li model on CBCT using GTV as its initial contour, e. Chan-Vese model on CBCT using centre of GTV as its initial contour, f. Li model on CBCT using centre of GTV as its initial contour, g. Chan-Vese model on texture image using GTV as its initial contour, h. Li model on PCA image using GTV as its initial contour, i. Chan-Vese model on vector-valued texture image using centre of GTV as its initial contour, j. Li model on PCA image using centre of GTV as its initial contour, k. Chan-Vese model on PCA image using GTV as its initial contour, l. Chan-Vese on CBCT using GTV as its initial contour and m. Chan-Vese model on PCA image using centre of GTV as its initial contour.

As shown in Figure 4.15 and Appendix B, poor parameter choice can totally change the performance of a robust model for the worse. Therefore, the parameter setting has to be done by taking advantage of all existing information. In lung cancer treatment, planning-CT images which have GTV contours on them are acquired before treatment. CBCT #1 is the next image taken from cancerous lungs but before any RT treatment. These images are the closest to planning-CT images as they are acquired less than a week after planning-CT. There are possibilities of changes in GTV from planning-CT to CBCT #1 but by considering small changes which are ignorable on average for fifty patients.

4.7 Conclusions

This chapter shows the formation of the proposed model. Combining texture analysis and level set method in different aspects was reviewed. Different test images in medical and non-medical shapes were used to illustrate the performance of some popular and well known level set methods. Chan-Vese and Li methods used in different combinations with texture features and different initialization mode. The proposed model presents a better segmentation compared to level set alone. Since lung dataset lacks ground truth on CBCT images, a parameter setting framework presented which finds the best parameters based on GTV on CT images.

As level set parameter settings are very challenging, a new level set method has been proposed which exploits the advantages of different level set methods or same model with different set of parameters. It gives the freedom of two or more level sets to run in parallel on the same image in each iteration. The concept can be used in vector-valued image level set or multi-phase level set. This model was tested on non-medical images and it succeeded over its conventional forms. The results on medical images from the lung dataset is shown in Chapter 5 and Chapter 6.

First and second-order statistics were both applied to the data. However, GLCM using second-order texture provides better information than first-order as it defines the location relationship. Sum variance combined with two-phase Chan-Vese or two-phase Li level set methods were performing outstanding compared to other texture features as well as other level set methods.

Chapter 5

Implementation of Texture and Level set Analysis on the Lung CBCT Data with the GTV of a Specific Patient

5.1 Introduction

This chapter investigates the proposed combined texture and level set model on one patient with the GTV available at CBCT #1 and CBCT #10. This patient had a concentrated tumour attached to the lung pleura and the tumour shrank dramatically during treatment. A clinical oncologist was able to estimate the contour on these slices/images for both #1 and #10. Out of the fifty patients in the dataset, only this case (Patient 25) provided quantitative analysis to evaluate the performance of the combined texture and level set model. The other forty nine patients had more complicated tumour shapes and positions where the cancer was contained in different regions of the lungs, therefore CBCT images did not provide any visualisation information about the status of tumour to the clinicians.

The shrinkage of the tumour in this case is clearly visible and the Dice coefficient showed a similarity of greater than 90% between CBCT slices and their relevant ground truth. The only possible comparison for the other forty nine patients was level set segmentation of CBCT #10 and the GTV on CT data and not CBCT. In order to evaluate the reliability of the proposed model, this chapter seeks to demonstrate that the shrinkage of tumour volume for Patient 25 can be measured automatically. Also this model can be extended in offline ART to improve the planning treatment to amend the remaining treatment schedule based on the results of RT obtained up to CBCT #10.

The fifteen level set contours presented in Section 4.4 and Section 4.5.1 are displayed on CBCT #10. Based on the evaluation of the oncologist, three of the proposed level set-texture feature combinations based on Chan-Vese and Li methods were selected. Further, the proposed parallel level sets segmentation was tested and compared with the relevant GTV on each available fraction of CBCT for Patient 25. The evaluation of this patient is demonstrated in qualitative and quantitative forms.

This chapter is organised as follows. The patient information is presented in Section 5.2. The texture analysis and reasons for selecting sum variance among the texture features are discussed in Section 5.3. All fifteen different segmentation models are discussed in Section 5.4. The texture and level set segmentation is discussed in Section 5.5 to illustrate the performance of the proposed model on Patient 25. The texture combined level set is analysed quantitatively in Section 5.6 and qualitatively in Section 5.7. The outcome of this chapter confirms the strength of this model, which can subsequently be applied to the other forty nine cases. Section 5.8 presents the possible extension of the proposed model to offline ART.

5.2 Patient 25 Data

This patient has a very localized tumour in the right lung. The planning-CT was acquired on 10^{th} of May 2011 with a resolution of $512 \times 512 \times 130$, and $3mm$ slice thickness. The GTV on the planning-CT was delineated for fifteen slices from Slice 50 to 64. The position of the tumour is illustrated in Figure 5.1 on one slice in the middle of the tumour in different planes, the cross-sections are illustrated from transverse, frontal and sagittal views. Also its 3D shape is shown in the same figure to show the volume of tumour inside the body.

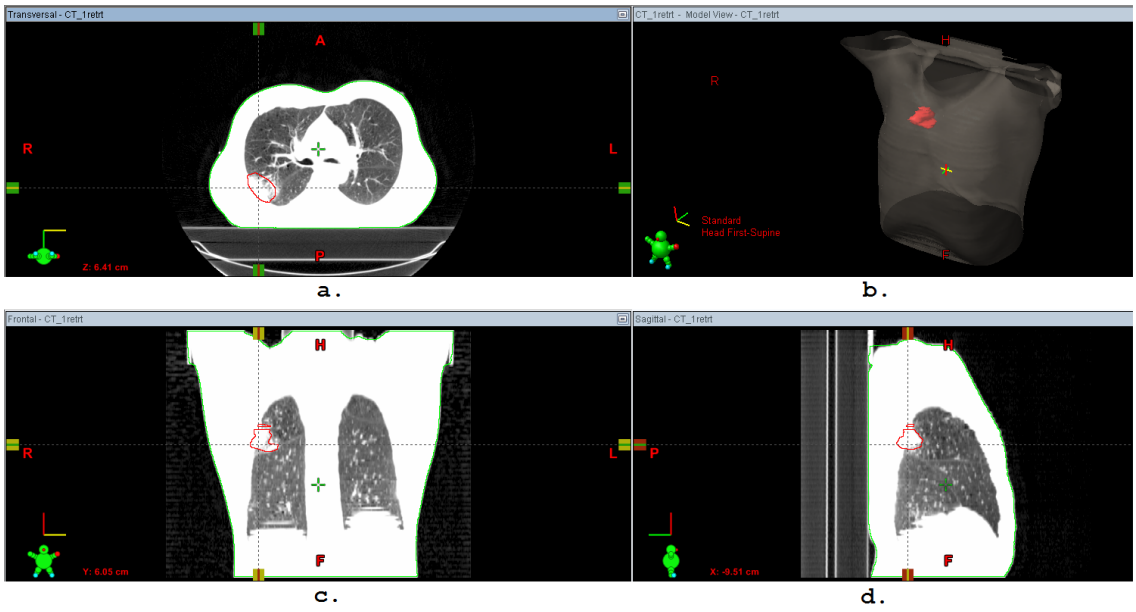

Figure 5.1: a. transverse, b. 3D shape, c. frontal and d. sagittal image views of Slice 55 of Patient 25 showing the GTV in red. This figure is generated using Varian Eclipse medical software.

The tumour is located toward the upper section of the lung, an area which is less affected by the breathing movements of the chest than other parts of the lung. Figure 5.1 shows

three different images of the tumour on the planning-CT for patient 25. Figure 5.1.a is the transverse cross sectional view where the red contour displays the GTV, the dotted grid vertically and horizontally across the tumour better illustrates its position in the frontal and sagittal cross sectional views in 5.1.c and 5.1.d respectively. Figure 5.1.b shows the full 3D shape of the tumour in red inside the body, the volume of tumour is 5% of both lungs.

This patient responded very well to RT. Figure 5.2 illustrates the clinical GTV on the planning-CT, CBCT #1 and CBCT #10 in blue. This patient is the only case where the oncologist could delineate the tumour volume on the CBCT images due to the obvious position of the tumour, which may be because of the reduced movement of the chest in this area. Even in this case, the vessels, airways and other parts of the lungs made contouring very complicated. These scans/images provide good examples of the efficacy of the proposed image processing method, however there are more sophisticated stages of lung cancer for other patients in the dataset where it is impossible to differentiate the tumour from healthy tissue on the CBCT images as we will subsequently see in Chapter 6.

Figure 5.2 illustrates GTV shrinkage for this patient. The relevant GTVs are all delineated on each set of images separately. Image 5.2.a is the planning-CT, 5.2.b CBCT #1 with similar size of tumour because both these images are collected before any RT. Figure 5.2.c is CBCT #10, after 9 fractions of treatment.

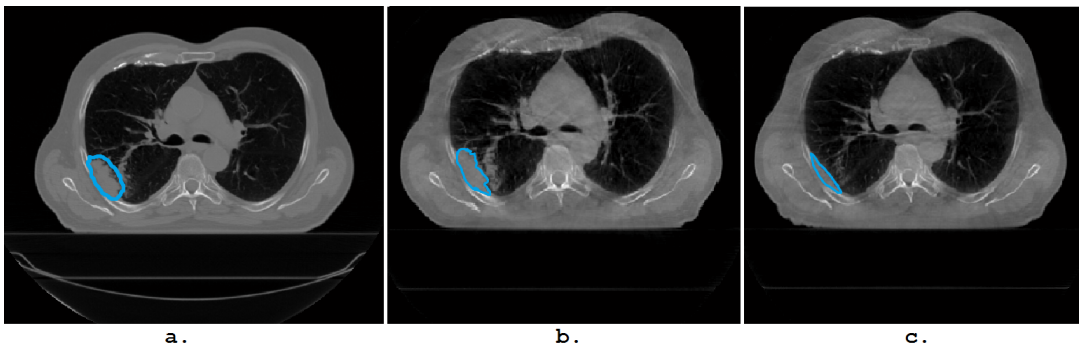

Figure 5.2: Patient 25 progress of treatment with the clinical GTV contours on both CT and CBCT images, a. planning-CT, b.CBCT #1 and c. CBCT #10.

Figure 5.3 shows that the tumour shrunk by 30% between CT, CBCT #1 and CBCT #10. In this figure the normlized value for area of GTV per slice having tumour is demonstrated. Slice numbers vary from 50 to 64 which refers to the fifteen slices out of 130 CT slices acquired from the patient during planning-CT. Although CBCT slices were less than planning-CT but due to registration of these images they have the same numbers.

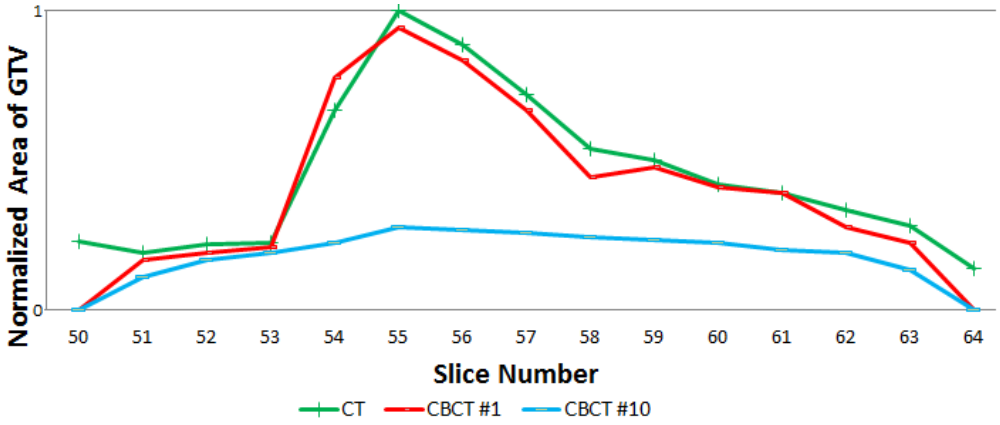

Figure 5.3: Tumour area comparison between the clinical GTV on planning-CT, CBCT #1 and CBCT #10 of Patient 25.

It is important to note that GTV on CT and on CBCT #1 were delineated at different times, therefore a slight difference is to be expected as the oncologists were different. The image quality is also noticeably different. The similarity between GTV on CT and CBCT #1 and #10 can be calculated based on their size and area overlap. It is interesting that the combined texture and level set model in Figure 5.4 in Section 5.5 shows the same amount of change. This suggests the proposed model may perform well for other patients in this dataset. Also the behaviour of the proposed model was considered slice by slice by the GTV on related CBCT and gave over 90% similarity. All these analyses are shown more in detail in the following sections.

Figure 5.4 demonstrates the expected area deduction of tumour of Patient 25 as shown in Figure 5.3. This is effectively the gold standard of this thesis which confirms the strength of this model which can subsequently be applied to other forty nine cases.

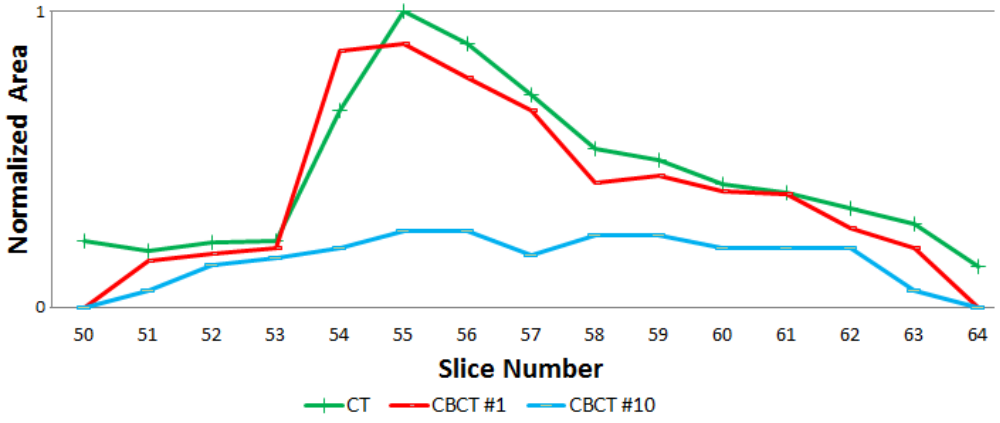

Figure 5.4: Tumour area comparison between the clinical GTV on planning-CT, level set method of CBCT #1 and level set method on CBCT #10 of Patient 25. The results of Model m is chosen here to show this comparison.

The success of the proposed models which was shown in Figure 5.7 and Figure 5.4, depends on three factors: initialization using GTV on CT, texture image and the choice of parameters. The level set is very much related to its parameter tuning, therefore choosing good parameters based on CBCT #1 leads to better performance on CBCT #10. Level set is assisted by texture and the parameter estimate on CBCT #1 to perform well on CBCT #10. The framework of this model was shown previously in Figure 4.14. The recursive parameter setting used in this approach minimises the errors. Each patient and even each CBCT for each patient needs different parameter settings. Sometimes changing parameters for different slices also leads to better segmentation. ROI in each slice is changing, along with time and the patient's breathing, therefore the best parametrisation is not possible by having the same set for all slices. For Patient 25 the parametrisation for all slices are very similar but with some small differences.

5.3 Texture Analysis of Patient 25 Data

Of the fourteen texture features of Patient 25, obviously some of the features are not well distributed in terms of intensity which might give a weak input for level set convergence. All Haralick features were applied, while considering GLCM in four symmetric directions in a 5×5 area. The best texture model which could be combined well with Chan-Vese method is sum variance. There are other textures which also show good results but interestingly sum variance always works well.

To gain a better understanding of why sum variance outperforms other features, Figure 5.5 and Figure 5.6 illustrate all features followed by their histogram and the equalised histogram image of CBCT #1 and CBCT #10 respectively. The red contour refers to GTV on CT. It is obvious that F6 as the sum average and F7 as the sum variance can pre-segment the tumour boundary best. Only sum variance has the original smooth histogram and can highlight the tumour more accurately than other features for all slices of CBCT #1 and CBCT #10. Besides demonstrating the strength of sum variance, Figures 5.5 and 5.6 also show the impractical usage of some other features for this application. For example, some features such as F12 to F14 cannot assist in any pre-segmentations and can disrupt the performance of other features when combined with them.

The main reason of failure of most of these texture features is due to their low range of intensity levels. F1, F3, F5, F8, F9, F11, F12, F13 and F14 have not enough intensity variation at all, therefore these texture images are not able to provide a better intensity variation image compared to CBCT image for level set. F2, F4, F6 and F10 are low dynamic range images which also cannot pre-segment well due to their low variation levels. F7, sum variance, has sufficient variation in intensity and preserves more of the

dynamic range of the variation. This accessible dynamic range of histogram proves the superior performance of sum variance.

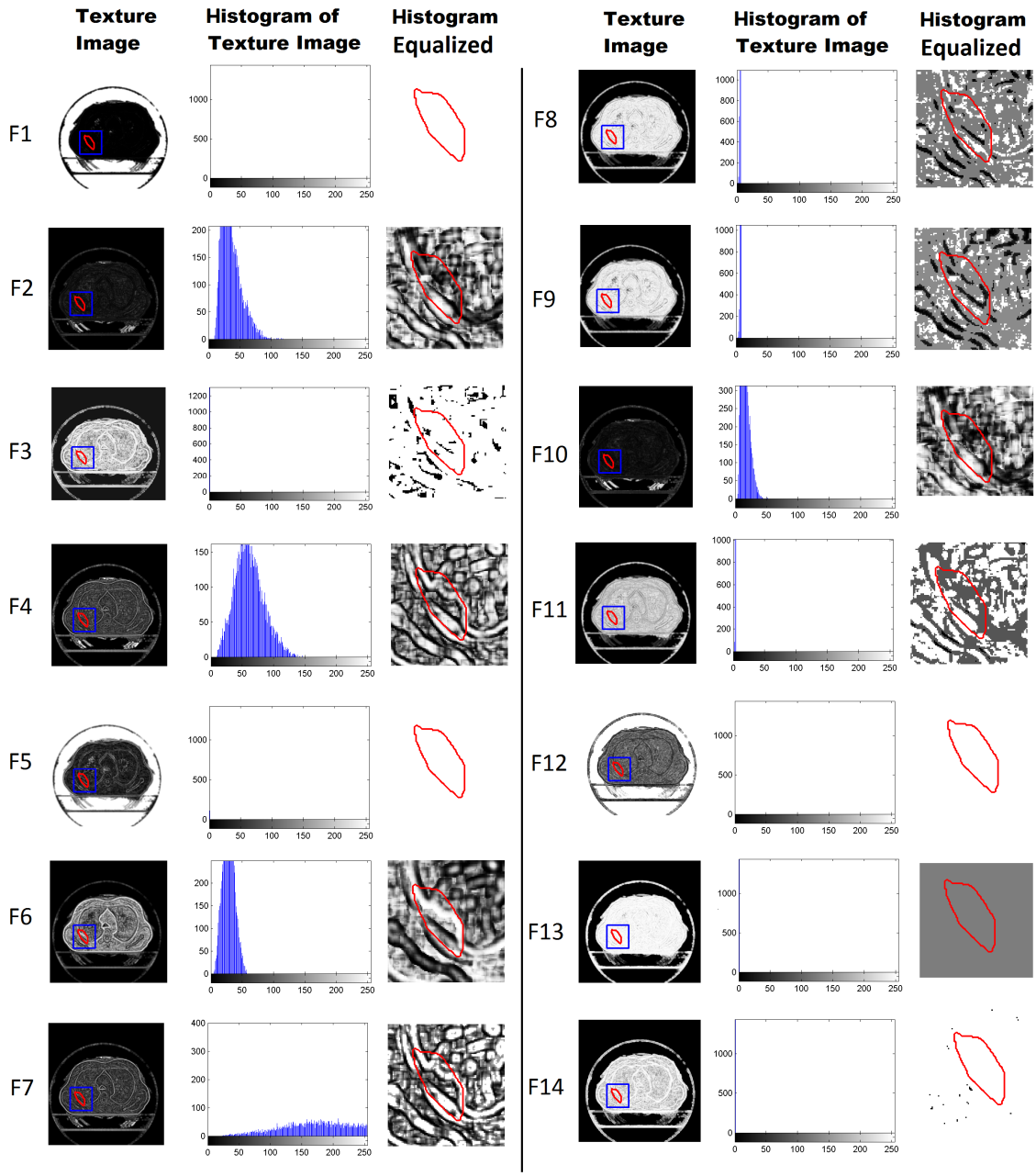

Figure 5.5: Haralick texture results for Patient 25 CBCT #1 Slice 58, F1: angular second moment, F2: contrast, F3: correlation, F4: variance, F5: inverse difference moment, F6: sum average, F7: sum variance, F8: sum Entropy, F9: entropy, F10: difference variance, F11: difference entropy, F12: information measures of correlation, F13: information measures of correlation and F14: maximal correlation coefficient.

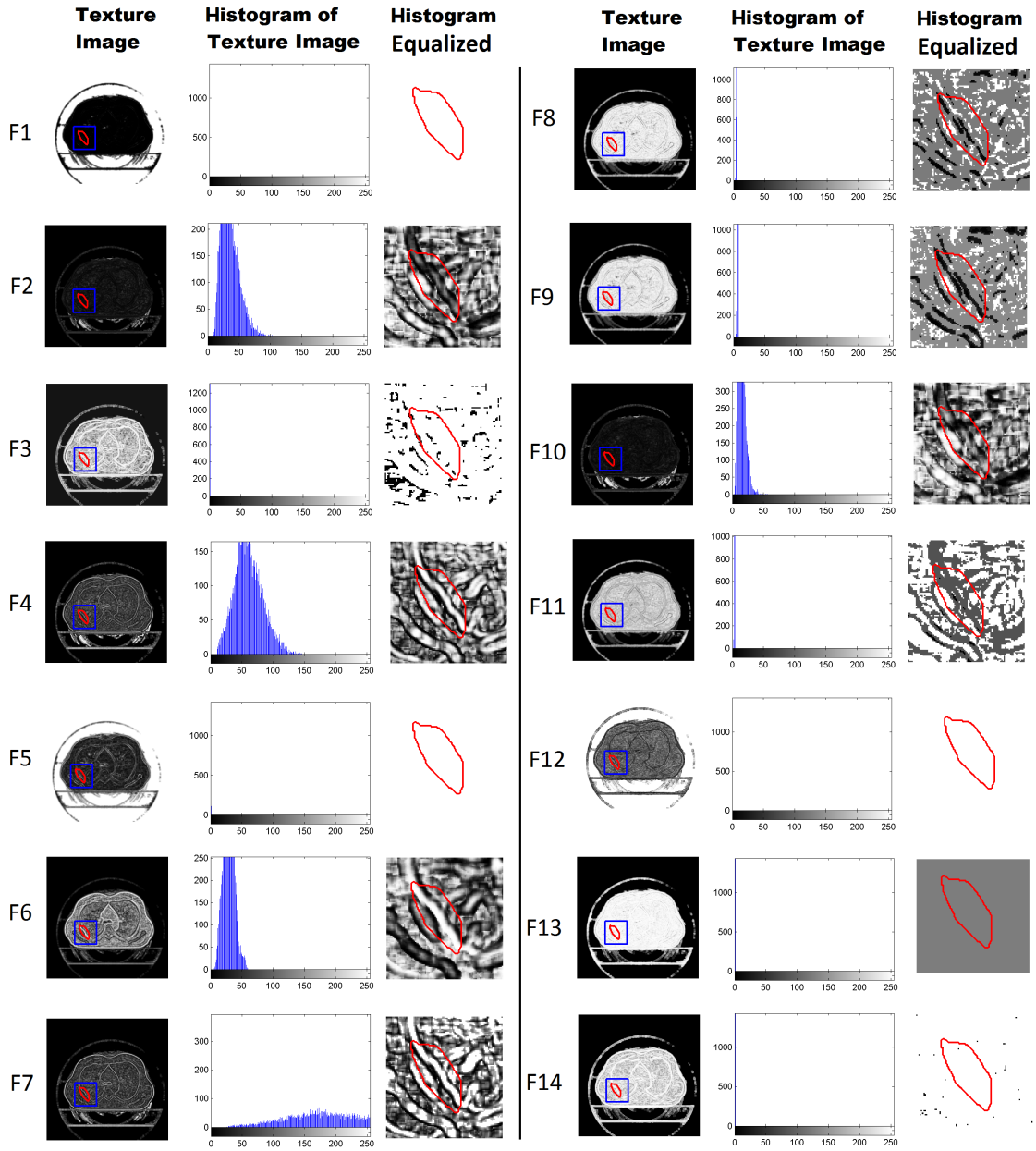

Figure 5.6: Haralick texture results for Patient 25 CBCT #10 Slice 58, F1: angular second moment, F2: contrast, F3: correlation, F4: variance, F5: inverse difference moment, F6: sum average, F7: sum variance, F8: sum Entropy, F9: entropy, F10: difference variance, F11: difference entropy, F12: information measures of correlation, F13: information measures of correlation and F14: maximal correlation coefficient.

It is interestingly that Figure 5.5 and Figure 5.6 both show the same behaviour for all texture features specificity for sum variance's well performance.

5.4 Level Set

Level set segmentation was applied to this data in fifteen different combinations. In total sixty seven contours as some models were applied on each of the fourteen texture features. These are listed in Table 5.1 and illustrated in Figure 5.7.

Model Name	Level Set Method	Image Used	Initialization of Level Set
Model a	Chan-Vese	CBCT	GTV
Model b	Chan-Vese	CBCT	GTV centre
Model c	Chan-Vese	PCA of 14 textures	GTV
Model d	Chan-Vese	PCA of 14 textures	GTV centre
Model e	Chan-Vese	Vector image of 14 textures	GTV
Model f	Chan-Vese	Vector image of 14 textures	GTV centre
Model g	Chan-Vese	Texture image F1	GTV
	Chan-Vese	Texture image F2	GTV
	Chan-Vese	Texture image F3	GTV
	Chan-Vese	Texture image F4	GTV
	Chan-Vese	Texture image F5	GTV
	Chan-Vese	Texture image F6	GTV
	Chan-Vese	Texture image F7	GTV
	Chan-Vese	Texture image F8	GTV
	Chan-Vese	Texture image F9	GTV
	Chan-Vese	Texture image F10	GTV
	Chan-Vese	Texture image F11	GTV
	Chan-Vese	Texture image F12	GTV
	Chan-Vese	Texture image F13	GTV
	Chan-Vese	Texture image F14	GTV
Model h	Chan-Vese	Texture image F1	GTV centre
	Chan-Vese	Texture image F2	GTV centre
	Chan-Vese	Texture image F3	GTV centre
	Chan-Vese	Texture image F4	GTV centre
	Chan-Vese	Texture image F5	GTV centre
	Chan-Vese	Texture image F6	GTV centre
	Chan-Vese	Texture image F7	GTV centre
	Chan-Vese	Texture image F8	GTV centre
	Chan-Vese	Texture image F9	GTV centre
	Chan-Vese	Texture image F10	GTV centre
	Chan-Vese	Texture image F11	GTV centre
	Chan-Vese	Texture image F12	GTV centre

	Chan-Vese	Texture image F13	GTV centre
	Chan-Vese	Texture image F14	GTV centre
Model i	Li	CBCT	GTV
Model j	Li	CBCT	GTV centre
Model k	Li	PCA of 14 textures	GTV
Model l	Li	PCA of 14 textures	GTV centre
Model m	Li	Texture image F1	GTV
	Li	Texture image F2	GTV
	Li	Texture image F3	GTV
	Li	Texture image F4	GTV
	Li	Texture image F5	GTV
	Li	Texture image F6	GTV
	Li	Texture image F7	GTV
	Li	Texture image F8	GTV
	Li	Texture image F9	GTV
	Li	Texture image F10	GTV
	Li	Texture image F11	GTV
	Li	Texture image F12	GTV
	Li	Texture image F13	GTV
	Li	Texture image F14	GTV
Model n	Li	Texture image F1	GTV centre
	Li	Texture image F2	GTV centre
	Li	Texture image F3	GTV centre
	Li	Texture image F4	GTV centre
	Li	Texture image F5	GTV centre
	Li	Texture image F6	GTV centre
	Li	Texture image F7	GTV centre
	Li	Texture image F8	GTV centre
	Li	Texture image F9	GTV centre
	Li	Texture image F10	GTV centre
	Li	Texture image F11	GTV centre
	Li	Texture image F12	GTV centre
	Li	Texture image F13	GTV centre
	Li	Texture image F14	GTV centre
Proposed Model			
Model o	Parallel Chan-Vese Li	Texture image F7	GTV

Table 5.1: All different proposed model of combining level set methods and texture features. In total there are fifteen different models resulting into sixty seven different contours per slice of CBCT.

Figure 5.7 illustrates the robustness of the proposed parallel level set (Model o) and other fourteen contours from Table 5.1. Models e and g also performing in expected shape. In the combination forms of level sets and texture features, the result of sum variance is shown in this figure. In general, other models do not have consistent performance for all images such as the ones shown in this figure. Therefore they were not deemed reliable enough for further study.

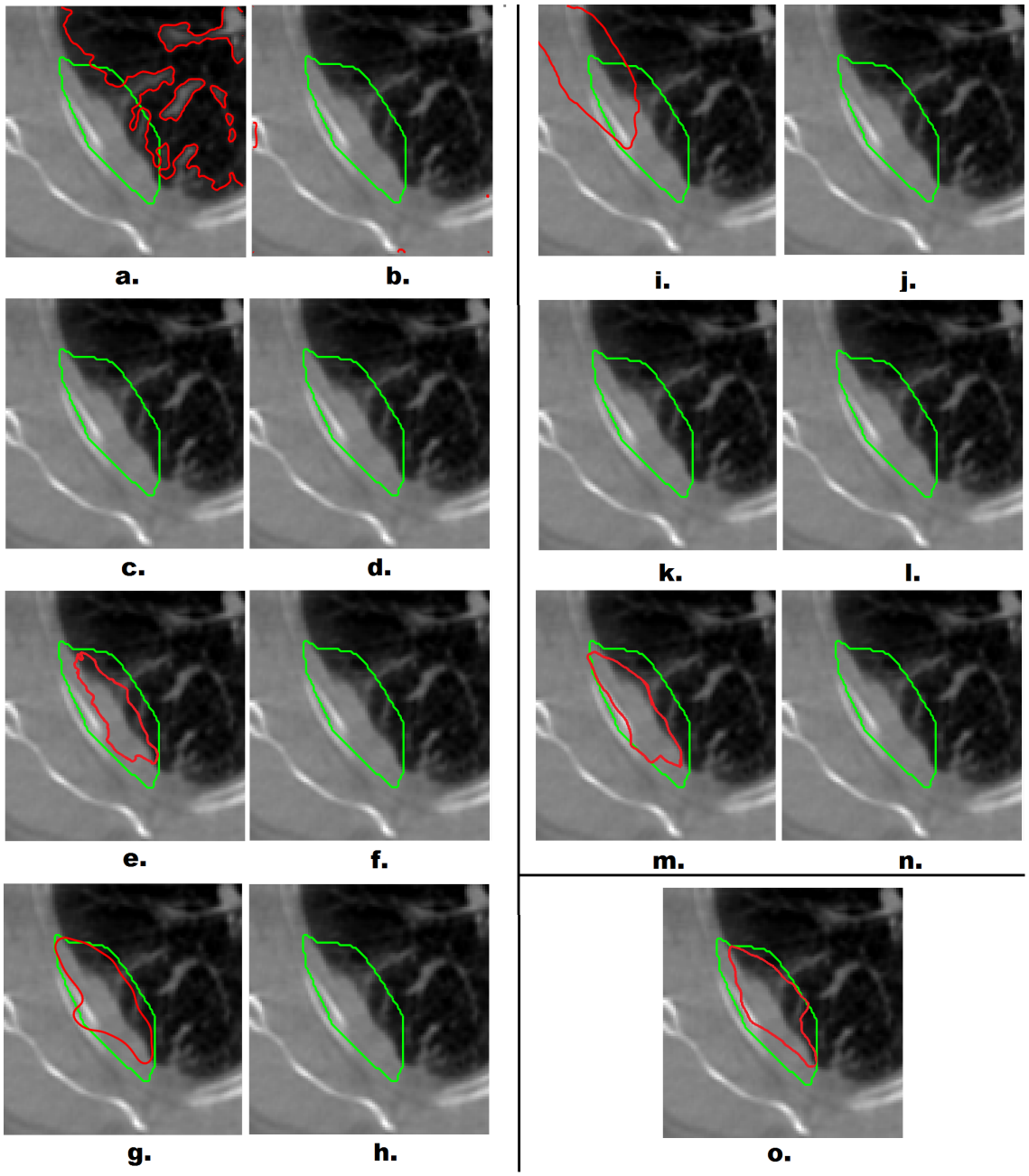

Figure 5.7: Fifteen different level set contours on CBCT #1 of Patient 25 mentioned in Table 5.1, where the green contour is the GTV on CT and the red contour is the result of level set.

5.5 The Combined Texture and Level Set Model

Texture images are likely to offer a better start for the level set, since the tumour cells are changing during treatment. Therefore tumour can be better monitored on different CBCTs using their texture images. The result of sum variance and level set for four different slices on #10 of Patient 25 is shown in Figure 5.8. There are two red contours in this figure, the inner one is the segmentation outcome of the proposed model and the outer one is the boundary of cropped-image for more optimal performance of level set and saving computation time.

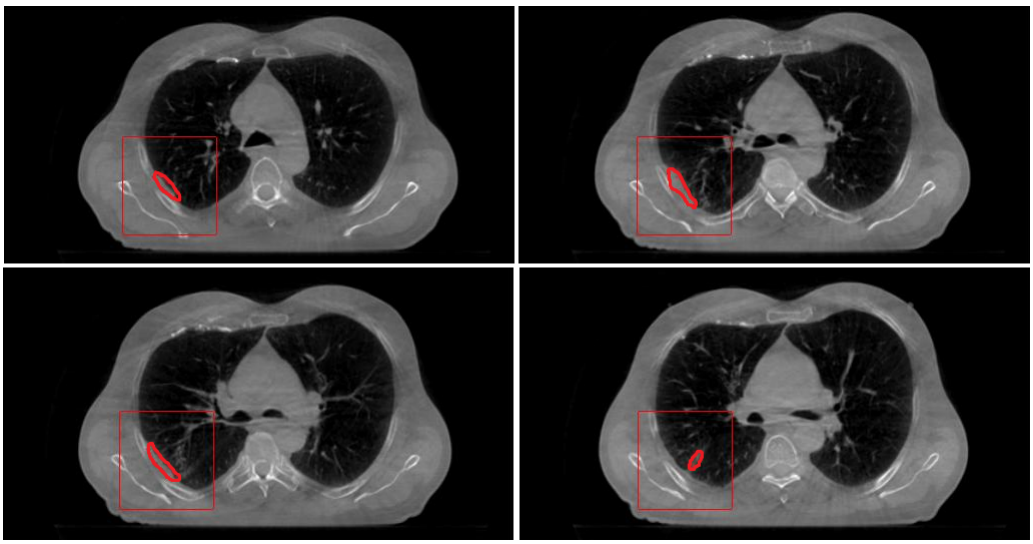

Figure 5.8: Chan-Vese method on sum variance image for four slices of Patient 25 CBCT #10.

The robustness of level set on top of sum variance texture segmentation of CBCT is perceptible here. Although the tumour position makes the level set convergence easy, the tumour's intensity values is very similar to the pleura side. Applying level set alone on the image instead of sum variance texture image cannot provide the results in Figure 5.8 due to similarity in intensity with the tumour's neighbouring tissues.

5.6 Qualitative Analysis of Patient 25 Data

The qualitative analysis is performed by the oncologist in two sessions. Firstly by comparing the results generated without the GTV on the CBCTs and secondly in a comparison after the oncologist contoured GTV on the CBCTs. In both cases the oncologist agreed with the proposed approach. As there were different combinations proposed for texture analysis and level set methods, in the first evaluation, the oncologist ranked the best three of models, Model a to Model n (models using only Chan-Vese or Li level set, not the proposed model which used both of them) as:

1. Sum variance + Li level set (Model m)
2. Sum variance + Chan-Vese level set (Model g)
3. Vector-texture images of Chan-Vese level set (Model e)

The quantitative analysis as well as time cost for calculation was compared, with Model e and Model m both considerably quicker than Model g. The average calculation time per slice for level set segmentation can be seen in Table 5.2.

Model m	Model g	Model e
20 seconds	30 seconds	30 minutes

Table 5.2: Average time of execution of proposed different combinations selected by the oncologist per registered CBCT slice.

The time of execution was measured on average for a 100×100 pixels CBCT image (cropped RIO based on common PTV area for all slices) over fifty slices. As mentioned in Section 4.3, the time of execution can be sacrificed for higher accuracy but due to tuning difficulties in level set parameters, Model g is not favourable. Also Chan-Vese level set in Model g (oncologist's choice 3) took an unacceptably long time to compute.

Considering the robustness of the model and the accuracy of detecting tumours the top three selected models (two by the oncologist and the proposed model) are:

1. Sum variance + Parallel level set (Model o)
2. Sum variance + Chan-Vese level set (Model g)
3. Sum variance + Li level set (Model m)

Figures 5.9 to 5.11 show the performance of these three models is robust and similar. In these figures the results of the proposed model on CBCT #10 are acquired without any assistance from the GTV on CBCTs, only GTV on planning-CT was used for their initialization. The same framework in Chapter 6 for all other forty nine patients was applied where the GTV on CBCTs do not exist.

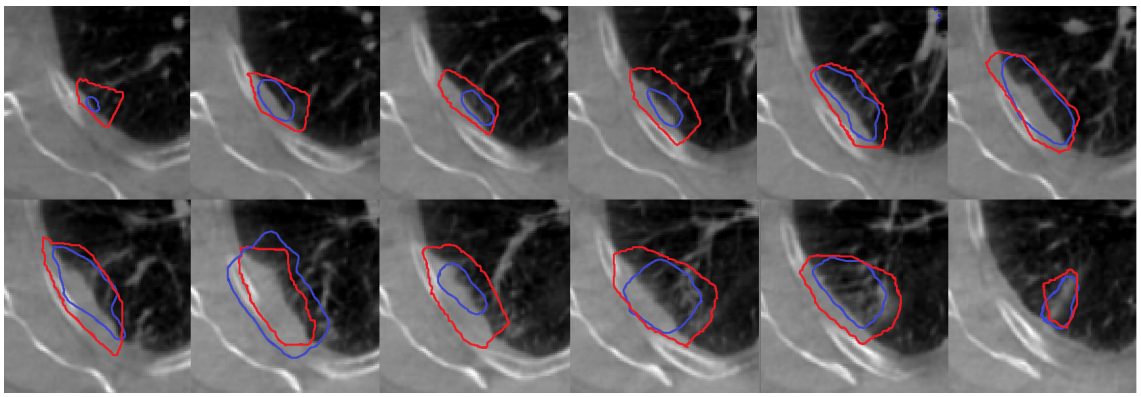

Figure 5.9: The proposed Model o on CBCT#10 Patient 25, where the red contour is the CT's GTV and the blue contour is the result of level set.

In some slices, the level set detects larger areas which seem to be blood vessels at first glance but are in fact the tumour affecting other regions. Texture analysis helps in this situation to define the difference between tumour, blood vessel or cancerous tissues attached to blood vessel. The power of texture analysis is also limited on CBCT images because of their poor quality but still can not be ignored.

The results of three best models are almost very similar. Figure 5.9 which illustrates Model o can be compared with both Figure 5.10 and Figure 5.11 since it takes the advantage of both level set methods used in Model g and Model m while using sum variance similar to them.

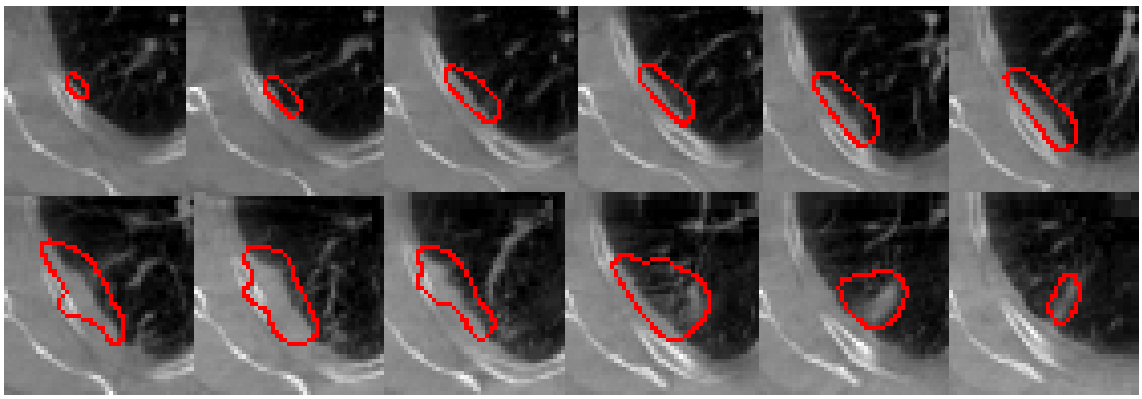

Figure 5.10: The proposed Model g on CBCT#10 Patient 25, where the red contour is the result of level set.

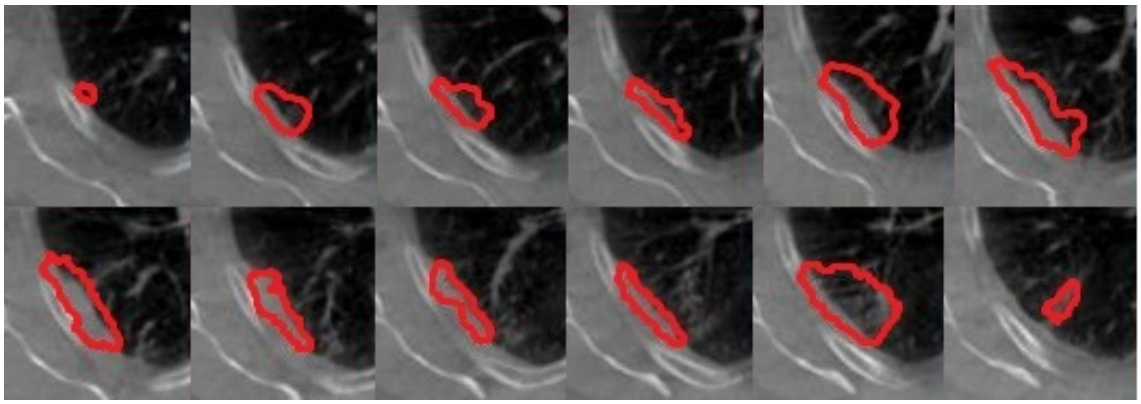

Figure 5.11: The proposed Model m on CBCT#10 Patient 25, where the red contour is the result of level set.

5.7 Quantitative Analysis of Patient 25 Data

As shown in Figure 5.12, parameter setting was tested on CBCT #10 data. In this case the reference contour from the oncologist is drawn in blue and texture combined by level set contour is delineated in red. The Dice coefficient between the clinical contour and segmentation contour for this case is 85%.

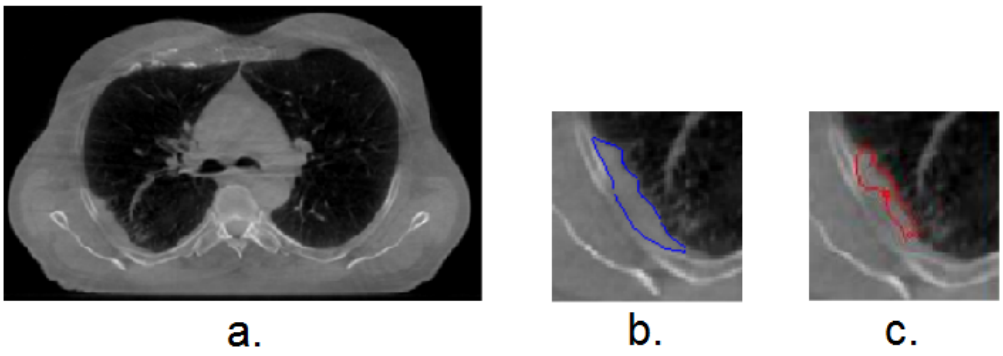

Figure 5.12: Registered CBCT #10 of Patient 25 compared to the final segmentation proposed model, a. registered CBCT #10, b. GTV on CBCT #10 and c. combined sum variance and Chan-Vese model-Model g.

The oncologist was satisfied that the small differences between GTV and the proposed model are to be expected. Therefore, a Dice coefficient with an error of $\pm 5\%$ is acceptable since the GTV delineation is the nearest estimate by the oncologist which might be slightly different in the eyes of other oncologist. Also GTV is not used for the shaping the radiation during treatment but PTV is used. This coefficient is widely used to compare contour segmentation accuracy in image processing [93].

The shrinkage of the tumour based on the results obtained from the proposed models on CBCT #10 is approximately 30%. This amount of shrinkage is almost the same between the main GTV on CT and GTV on CBCT #10 as shown in Figure 5.13.

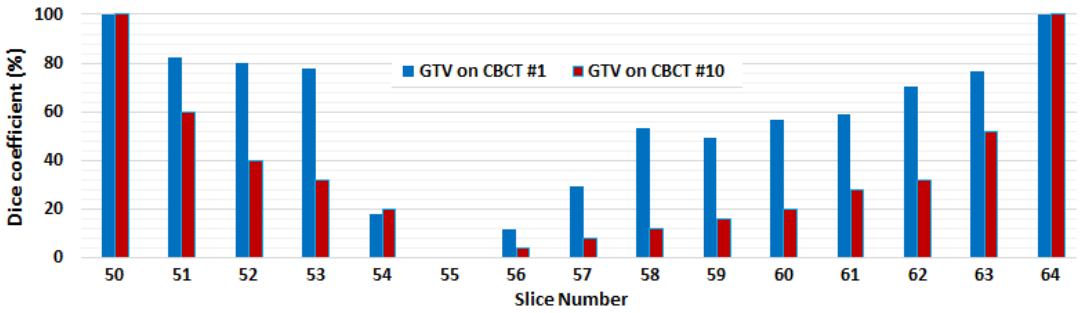

Figure 5.13: Change of GTV on CT compared to GTV on CBCTs, the blue bar indicates the similarity for CBCT #1 and red represents CBCT #10.

As shown in Figure 5.14, the Dice coefficient between CBCT #1 and #10 with their relevant GTV for different slices on average is 90% and 93% respectively for the best three models.

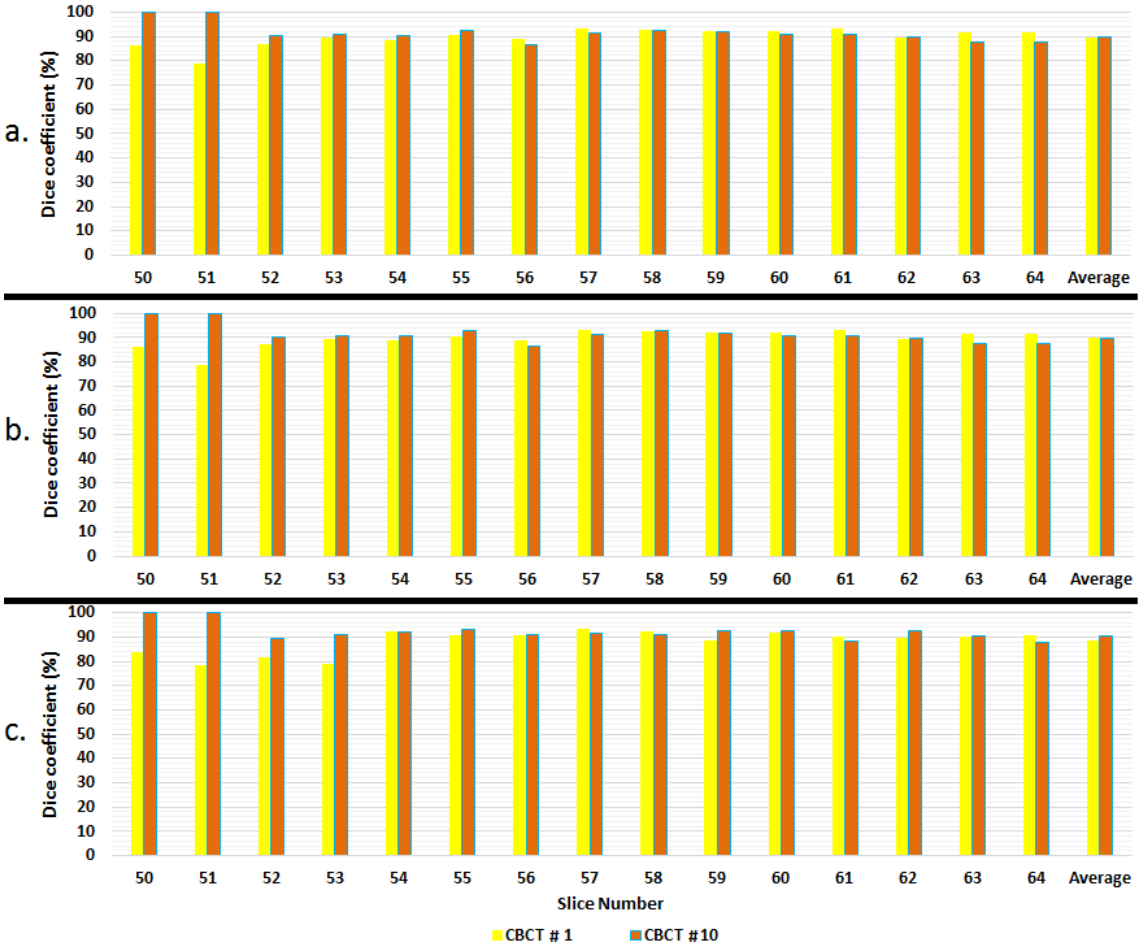

Figure 5.14: Dice coefficient comparison between GTV on CBCTs and different proposed models, a. Model o, b. Model g and c. Model m. The yellow bar indicates the similarity for CBCT #1 and brown represents CBCT #10.

The average of GTV similarity on each fraction and level set supports the view that the proposed method is accurate. It is worth mentioning that contouring in medical imaging, especially in CBCT imaging, can be reliable way of identifying the presence or absence of tumour, however, the accuracy may be limited. Therefore some variation of accuracy is always acceptable in comparisons.

The level set parameter setting was carried out with assistance from the closest Dice coefficient between GTV on CT and the proposed model on CBCT #1. By finding these parameters, the level set was tuned for better performance on CBCT #10. Figure 5.15 illustrates the Dice coefficient between the main GTV on CT with the proposed model on CBCT #1 and #10 for different slices.

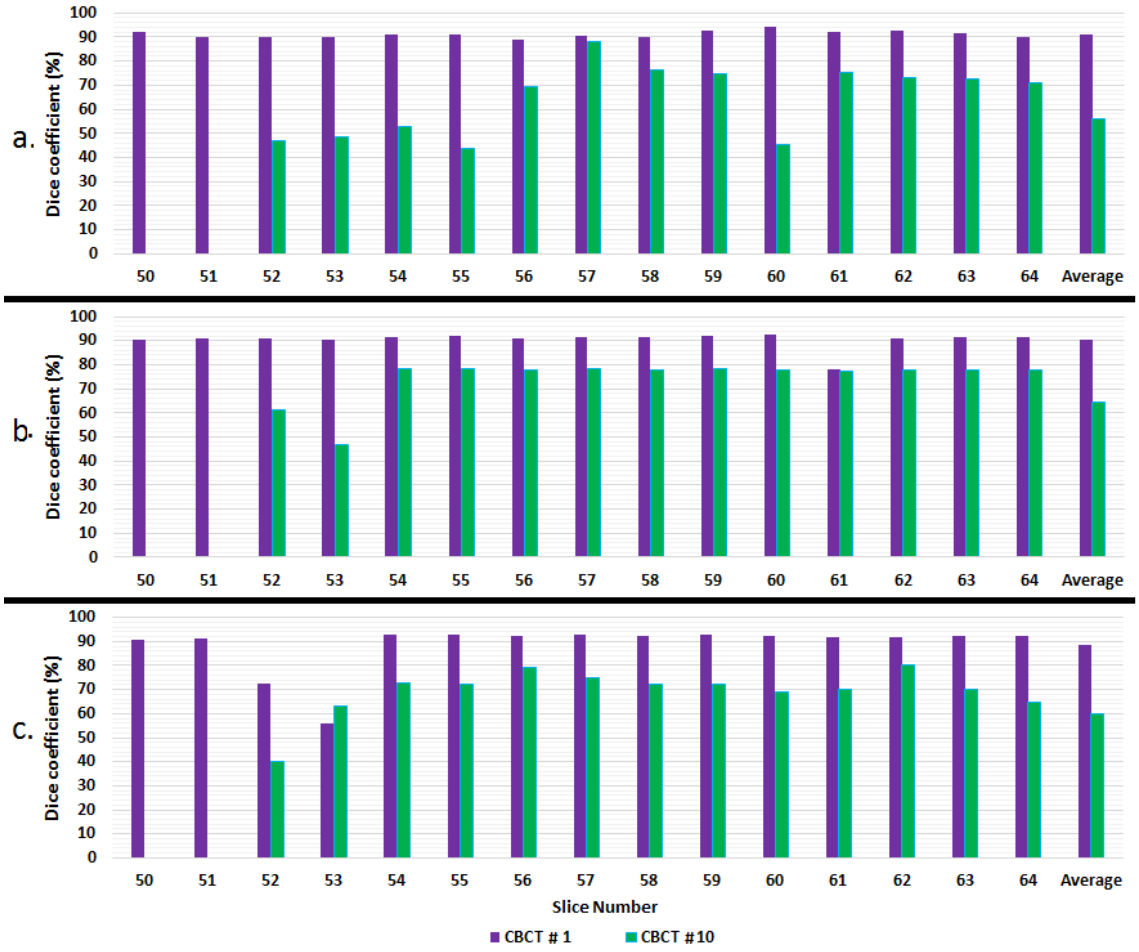

Figure 5.15: Dice coefficient comparison between the main GTV on CT and different proposed models, a. Model o, b. Model g and c. Model m. The purple bar indicates the similarity for CBCT #1 and the green represents CBCT #10.

The proposed models can be applied on more complex tumours without any ground truth on follow-up images. The success of this approach still depends on GTV prior shape from the CT before treatment since level set can be dependent to the initialization and its parameter setting. The more recursive parameter tuning used, the better the result from level set will be.

As discussed in Chapter 2, the aim of image segmentation is to provide assistance to clinicians. Efficient de-noising, image enhancement, registration and segmentation methods can assist in online or offline adaptive radiation planning in RT and therefore lead to IGART. In IGART, the treatment plan changes either within or between fractions. Therefore, more accurate treatment is delivered to tumour regions and a smaller dose is delivered to healthy tissues. However, it is not sufficient to generate adaptive radiation planning using only CT images. Information from CBCT images is also required. Further, a robust and automatic segmentation approach that can use all of the segmentation information as prior knowledge and generate accurate GTV contours is needed. However,

there is still no generally applicable procedure for online ART in clinical practice. In this project, the information extracted from CBCT images might not be accurate enough to be used in IGART but can be used as an alarm for oncologists to reconsider the treatment plans in case of tumour growth during RT treatment.

5.8 Extension to Offline Adaptive Radiotherapy

Offline ART allows changes to be made between fractions (daily) and also helps to adjust planning for the remaining RT sessions in a treatment cycle. The frequency of applying online or offline ART is dependent on the type of treatment. In this research, the clinicians seek information about changes of tumour in CBCT#10 to monitor the effect of the treatment one third of the way through therapy.

The information obtained in Section 5.5 showed considerable shrinkage in the tumour volume. Since it shrank by 30%, the medical team can continue the treatment from CBCT #11 with a smaller shape of tumour, meaning they can focus the RT on a smaller volume.

The proposed model can be applied on CBCT #20 to compare with GTV and CBCT #10. New considerations can be applied for the last 10 treatments. On the last day of treatment, CBCT #30, the proposed model can be applied again. If the cancer is still progressing at this point, new treatment plans could be proposed.

For Patient 25, the information of the GTV on CBCT images was obtained for the purpose of this thesis. In general, oncologists do not contour CBCT for all cases, however they could use the information in the proposed model (for Patient 25) to decrease the PTV size. By doing this healthy tissues would be at less risk of radiation. The amount of minimization (or maximization in the opposite situation) depends on the decision of the medical team for different patients.

Current lung cancer RT accuracy can be improved if the proposed model is applied to every fraction of the CBCTs and the results of segmentation for the first 10 fractions show a consistent trend. For the case of consistent outcomes, the doctor would have more confidence in applying the model in offline ART and the results for the next 10 fractions.

The proposed model can be extended to other offline ART applications such as other medical image modalities as well as other clinical RT applications. Irrespective of the ground truth existing or not, the proposed model can assist the clinicians and better inform their decision making. A typical framework for ART is shown in Figure 5.16.

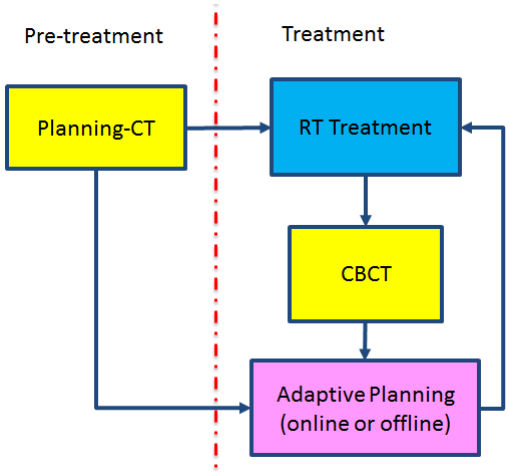

Figure 5.16: The typical framework for an ART process.

5.9 Conclusions

The proposed method is based on level set methods and texture features in determining the tumour position during lung cancer RT based on CBCT images. To date, no segmentation model can detect lung tumours on CT or CBCT images with 100% accuracy due to the poor intensity variation of these images on soft tissues, although there can be some changes on a sequence of images over different periods of time (i.e., fractions). Each time a patient experiences RT, the texture of the lung may change compared to the previous session due to progression of the cancer or a positive effect of the RT. Knowing this, different images taken at different times of the same position of a patient during treatment was considered, using texture analysis to find out the difference in these textures during course of treatment by applying level set methods on them.

In this chapter, Patient 25 was chosen as an example to illustrate the robustness of the proposed models. This chapter illustrated that the level set method based texture features is capable of generating a more accurate boundary with a smaller chance of distortion while converging. The distortions were identified by minimizing the parameter error based on the similarity function of Dice coefficient between corresponding parameters which were defined manually based on CBCT #1 and GTV.

The proposed combined texture and level set model demonstrated an accuracy of almost 90% for Patient 25. This model might not be purely accurate as there is no gold standard in medical imaging in general. However, it would provide a great help to an oncologist in knowing the condition of the patient after each RT treatment. Last but not the least, this chapter discussed that by applying the proposed model on every fraction of CBCT and having consistent results, this method could be used in offline ART.

Chapter 6

Texture and Level Set Model for Lung Cancer Analysis on CT and CBCT of 49 Patients

6.1 Introduction

This chapter uses the combined texture and level set model proposed in Chapter 5 to identify the GTV on CBCT images of forty nine patients from the lung dataset. Initially, all image processing work carried out on the lung dataset, starting with image conditioning, is discussed. Then, in order to map the GTV from the CT to CBCT images, a registration model was applied based on RT data included in the CBCT data used by radiographers during treatment. This registration is the gold standard in RT because it has real translocation of the patient position. By having the correct position of the original GTV (from CT) on CBCT #1, and applying the proposed segmentation model, a suitable range of level set parameters are found. Finally, this tuned proposed segmentation model was presented to the oncologist for visual evaluation in order to verify its accuracy. The oncologist also had access to the patient case history while evaluating the results. The high acceptance score given by the oncologist to this study/analysis is verification of the effectiveness of the approach.

Figure 6.1 illustrates a general schematic of medical image analysis. Image acquisition, enhancement, segmentation, feature extraction, decision making and validation are the most commonly used steps in medical imaging. Although not all steps were required here, this chapter tries to convey the whole analysis procedure applied in this work. In Section 6.2 the test images from the data are shown, and their characteristics are discussed. Section 6.3 presents the registration procedure between the CT and CBCT images. The GTV contours on CT images are used on CBCT images as an initialization of level set, therefore registration is needed to map the relevant contours of each slice from CT to its equivalent CBCT. Registered contours on the CBCT images were assessed by a clinician as well as being tested by evaluating the distance ratio of airways to the vertebra.

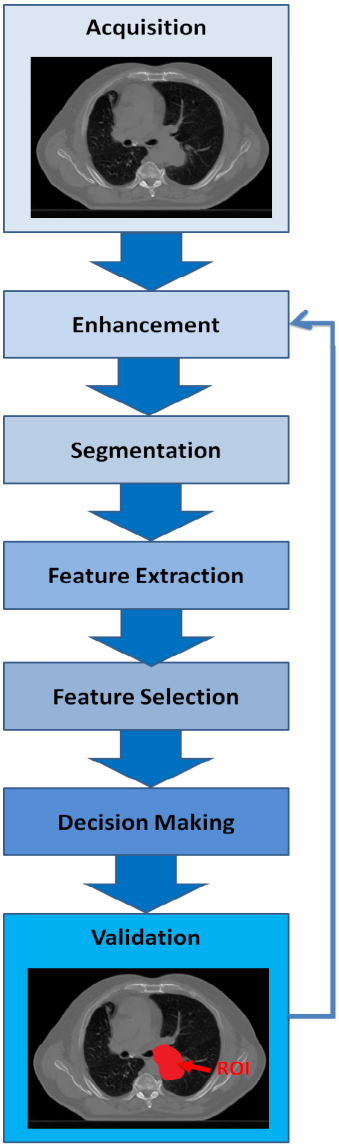

Figure 6.1: Flowchart of medical image analysis.

In Section 6.4, texture analysis is discussed as a combined texture with level set model which is proposed in this work, applies level set on the textured images. As lung images are more textured than brain and other medical images, fourteen Haralick texture features are calculated to generate the new image. Level set is applied on the textured images to find out the behaviour of level set on a textured image which highlights the texture in the image more. In texture analysis, the areas of image with low intensity variation are called smooth textured and the areas with larger amounts of variation are rough textured. The performance was assessed by clinicians since the quality of CBCT images is very poor, hence oncologists cannot contour them. The proposed algorithm in this study can help doctors to understand any change in the tumour. The results of the combined texture and level set are discussed mainly in Section 6.5.

6.2 Lung CT and CBCT Data Details of Patients

The main dataset used in this research is based on two modalities, planning-CT and follow up CBCT taken at different fractions of the treatment. The combined texture and level set algorithm formed an analysis framework that could be used as an RT assessment factor, it is suitable for extension to ART but without any gold standard it would not be pragmatic. This dataset includes fifty patients who suffered lung cancer and underwent an RT in 2010 and 2011 at the Western General Hospital, Edinburgh, Scotland. All of these patients went through the whole course of treatment over approximately four weeks. CBCT #1 and #10 are most commonly used, although some patients have more fractions of CBCT data available. Full information for all fifty patients is described in Appendix A.

All CT images were acquired with 512×512 pixels and a pixel size of $0.977mm \times 0.977mm$. All CBCT images were acquired with 384×384 pixels and a pixel size of $1.172mm \times 1.172mm$. The number of CT and CBCT image slices containing the tumour volume varied between different patients. A board-certified radiation oncologist evaluated all images and the contoured GTV, CTV, PTV and OAR. The CT images were acquired with a General Electronics Medical scanner and CBCT images by a Varian Medical Systems On-Board Cone-Beam CT (OBI CBCT which is a type of CBCT scanner embedded inside a LINAC).

GTV contours are available for all fifty patients on their planning-CT images but not on CBCT images as the poor quality of CBCT restricts the oncologists as noted previously. They do not expect much change in CBCT #1 as this series is acquired before planning-CT and immediately prior to comencing RT, therefore the tumour has not undergone any X-ray treatment. The main concern of the medical team is the tumour response in CBCT #10. This occurs when the patient has had almost 30% of treatment. At this stage, having any indication about the tumour's progression or regression can be a great help to physicians in monitoring the response of the tumour to initial RT sessions. Since in most cases observing CBCT alone can not give any indication of tumour shape to the oncologist, applying the combined texture and level set model proposed in this thesis can be a beneficial help for clinicians.

Table 6.1 lists 3 patients' details only which are used for demonstration purposes in this Chapter, Patients 25, 26 and 34. The reason for choosing these 3 patients were due to the visible shrinkage of tumour on CBCT images of Patient 25 and 26. Also Patient 26 and 34 were chosen as most of the dataset were similar to them, with cancer seen in different tissues. Patient 25 was discussed in Chapter 5 in detail. Patient 26 responded positively to RT, noticeably in some slices and Patient 34 is the final case, which had collapsed lungs during treatment.

Case	Modality	Slice No	Date	Pixel Size	Slice Thickness
Patient 25	CT	130	10-05-2011	512 ×512	3mm
	CBCT # 1	64	23-05-2011	384 ×384	1mm
	CBCT # 10	54	10-06-2011	384 ×384	1mm
Patient 26	CT	126	05-10-2010	512 ×512	3mm
	CBCT # 1	52	18-10-2010	384 ×384	3mm
	CBCT # 10	54	01-11-2010	384 ×384	1mm
Patient 34	CT	137	28-06-2011	512 ×512	3mm
	CBCT # 1	53	12-07-2011	384 ×384	1mm
	CBCT # 3	53	14-07-2011	384 ×384	1mm
	CBCT # 4	53	15-07-2011	384 ×384	1mm
	CBCT # 6	53	19-07-2011	384 ×384	1mm
	CBCT # 7	53	20-07-2011	384 ×384	1mm
	CT	127	14-07-2011	512 ×512	3mm
	CBCT # 11	53	26-07-2011	384 ×384	1mm
	CBCT # 14	53	29-07-2011	384 ×384	1mm
	CBCT # 17	53	03-08-2011	384 ×384	1mm

Table 6.1: Details of 3 out of fifty patients from lung cancer dataset.

In Figure 6.2, Patient 26's planning-CT and relevant CBCT #1 and #10 are shown, even though the tumour is in the middle of the lungs, the positive results are obvious in CBCT #10. In Figure 6.2.a. the GTV is shown in red and on CBCT images the estimated region of GTV is circled in red colour as well to highlight the shrinkage of tumour during RT.

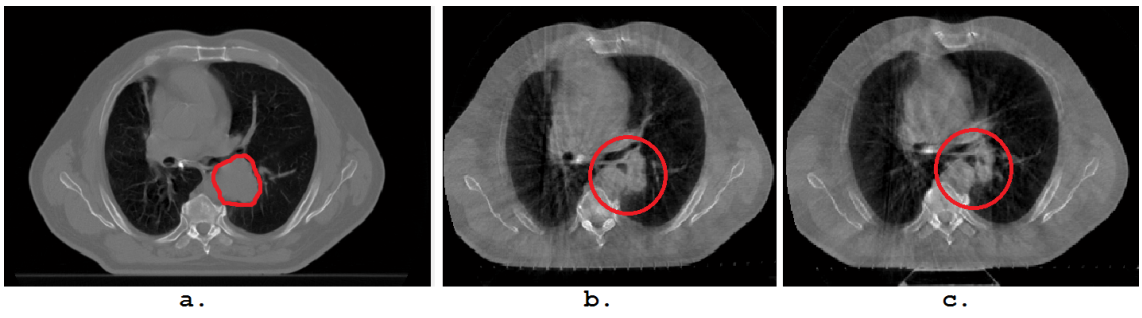

Figure 6.2: Patient 26, a. one slice of the planning-CT with the clinical GTV contour shown in red, b. the CBCT #1 after 13 days of planning, before applying any RT treatment (GTV region is circled in red) and c. the CBCT #10 after 26 days of treatment (GTV region is circled in red).

Patient 34 is the most complicated case among all patients as they suffered from a collapsed lung, or atelectasis, during RT. Briefly, this is when the lung evacuates all air suddenly and shrinks. Air enters the spaces between lungs and pleural usually happens due to the presence of a hole in the lung. This can occur for different reasons such as external injury, for example a car accident, or internal lung diseases, such as cancerous lesion expansion.

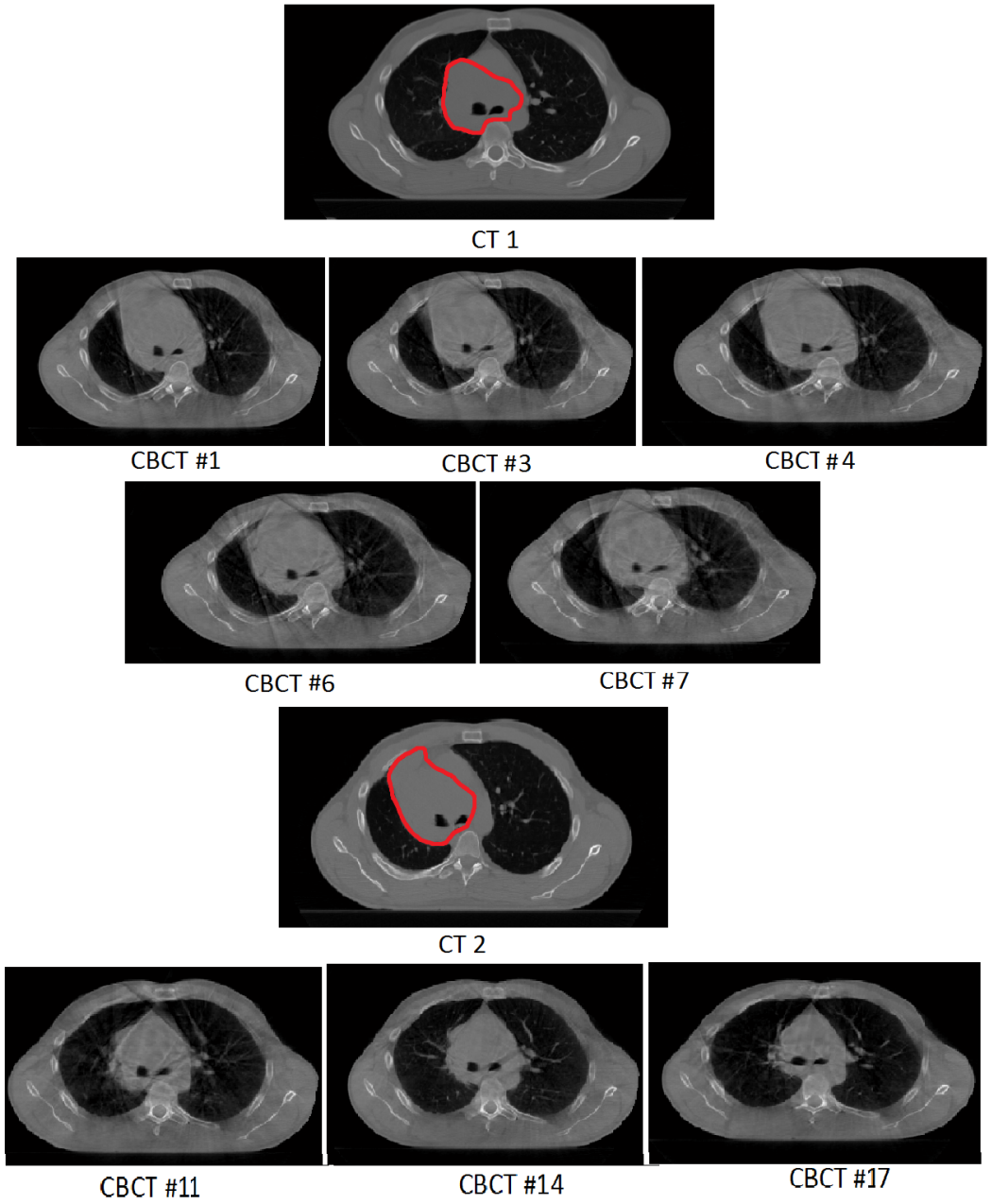

Figure 6.3: Lung tumour state during RT for Patient 34: This patient had two different planning-CTs with their relevant GTV on each scan as the patient suffered from collapsed lung during RT. This figure shows different fractions of CBCT with respect to the GTV of their relevant CT.

Treatment for Patient 34 was stopped on 12-07-2011 and the lung re-inflated during XRT. Treatment was then re-planned on 14-07-2011. Since the health situation of this patient was an emergency, the medical team was not able to provide a new GTV quickly. The treatment was therefore continued with the first GTV from first planning-CT on 28-06-2011 for a few fractions. From CBCT #11 on 26-07-2011 onwards the treatment continued using new GTV delineated on the new planning-CT. In Figure 6.3 illustrates that Patient 34 had two different planning-CTs with their relevant GTV on each scan as the patient suffered from collapsed lung during RT. This figure shows different fractions of CBCT with respect to the GTV of their relevant CT and illustrates the tumour shrinkage on CBCT #11, #14 and #17.

Before moving to the image processing/analysis sections, there are some medical notes which are essential to point out:

1. The first and foremost consideration is oncologists always include airways inside the GTV if the tumour is attached or around airways. Figure 6.4 shows the GTV and PTV delineated by the oncologist on one slice of CT with large tumour that can be used as the ground truth for comparison of level set and GTV. This example is chosen to show that the airway is also included in the GTV and PTV even though the tumour is not growing inside the airway. The reason for this and similar cases is twofold. First, because there is nothing inside the airway, therefore there will be no harm from the radiation and second, in case of further growth of tumour in the airways.

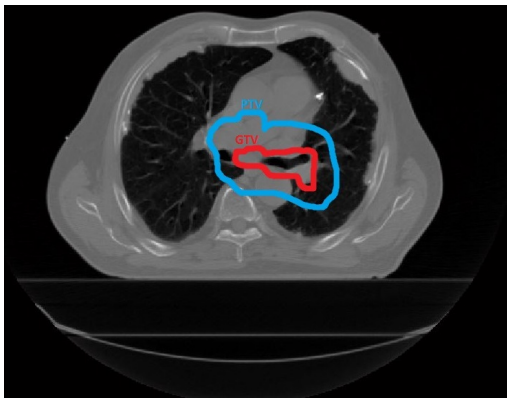

Figure 6.4: GTV and PTV delineated by the oncologist.

2. The second note is that the radiation dose is based on PTV not the GTV as discussed in Section 1.2. By improving IGART this penalty can be reduced and rescue healthy tissues from further radiation.
3. A final important principle is that the patients suffering from cancer and treated by RT will most likely face weight loss. Therefore images of the same patient might show different volume per slice compared to previous treatments.

6.3 Registration of CT and CBCT Dataset

Registration is a necessary step in medical imaging to allow clinicians to compare images from different time intervals and different modalities. From an image processing point of view, it is very challenging to find the transformation between different images. As mentioned previously, in medical treatment it is critical to adjust the patient's body to the proper position. In RT, radiographers try to capture CBCT images and record the translation of patient position compared to the planning-CT images. In other words, radiographers register CBCT to CT when preparing the patient for treatment. Finding this translation is vital for transferring the tumour delineated shape by the oncologist on CT to CBCT before starting any radiation. All this information regarding the patient's position and translation is saved in the patient's DICOM data and can be used in image processing to find the most accurate registration between images. It was calculated as follows.

The CBCT images were registered to CT images by a transformation matrix generated as a gold standard. This registration before segmentation helps to transfer the proper GTV to CBCT images. In this registration three transformations happen. CBCT images should be transferred to CT coordinates, but need to be transferred to the centre of CBCT and then transferred based on image, patient position and patient orientation. Next, the radiology translation file, attached to each CBCT, can be used to find the changes between CBCT and CT to bring the image into the origin domain/space of CT. The last translation is based on embedded information in the CT images which define the patient current position compared to their original position. DICOM data embedded in CBCT images contains the values of rotation and translation of the patient body for comparison to CT images.

As shown in Figure 6.5, 3 transformation matrices, T_1, T_2 and T_3 (all of them 4×4), are the key parts to calculate the mapping between the reference and target images. T_1 and T_2 can be calculated using Equation 6.1 on DICOM information from the reference and target images respectively. T_3 is based on the information from the reference coordinate system (RCS) which are the DICOM data embedded in CBCT measured and recorded by the radiographer.

$$T_1 = \begin{bmatrix} X_x\Delta i & Y_x\Delta j & 0 & S_x \\ X_y\Delta i & Y_y\Delta j & 0 & S_y \\ X_z\Delta i & Y_z\Delta j & 0 & S_z \\ 0 & 0 & 0 & 1 \end{bmatrix} \tag{6.1}$$

where S_{xyz} are the three values of the Image Position Patient (DICOM tag), which indicates the location from the origin of the Radiation Calibration Service (RCS) in *mm*. X_{xyz} are the first three values of the Image Orientation Patient (DICOM tag) and Y_{xyz} are the last three values of the Image Orientation Patient (DICOM tag). Δi and Δj are the pixel

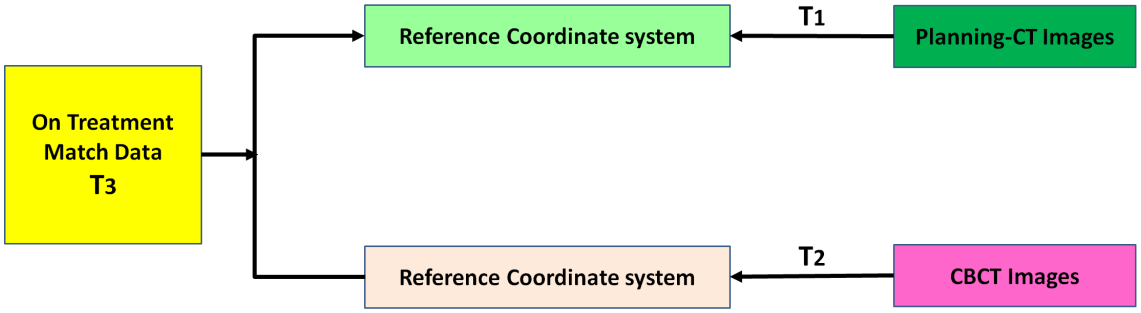

Figure 6.5: The relationship between the reference image (planning-CT), the target image (CBCT) and their RCS. Here T_1 is the transformation matrix from the planning-CT image to the RCS, T_2 is the transformation matrix from CBCT image to the RCS and T_3 is the transformation matrix from the RCS of the target image to the RCS of the reference image.

size, which can be extracted from Pixel Spacing (DICOM tag). After reading T_3 from an RT registration file generated by the radiographers, the transformation matrix T, which represents the gold standard in rigid registration, can be calculated using Equation 6.2.

$$T = T_1^{-1} T_3 T_2 \tag{6.2}$$

Figure 6.6 illustrates an example of a registration algorithm in which the 512×512 planning-CT image from Patient 5 was used as the reference image and the 384×384 CBCT #11 of the same patient was used as the translated image. This figure shows CBCT images before and after registration. Medical images usually have the same orientation because they were acquired from patients laid on a couch, which makes the orientation of patients relatively stable between different time points. As a result, rotation parameters of the rigid registration defined by radiographers or generated by the presented algorithm were both 0 for CBCT data sets.

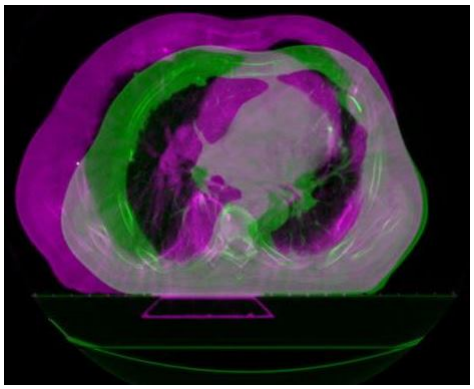

Figure 6.6: The reference CT image with dimension of 512×512 in green and resized CBCT image to 512×512 with original dimension of 384×384 in purple before registration.

This registration uses the most accurate values to find the isocentre of the patient before CBCT image acquisition. Clinical registration for Patient 30 is shown in Figure 6.7. The result of registration is prominent although there are visible errors which may be slight shape variations between the reference and target image because they were acquired at different time points from different modalities.

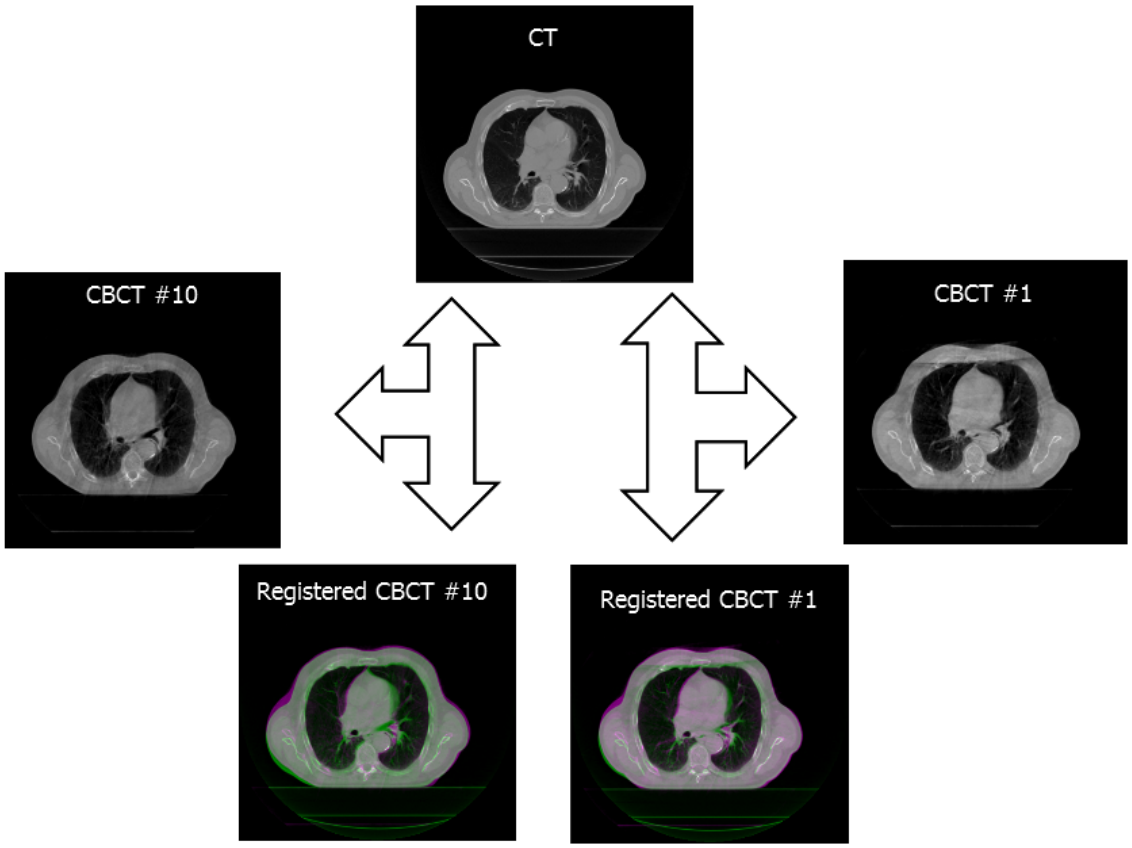

Figure 6.7: CBCT #1 and #10 registration to the planning-CT for Patient 30.

Clinical Trick for Validation of Registration

The validation of the registration in this work is performed by measuring the ratio between airways and the vertebral column. This is the assessment method applied by the oncologist who evaluated this research. The diameter of the vertebral column is always a fixed value for any individual during his/her life, but the length of vertebral shrinks as the human ages. Therefore, it is always the best method of measurement for validating the registration results on CBCT. The diameter of vertebral and the height between vertebral and airways is shown in Figure 6.8.

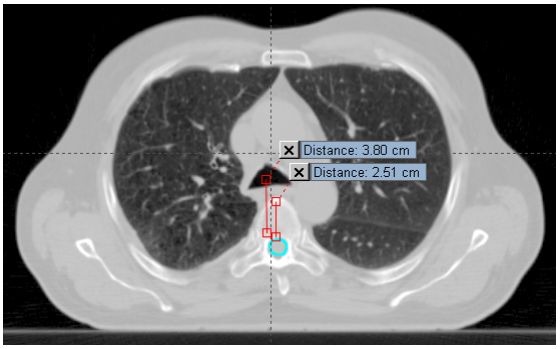

Figure 6.8: Fixed ratio between distance of airways and vertebral can be measured in each slice of CT and CBCT.

6.4 Texture Analysis Pre-Segmentation of Lung Dataset

Texture analysis has been widely used for characterising the irregularity in medical images and for extracting quantitative information not necessarily visible to the naked eye. In this work second-order texture features introduced in Chapter 3, based on the GLCM in [94], were calculated on the GTV region present on each CBCT. The pixel values on the CBCT images were replaced by the texture feature values and these textured images were used as the image for Chan-Vese level set evolution. Figure 6.9 shows examples of the CBCT images and the contours produced by level set with and without being combined with textured features. Columns b. and c. compared when level set only was applied on CBCT images and when it was applied on sum variance of the same image.

Of the fourteen features used, the image produced by the sum variance feature consistently produced the best results. This is shown in Figure 6.9, where the blue contour is the clinical contour and the red contour is the level set. Patient 3 has a small piece of tumour on his left lung which level set alone was not able to detect. but by applying level set on top of sum variance, the tumour is picked up. It is a small example which shows the improvement of level set when it is combined with texture analysis.

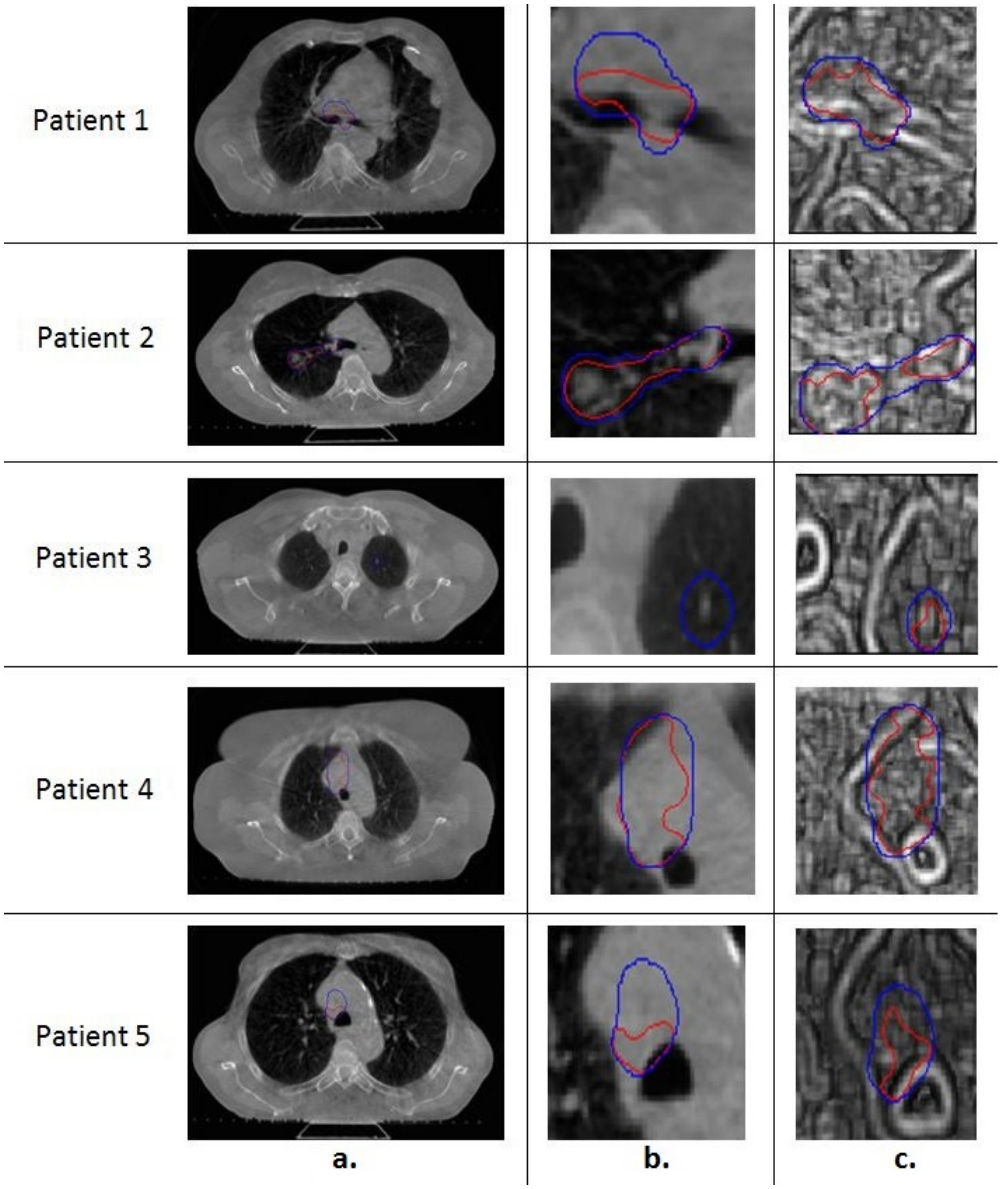

Figure 6.9: Level set comparison on registered CBCT images and their textured images for five patients, a. Level set on registered CBCT image, b. cropped region of interest in each patient of previous part and c. cropped region of interest when level set on textured images is applied (blue contour is GTV and red contour is level set).

6.5 Results and Discussion

As explained in Section 5.4 different level set methods and different texture features were tested in different combinations. The best combination resulted from textures combined by level set when the GTV was the initial contour for level set. As the oncologist chose the three best models, Figure 6.10 shows the performance of these three models on Patient 26.

Figure 6.10: Patient 26: Three best selected segmentations by the oncologist. Blue contour is GTV, yellow is Model m, pink refers to Model e and red is Model g in Section 5.4.

Figure 6.11 shows the results of Model m on the shrinkage of CBCT #10 of Patient 26. Their tumour shrinkage might be more visible in the upper right slice, however the ability of proposed model is shown on the lower right image where nothing is clear. From the upper image, it is obvious that tumour responded well to RT but the lower image is the interesting unknown for clinicians. This model would be a great help when the tumour is hidden between different tissues.

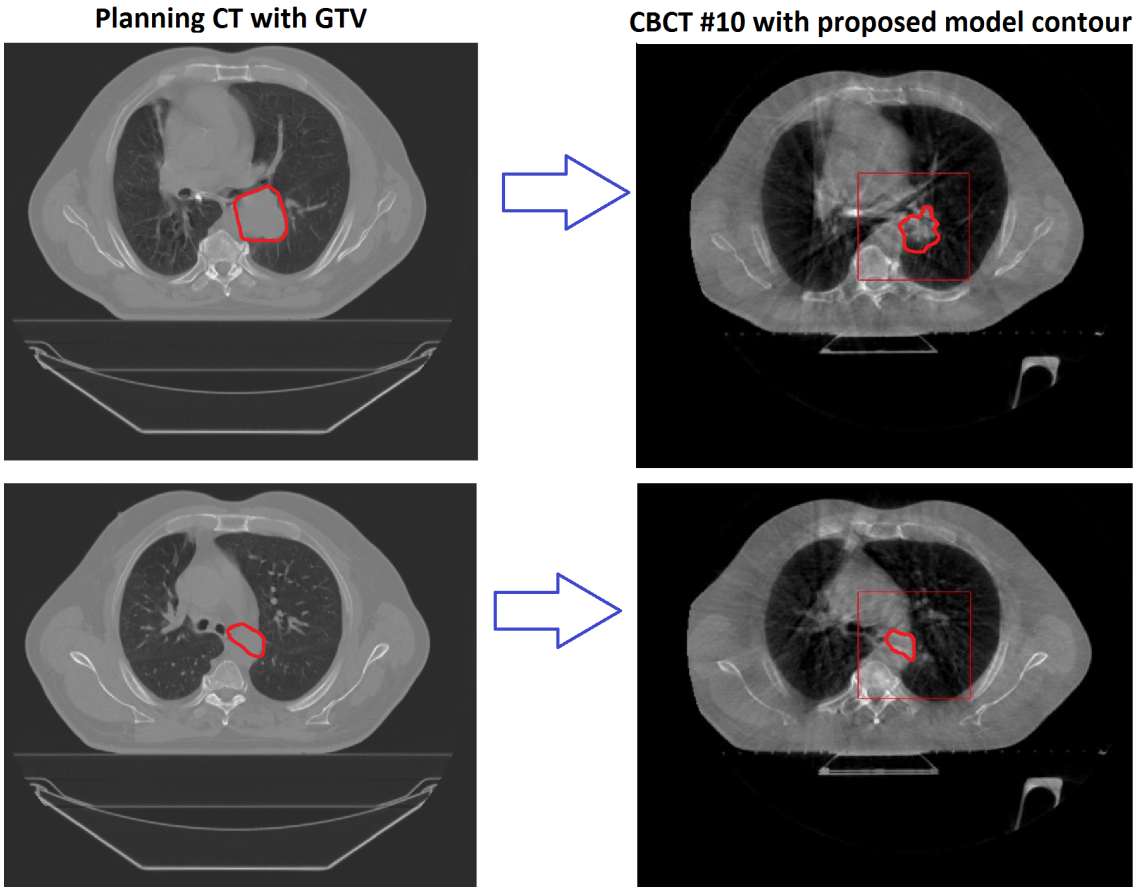

Figure 6.11: Patient 26: Combined sum variance and Li level set method on CBCT #10.

The Figure 6.12 illustrates the Dice coefficient comparison between the three selected contours by the oncologist and GTV on planning-CT for all fifty patients on CBCT #10. Model g has the highest Dice coefficient for all patients which highlights the inability of this method to move far from the initial point. Models m and e have the best performance with generally more than 50% similarity with GTV, as should be expected after almost one third of the RT procedure having been performed. All models are the selected performers by the oncologist. In general, the performance of Model g leads Model g and also Model m by comparing their Dice coefficients. Although all models perform well.

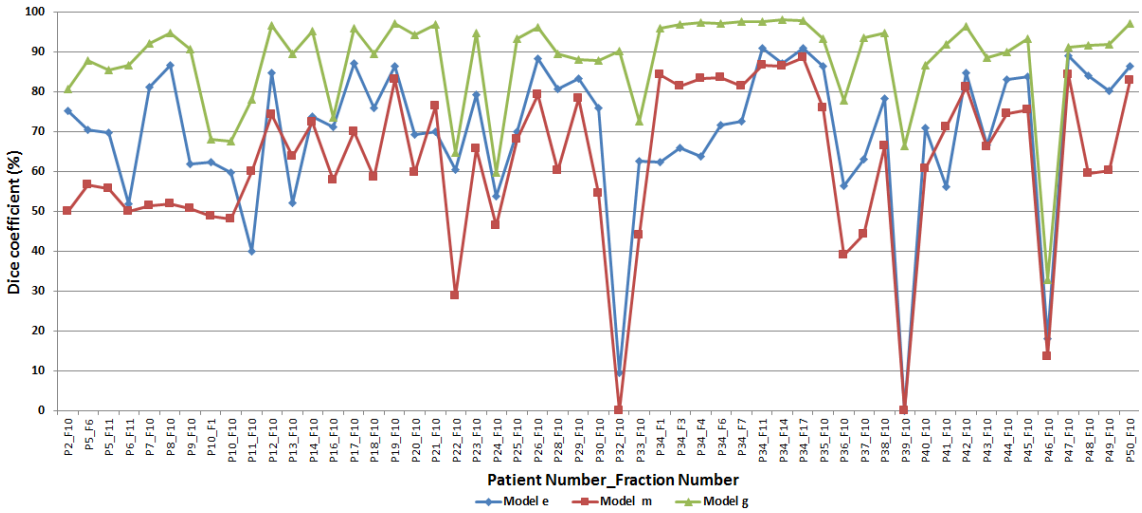

Figure 6.12: The strength of proposed models (e, m and g) on CBCT #10 by comparing the Dice coefficient for all fifty patients compared to the relevant GTV, Model m in blue, Model e in red and Model g in green. All models are the selected performers by the oncologist. In general, the performance of Model g leads Model g and also Model m by comparing their Dice coefficients.

Figure 6.13 shows Dice coefficient measurement between GTV and proposed Model o for one randomly selected slice per patient shown in 6.14 of all fifty patients. This figure illustrates the volume of tumour at the same time.

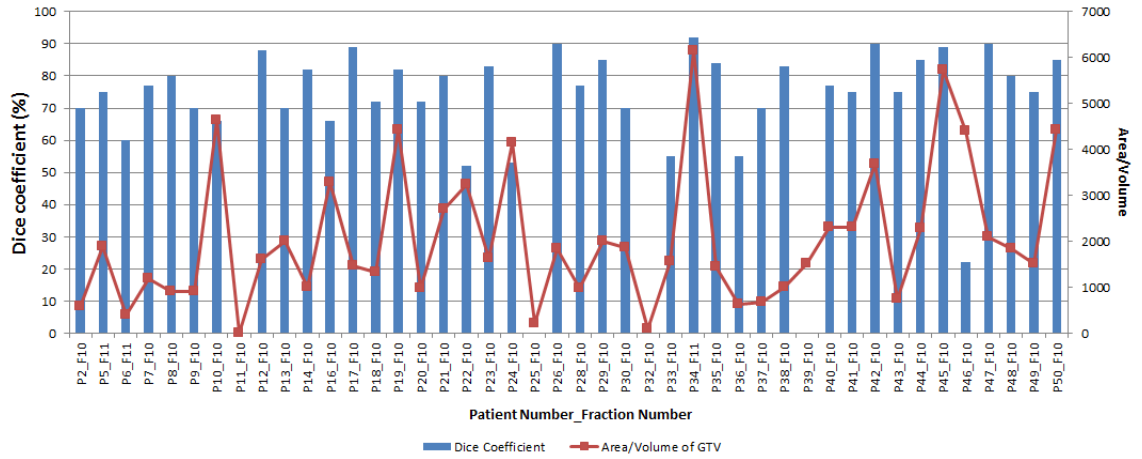

Figure 6.13: The strength of proposed model (Model o) by comparing the Dice coefficient for fifty patients compared to area of the tumour on CBCT #10-11.

The volume and response of a tumour affects the whole RT and image analysis. Smaller tumours and those higher up in the chest cavity are less affected by breathing, therefore from an imaging point of view the images are less distorted by breathing movements. Figure 6.14 illustrates the position and volume of all patients in the dataset from transverse, frontal and sagittal views. The depth for these images inside the body are approximately

in the middle section of human lungs. This image illustrates the exact GTV boundary in upper bust area in all views. Most patients suffered from tumours in the middle or connected between both lungs and are categorized mostly as stage III or IV, shown in Figure 2.4. Figure 6.14 shows that some patients have two or more regions of tumour on the selected CT image such as Patient 16 has two regions on Slice 49 or Patient 24 has two regions on Slice 52 and Patient 27 has no GTV on its data.

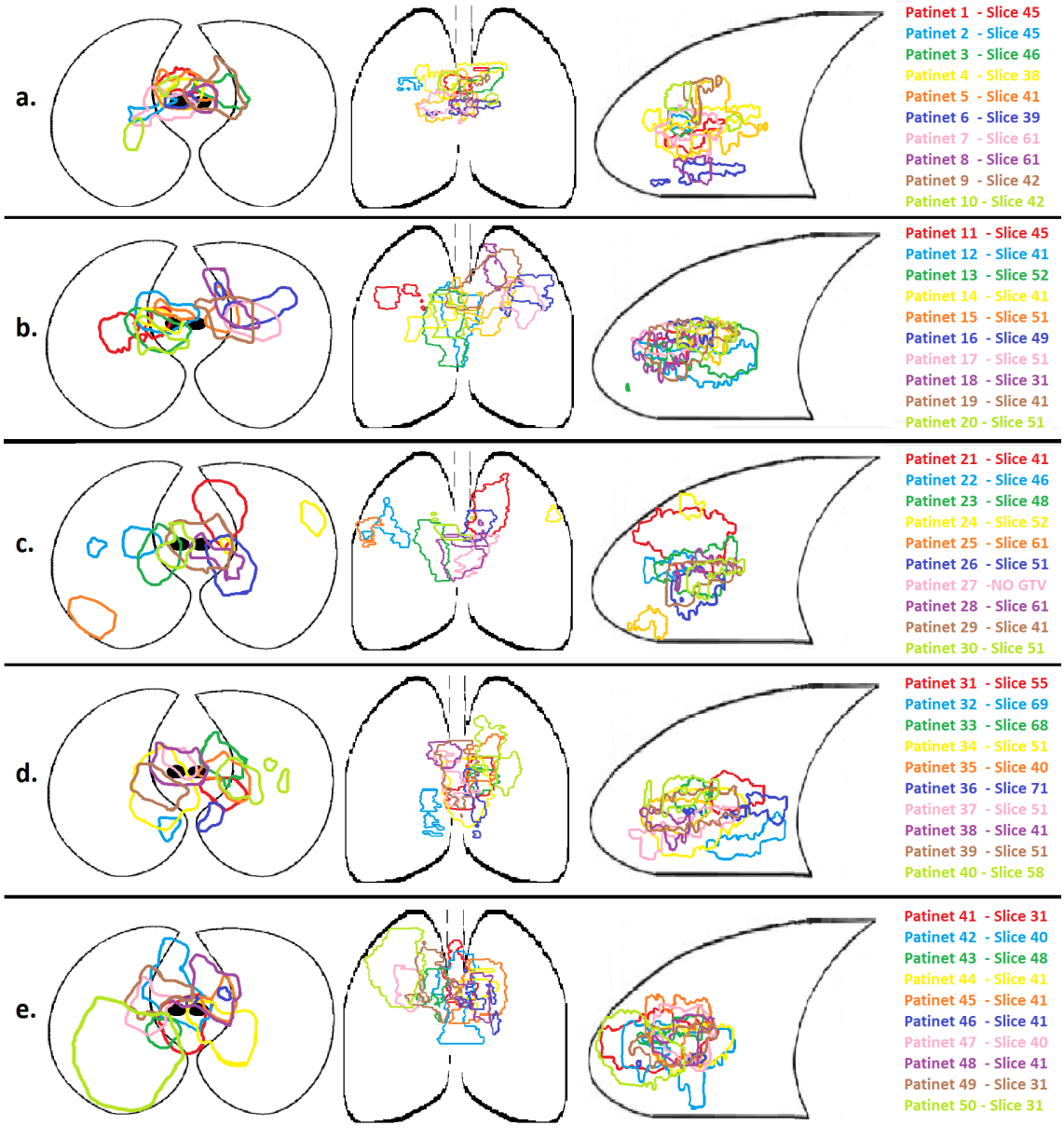

Figure 6.14: Lung tumour GTV distribution for all fifty patients from transverse, frontal and sagittal views on a randomly selected CT slice per patient, a. Patient 1 to Patient 10, b. Patient 11 to Patient 20, c. Patient 21 to Patient 30, d. Patient 31 to Patient 40 and e. Patient 41 to Patient 50.

The volume as well as position of the tumour can affect the accuracy of the proposed model. The quantitative analysis is not very reliable since the tumour is located in the middle area of the lungs. Airways, vessels, oesophagus, the heart and many other organs are compacted inside rib cage. Based on the clinician's experience and situation of the patients, they can contour the GTV to include or exclude different organs which are not thought to be cancerous. The oncologist mentioned that the proposed model can be wrong when Dice coefficient presents strangely since the GTV itself might not be accurate. Although his viewpoint was confidently affirmative when the tumour was just on one lung, when the tumour is distributed in different organs, especially in the middle sections between lungs, the texture analysis would not improve level set's performance as the texture for different organs is different. Therefore the texture changes would mislead the level set.

6.6 Conclusions

In this chapter, the pre-processing algorithms, registration, validation, texture features and segmentations applied on test datasets were discussed. Re-sampling was applied on lung CBCT images. The clinical registration algorithm presented was devised based on clinical RT information embedded in the images by applying the affine transform based on three transformation scales and rotation data from CBCT image domain to its RT domain followed by CBCT RT domain to CT RT domain and finally from CT RT domain to CT image domain.

The proposed combined texture and level set framework demonstrates that by using prior information from pre-treatment images it is possible to automatically segment the GTV on post-RT images with acceptable clinical accuracy. This method was applied to fifty different patients with different types and stages of lung cancer. All of which prove that this model can have a very high accuracy for patients with tumours inside the lungs. However for cases where tumours grow in between organs and include several parts, the segmentation results are not reliable. This can be explained for cases where airways are included inside the GTV because there is no harm of radiating inside GTV as it is hollow but the proposed level set cannot segment airways as a tumour. The oncologist believed that the proposed model is working well when the tumour shape and location is not complicated. The oncologist approved the robustness of combined models and accepted their performance accuracy even for complicated cases, but since the delineated GTV is different it cannot be quantitatively graded.

Chapter 7

Conclusion and Suggestions for Future Work

7.1 Conclusion

There is a need in RT treatment of cancer to identify and segment tumours. The use of semi or fully automatic segmentation approaches can help to increase accuracy and reduce the time spent by doctors defining target radiation volumes. Lung cancer RT has been always a very challenging area in the UK as the image modalities are restricted to planning-CT before treatment and CBCT during the course of treatment. The proposed approach in analysing lung tumours based on CBCT images would help the clinicians to better estimate the location and size of the tumour which is not really visible to the naked eye.

This thesis describes research to develop novel tumour shape analysis models based on texture and level set methods which is capable of improving the off-line ART for lung cancer disease. The improvement of the proposed combined model over level set segmentation alone is illustrated in this research. However, combining texture technique and level set model needs consideration in many factors. First is the matter of choosing the appropriate method from each technique that can combine properly as well as perform satisfactorily on lung CBCT images. Literature reviews in addition to experiments helped in choosing Chan-Vese and Li models for level set and Haralick features as texture techniques. Many combinations in different orders were applied and gave the best combination of sum variance and two-phase Chan-Vese/Li method. The second challenging issue in the proposed model was initialisation as level set can be very dependent to it. This issue was solved by using GTV on CT images and clinical registration to map them on CBCT images. The most and third challenging issue was parameter setting for level set which can influence its success or failure. The absence of ground truth and the poor quality of level set restricts each of the combined models, therefore different combinations of parameters had to be tested on each CBCT slice. A threshold was set to find the Dice coefficient between GTV and the proposed model's level set segmentation on CBCT #1. This recursive parameter tuning was successful in finding the most suitable parameters for

each slice of its relevant CBCT #10. Sum variance and Chan-Vese as well as sum variance and Li methods were both performing well for lung dataset. Although one can perform better than the other for some slices of CBCT for the same fraction of the same patient and can perform weaker than for the remaining slices.

As there is no gold standard for any of these contours, comparing was not yet possible, so the GTV is used for initializing level set but the final segmented result cannot be compared with any fine answer as it is difficult for doctors to delineate the contours of lung tumours on CBCT images. It makes this work more challenging since any of the contours with any parameter may or may not be correct but the final decision was made by the oncologist.

Since the parameter setting was a very challenging issue in this research and in general in most medical imaging in the absence of gold standard. Also, as mentioned earlier, sum variance combined with Chan-Vese and Li methods can perform well but can be further improved. Therefore a new novel level set method was proposed which was taking advantage of the performance of two or more different level set methods in the vector-valued level set shape. This benefited the proposed combined texture and level set model even further as choosing two models with slight different parameters could eliminate the error from the wrong method which could not suit the segmentation image. The proposed model can be combined in multi-phase level set method as well as combination of different other level set methods but the combination of Chan-Vese and Li models in parallel on the sum variance texture image was chosen for the lung data.

The proposed model was applied on non-medical and brain MRI images as well in Chapter 4 also in Chapter 5, Patient 25 is the only case in lung dataset who had GTV on CBCTs. Patient 25 was a great approval for the robustness of the proposed models. The proposed combined sum variance and parallel level sets model demonstrated the 30% shrinkage on the CBCT #10 compared to the GTV on planning-CT as it was expected. This model demonstrated almost 90% of Dice coefficient between each segmentation and its relevant GTV on CBCT#10 as well as CBCT#10.

The outcome of analysis in Chapter 4 and Chapter 5 helped the improvement of the proposed model for all fifty lung cases. Chapter 6 showed the results and introduced this model as an assistant to the medical team during the course of lung cancer RT. Chapter 6 provided the results of Dice coefficient between proposed models and GTV on planning-CT data. Also the area of GTV was compared against the proposed parallel level sets to show the expected changes compared to the area overlap. These models can be very helpful to the expert oncologists and can be used in offline ART for this data and also for other similar medical imaging RT applications.

The oncologist approved the ability of the proposed models. For some cases where the shape of tumour was complicated and grew in different organs, the oncologist still commented that the proposed model can be correct but there is no possible way of seeing the real tumour.

7.2 Suggestions for Future Work

Future work will focus on considering different texture parameters in different depths of the body as the texture of the same patient would vary slightly during image acquisition at these different depth. Also using the new generation of CBCT images which are more accurate in quality in 4D can help better analysis of lung tumours for RT purposes.

Another worthwhile approach might be combining level set with Markov random fields to form a dedicated platform. This approach would be widely applicable and could be developed on a range of clinical data especially lung cancer.

One drawback of this work is the lack of data, as there is no gold standard. In most medical image contouring, clinicians are not 100% confident with the boundary they delineated. Two different oncologists might have different opinions with regards to the details of the tumour shape even on good quality images like MRI or CT. Therefore, applying this model on other datasets would be a great help for oncologists and provide better evaluation for the model.

Another suggestion is considering 3D texture analysis on the same data. The changes over the volume can give 3D texture analysis as well as more freedom to level set to evolve in 3D.

Detecting any similarity of changes for a cancerous region of different tissues would be the best method of analysis. Doctors spend time in changing intensity enhancement slice by slice to detect the tumours, also based on experience and the knowledge they gain through treating patients. A future work would be developing deep learning algorithms to detect the shapes, easier direction of growth for the tumour as well as intensity change speed based on the tissue type and neighbourhood regions which helps in finding the relativity of cancerous cells with each other.

Appendix A

Description of Lung Dataset

A.1 Image Details of Lung Dataset

The main dataset used in this thesis is shown in Table A.1 which includes the CT and CBCT images details for all fifty patients. The table shows the main characteristic of each image sequence which are used for the pre-processing and registration purposes such as pixel and voxel sizes.

Case	Modality	Slice No	Date	Pixel Size	Slice Thickness
Patient 1	CT	107	30-01-2010	512 ×512	3mm
	CBCT #10	53	30-04-2010	384 ×384	3mm
Patient 2	CT	123	06-04-2010	512 ×512	3mm
	CBCT #10	53	05-05-2010	384 ×384	3mm
Patient 3	CT	124	27-04-2010	512 ×512	3mm
	CBCT #1	53	10-05-2010	384 ×384	3mm
	CBCT #10	53	21-05-2010	384 ×384	3mm
Patient 4	CT	111	18-05-2010	512 ×512	3mm
	CBCT #1	53	08-06-2010	384 ×384	3mm
	CBCT #10	53	22-06-2010	384 ×384	3mm
Patient 5	CT	111	08-06-2010	512 ×512	3mm
	CBCT #1	53	21-06-2010	384 ×384	3mm
	CBCT #6	53	28-06-2010	384 ×384	3mm
	CBCT #11	53	07-08-2010	384 ×384	3mm
Patient 6	CT	110	13-09-2011	512 ×512	3mm
	CBCT #1	53	26-09-2011	384 ×384	1mm
	CBCT #11	53	10-10-2011	384 ×384	1mm
Patient 7	CT	144	21-09-2010	512 ×512	3mm
	CBCT #1	53	08-10-2010	384 ×384	3mm
	CBCT #10	53	15-10-2010	384 ×384	3mm
Patient 8	CT	116	16-11-2010	512 ×512	3mm
	CBCT #1	53	30-11-2010	384 ×384	1mm

	CBCT #10	53	10-12-2010	384 ×384	1mm
Patient 9	CT	121	25-01-2011	512 ×512	3mm
	CBCT #1	53	14-02-2011	384 ×384	1mm
	CBCT #10	53	28-02-2011	384 ×384	1mm
Patient 10	CT	111	18-01-2011	512 ×512	3mm
	CBCT #1	53	07-02-2011	384 ×384	1mm
	CBCT #10	53	21-02-2011	384 ×384	1mm
Patient 11	CT	118	21-06-2011	512 ×512	3mm
	CBCT #1	53	05-07-2011	384 ×384	1mm
	CBCT #10	53	18-07-2011	384 ×384	1mm
Patient 12	CT	102	16-07-2010	512 ×512	3mm
	CBCT #1	53	19-07-2010	384 ×384	3mm
	CBCT #10	53	30-07-2010	384 ×384	3mm
Patient 13	CT	120	29-06-2011	512 ×512	3mm
	CBCT #1	53	03-08-2011	384 ×384	1mm
	CBCT #10	53	16-08-2011	384 ×384	1mm
Patient 14	CT	97	27-07-2010	512 ×512	3mm
	CBCT #1	53	10-08-2010	384 ×384	3mm
	CBCT #10	53	23-08-2010	384 ×384	3mm
Patient 15	CT	100	10-09-2010	512 ×512	3mm
	CBCT #1	53	27-09-2010	384 ×384	3mm
Patient 16	CT	117	05-01-2011	512 ×512	3mm
	CBCT #1	53	19-01-2011	384 ×384	1mm
	CBCT #10	53	01-02-2011	384 ×384	1mm
Patient 17	CT	117	22-06-2010	512 ×512	3mm
	CBCT #1	53	05-07-2010	384 ×384	3mm
	CBCT #10	53	16-07-2010	384 ×384	3mm
Patient 18	CT	121	26-10-2010	512 ×512	3mm
	CBCT #1	53	08-11-2010	384 ×384	1mm
	CBCT #10	53	22-11-2010	384 ×384	1mm
Patient 19	CT	131	17-08-2010	512 ×512	3mm
	CBCT #1	53	31-08-2010	384 ×384	3mm
	CBCT #10	53	13-09-2010	384 ×384	3mm
Patient 20	CT	100	20-07-2010	512 ×512	3mm
	CBCT #1	53	02-08-2010	384 ×384	3mm
	CBCT #10	53	13-08-2010	384 ×384	3mm
Patient 21	CT	112	24-05-2011	512 ×512	3mm
	CBCT #1	53	06-06-2011	384 ×384	1mm

	CBCT #10	53	17-06-2011	384 ×384	1mm
Patient 22	CT	109	07-09-2011	512 ×512	3mm
	CBCT #1	53	20-09-2011	384 ×384	1mm
	CBCT #10	53	05-10-2011	384 ×384	1mm
Patient 23	CT	106	04-10-2011	512 ×512	3mm
	CBCT #1	53	17-10-2011	384 ×384	1mm
	CBCT #10	53	28-10-2011	384 ×384	1mm
Patient 24	CT	124	06-09-2011	512 ×512	3mm
	CBCT #1	53	20-09-2011	384 ×384	1mm
	CBCT #10	53	04-10-2011	384 ×384	1mm
Patient 25	CT	130	10-05-2011	512 ×512	3mm
	CBCT #1	64	23-05-2011	384 ×384	1mm
	CBCT #10	54	10-06-2011	384 ×384	1mm
Patient 26	CT	126	05-10-2010	512 ×512	3mm
	CBCT #1	52	18-10-2010	384 ×384	3mm
	CBCT #10	54	01-11-2010	384 ×384	1mm
Patient 27	CT	127	06-09-2011	512 ×512	3mm
	CBCT #1	53	19-09-2011	384 ×384	1mm
	CBCT #10	53	30-09-2011	384 ×384	1mm
Patient 28	CT	121	10-12-2010	512 ×512	3mm
	CBCT #1	53	20-12-2010	384 ×384	1mm
	CBCT #10	53	06-01-2011	384 ×384	1mm
Patient 29	CT	104	26-04-2011	512 ×512	3mm
	CBCT #1	53	13-05-2011	384 ×384	1mm
	CBCT #10	53	26-05-2011	384 ×384	1mm
Patient 30	CT	121	07-06-2011	512 ×512	3mm
	CBCT #1	53	20-06-2011	384 ×384	1mm
	CBCT #10	53	01-07-2011	384 ×384	1mm
Patient 31	CT	95	15-06-2010	512 ×512	3mm
	CBCT #1	53	28-06-2010	384 ×384	3mm
	CBCT #10	53	12-07-2010	384 ×384	3mm
Patient 32	CT	117	27-09-2011	512 ×512	3mm
	CBCT #1	53	10-10-2011	384 ×384	1mm
	CBCT #10	53	21-10-2011	384 ×384	1mm
Patient 33	CT	137	01-02-2011	512 ×512	3mm
	CBCT #1	53	14-02-2011	384 ×384	1mm
	CBCT #10	53	25-02-2011	384 ×384	1mm
Patient 34	CT	137	28-06-2011	512 ×512	3mm
	CBCT #1	53	12-07-2011	384 ×384	1mm

	CBCT #3	53	14-07-2011	384 ×384	1mm
	CBCT #4	53	15-07-2011	384 ×384	1mm
	CBCT #6	53	19-07-2011	384 ×384	1mm
	CBCT #7	53	20-07-2011	384 ×384	1mm
	CT	127	14-07-2011	512 ×512	3mm
	CBCT #11	53	26-07-2011	384 ×384	1mm
	CBCT #14	53	29-07-2011	384 ×384	1mm
	CBCT #17	53	03-08-2011	384 ×384	1mm
Patient 35	CT	115	19-07-2011	512 ×512	3mm
	CBCT #1	53	01-08-2011	384 ×384	1mm
	CBCT #10	53	10-08-2011	384 ×384	1mm
Patient 36	CT	113	23-08-2011	512 ×512	3mm
	CBCT #1	53	05-09-2011	384 ×384	1mm
	CBCT #10	53	09-09-2011	384 ×384	1mm
Patient 37	CT	111	24-05-2011	512 ×512	3mm
	CBCT #1	53	06-06-2011	384 ×384	1mm
	CBCT #10	53	21-06-2011	384 ×384	1mm
Patient 38	CT	110	16-08-2011	512 ×512	3mm
	CBCT #1	53	29-08-2011	384 ×384	1mm
	CBCT #10	53	09-09-2011	384 ×384	1mm
Patient 39	CT	115	14-09-2011	512 ×512	3mm
	CBCT #1	53	26-09-2011	384 ×384	1mm
	CBCT #10	53	07-10-2011	384 ×384	1mm
Patient 40	CT	130	04-05-2011	512 ×512	3mm
	CBCT #1	53	23-05-2011	384 ×384	1mm
	CBCT #10	53	03-06-2011	384 ×384	1mm
Patient 41	CT	112	03-08-2011	512 ×512	3mm
	CBCT #1	53	16-08-2011	384 ×384	3mm
	CBCT #10	53	30-08-2011	384 ×384	3mm
Patient 42	CT	93	03-08-2010	512 ×512	3mm
	CBCT #1	53	16-08-2010	384 ×384	3mm
	CBCT #10	53	30-08-2011	384 ×384	3mm
Patient 43	CT	118	20-09-2011	512 ×512	3mm
	CBCT #1	53	03-10-2011	384 ×384	1mm
	CBCT #10	53	14-10-2011	384 ×384	1mm
Patient 44	CT	108	17-05-2011	512 ×512	3mm
	CBCT #1	53	02-06-2011	384 ×384	1mm
	CBCT #10	53	16-06-2011	384 ×384	1mm
Patient 45	CT	120	02-08-2011	512 ×512	3mm

	CBCT #1	53	15-08-2011	384 ×384	1mm
	CBCT #10	53	26-08-2011	384 ×384	1mm
Patient 46	CT	108	20-07-2010	512 ×512	3mm
	CBCT #1	53	02-08-2010	384 ×384	3mm
	CBCT #10	53	13-08-2010	384 ×384	3mm
Patient 47	CT	119	21-06-2011	512 ×512	3mm
	CBCT #1	53	06-07-2011	384 ×384	1mm
	CBCT #10	53	20-07-2011	384 ×384	1mm
Patient 48	CT	99	03-08-2010	512 ×512	3mm
	CBCT #10	53	30-08-2010	384 ×384	3mm
Patient 49	CT	106	27-07-2010	512 ×512	3mm
	CBCT #10	53	23-08-2010	384 ×384	3mm
Patient 50	CT	105	11-09-2010	512 ×512	3mm
	CBCT #1	53	20-09-2011	384 ×384	3mm
	CBCT #10	53	04-10-2011	384 ×384	3mm

Table A.1: Image details of lung dataset used to test the novel proposed combined texture and level set framework including fifty patients.

A.2 GTV on CT Images for All Fifty Patients

Figures A.1, A.2 and A.3 illustrate the montage form of planning-CT images for patients 25, 26 and 34 respectively. In each figure, all of the slices acquired during CT scan is shown as well as the GTV delineated for the slices containing the tumour.

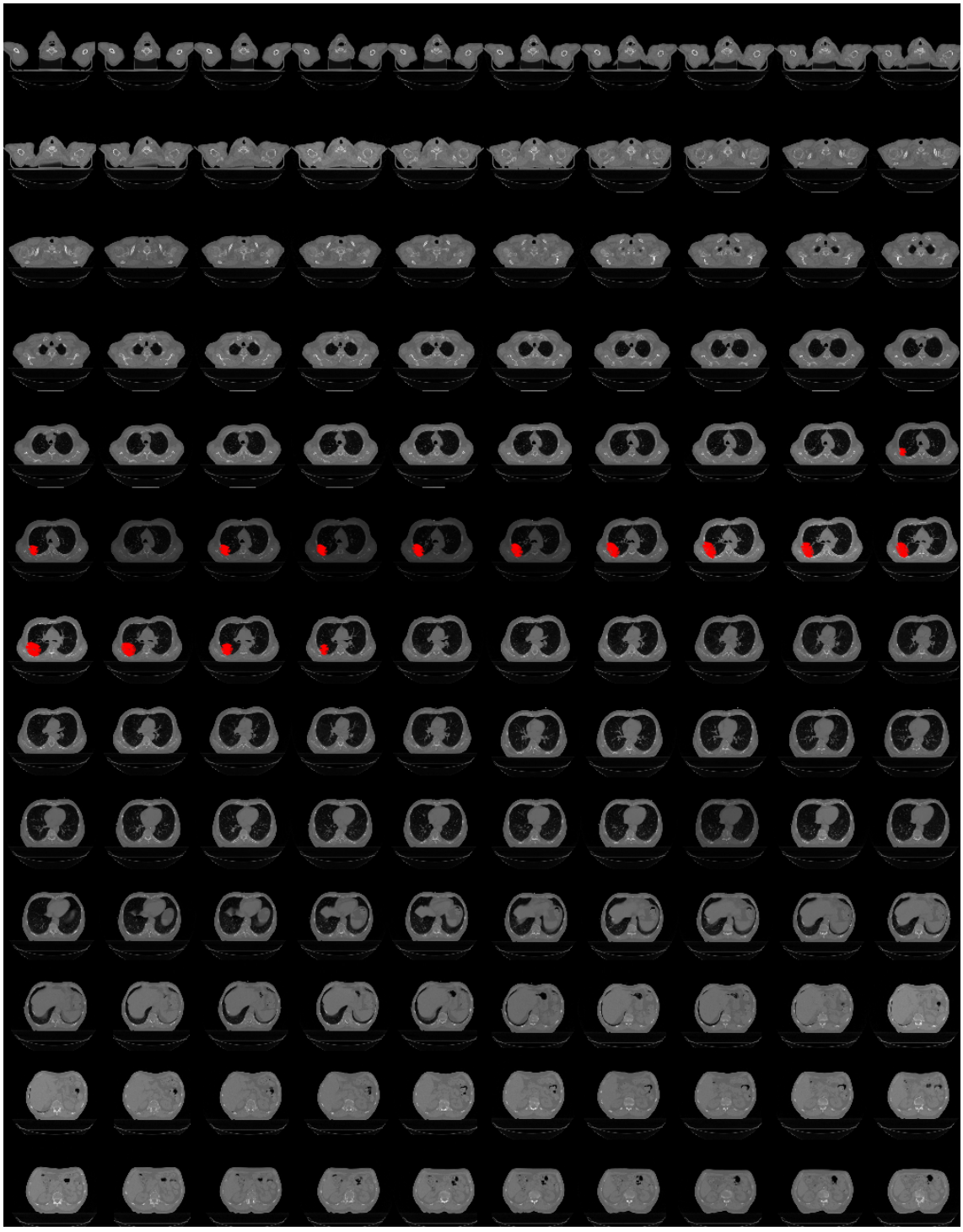

Figure A.1: Montage illustration of planning-CT images for Patient 25 including GTV (by the oncologist) in red on slices which contain the tumour.

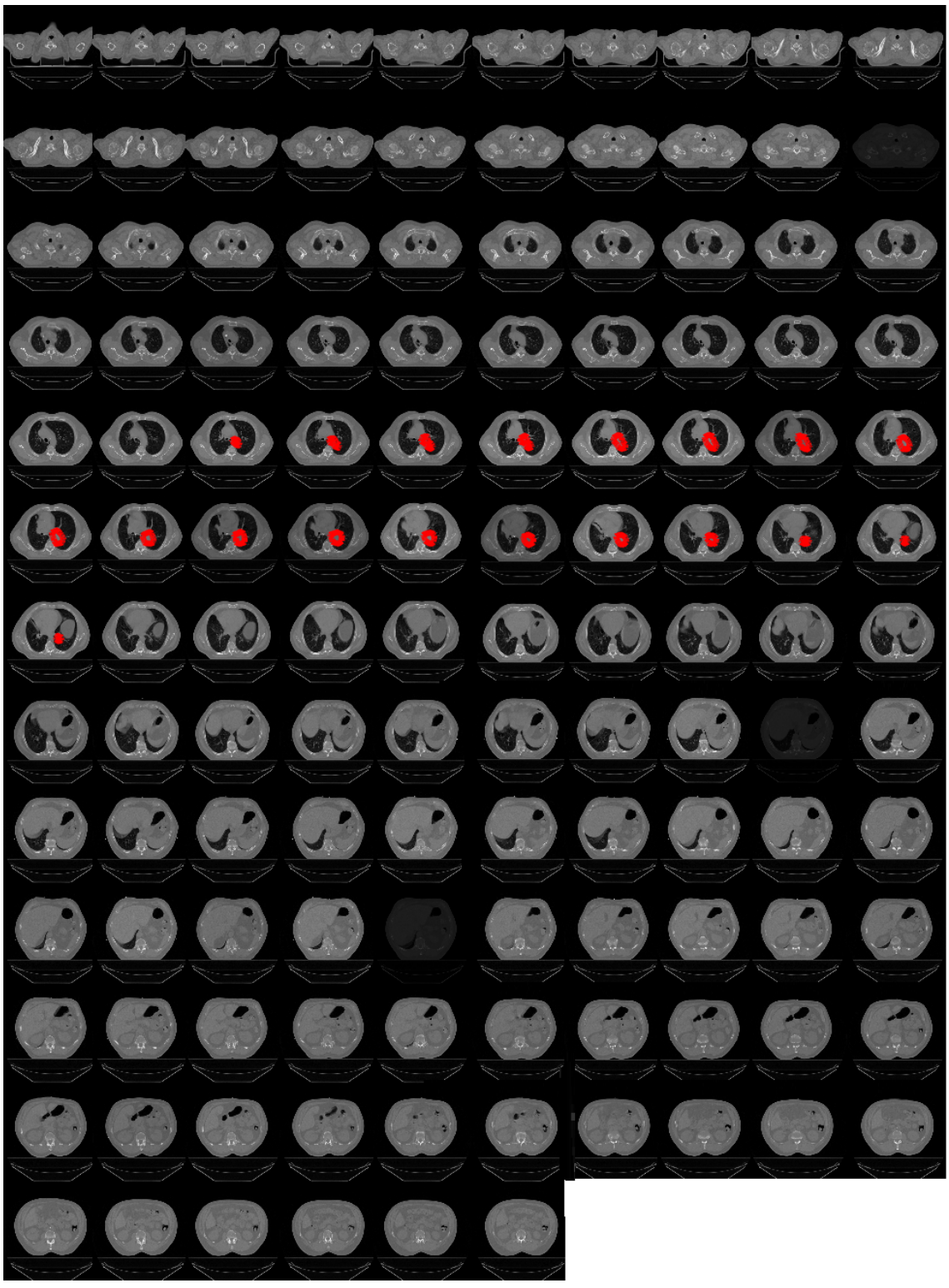

Figure A.2: Montage illustration of planning-CT images for Patient 26 including GTV (by the oncologist) in red on slices which contain the tumour.

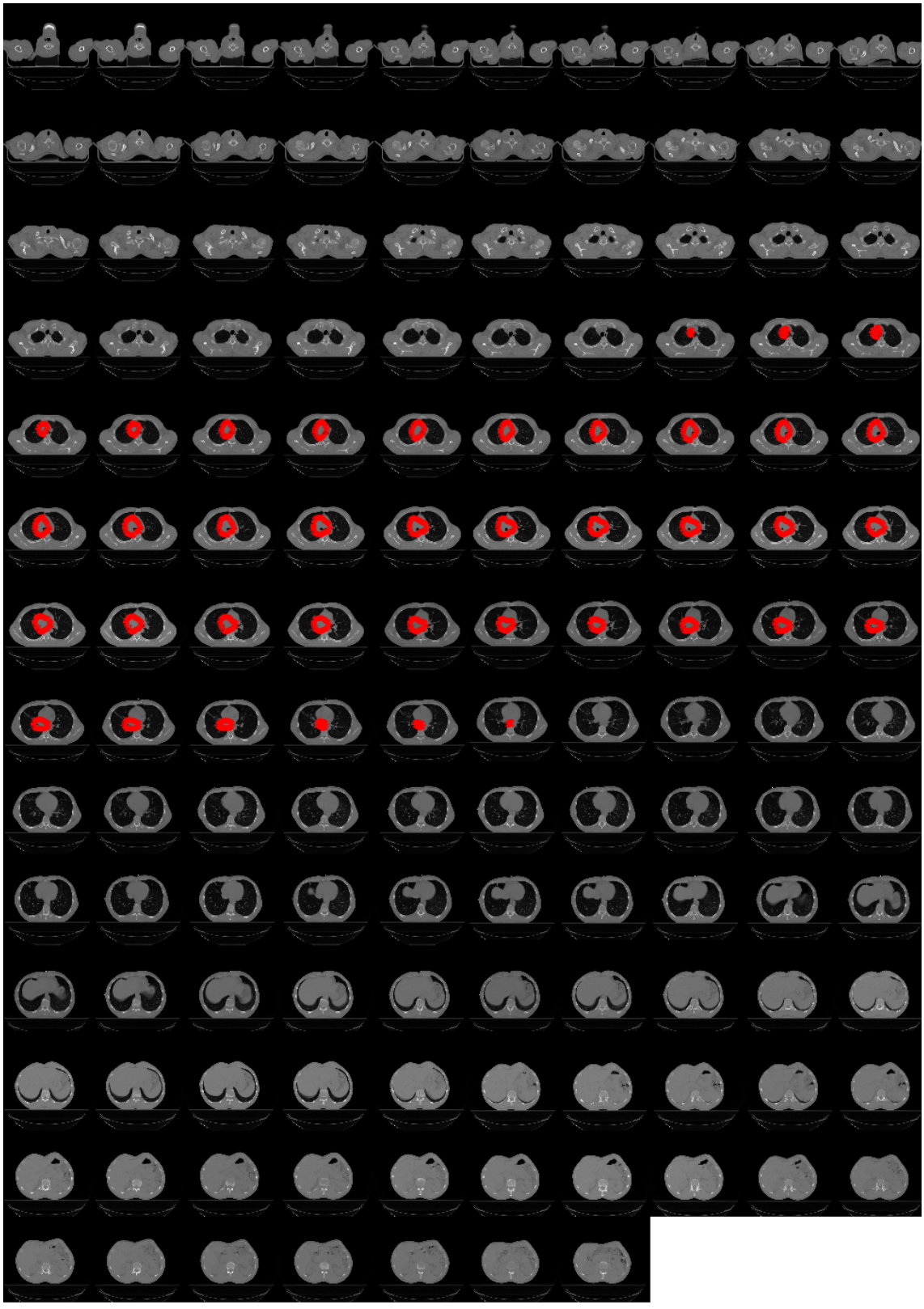

Figure A.3: Montage illustration of planning-CT images for Patient 34 including GTV (by the oncologist) in red on slices which contain the tumour.

Appendix B

Results of Different Parameter Sets for Level Set

The figures in this Appendix show different parameter settings for level set methods on different patients and their different CBCT images. Figure B.1 to Figure B.5 illustrate Patient 2 for all of its slices containing the tumour. Figure B.6 to Figure B.8 show Patient 3 for slices 23 to 25. Figure B.9 to Figure B.11 demonstrates different parameters combinations for Patient 4 slices 14 to 16. Finally, Patient 5 is shown in Figure B.12 for Slice 23 until Figure B.14 for Slice 25.

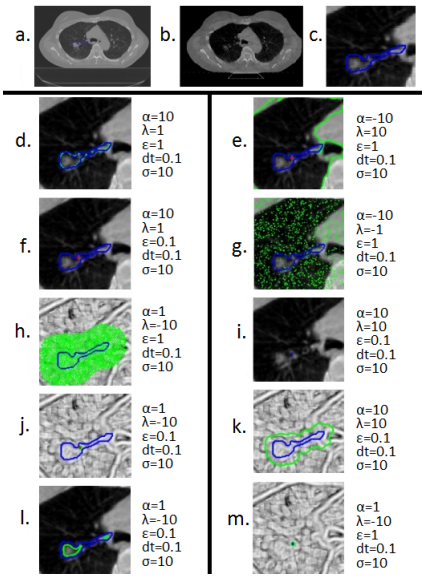

Figure B.1: Performance of different combinations with different parameters for lung CBCT image tumour segmentation, Patient 2-Slice 40: a. planning-CT, b. CBCT #1, c. cropped part of of part c with clinical GTV, d. Li model on CBCT using GTV as its initial contour, e. Chan-Vese model on CBCT using centre of GTV as its initial contour, f. Li model on CBCT using centre of GTV as its initial contour, g. Chan-Vese model on texture image using GTV as its initial contour, h. Li model on PCA image using GTV as its initial contour, i. Chan-Vese model on vector-valued texture image using centre of GTV as its initial contour, j. Li model on PCA image using centre of GTV as its initial contour, k. Chan-Vese model on PCA image using GTV as its initial contour, l. Chan-Vese on CBCT using GTV as its initial contour and m. Chan-Vese model on PCA image using centre of GTV as its initial contour.

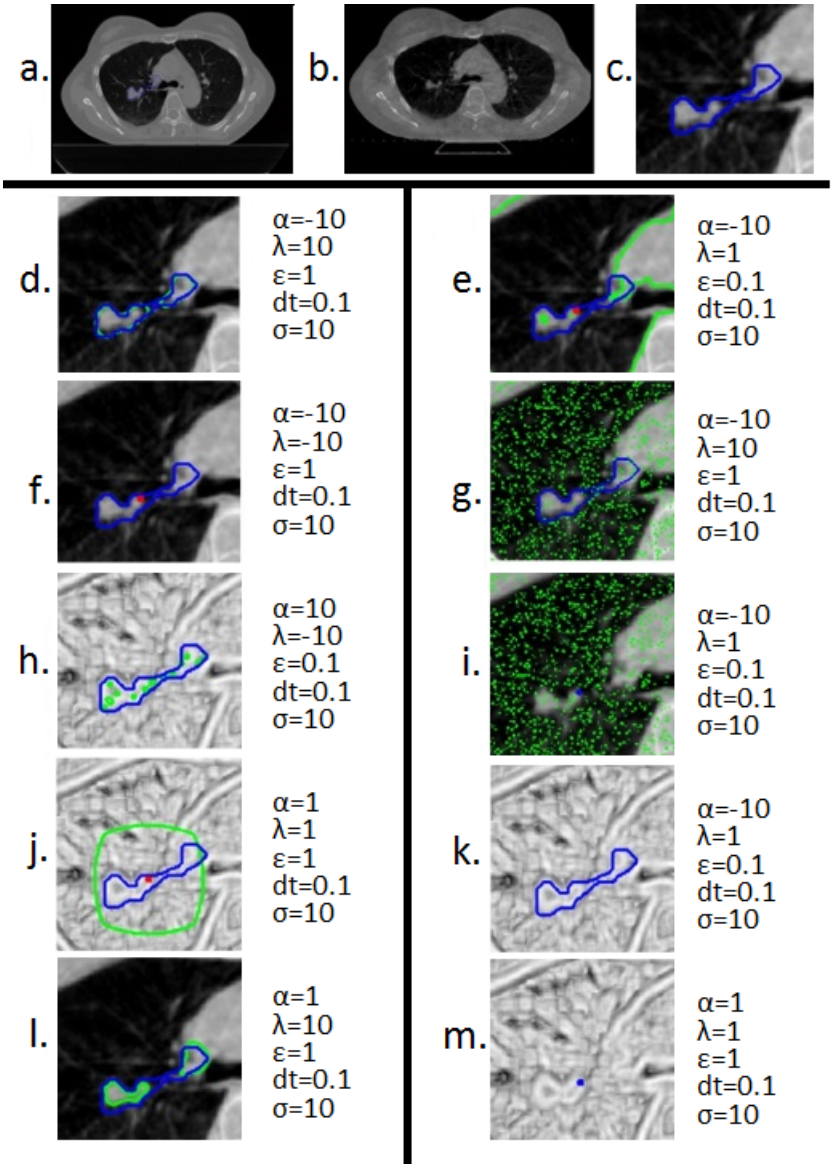

Figure B.2: Performance of different combinations with different parameters for lung CBCT image tumour segmentation, Patient 2-Slice 42: a. planning-CT, b. CBCT #1, c. cropped part of of part c with clinical GTV, d. Li model on CBCT using GTV as its initial contour, e. Chan-Vese model on CBCT using centre of GTV as its initial contour, f. Li model on CBCT using centre of GTV as its initial contour, g. Chan-Vese model on texture image using GTV as its initial contour, h. Li model on PCA image using GTV as its initial contour, i. Chan-Vese model on vector-valued texture image using centre of GTV as its initial contour, j. Li model on PCA image using centre of GTV as its initial contour, k. Chan-Vese model on PCA image using GTV as its initial contour, l. Chan-Vese on CBCT using GTV as its initial contour and m. Chan-Vese model on PCA image using centre of GTV as its initial contour.

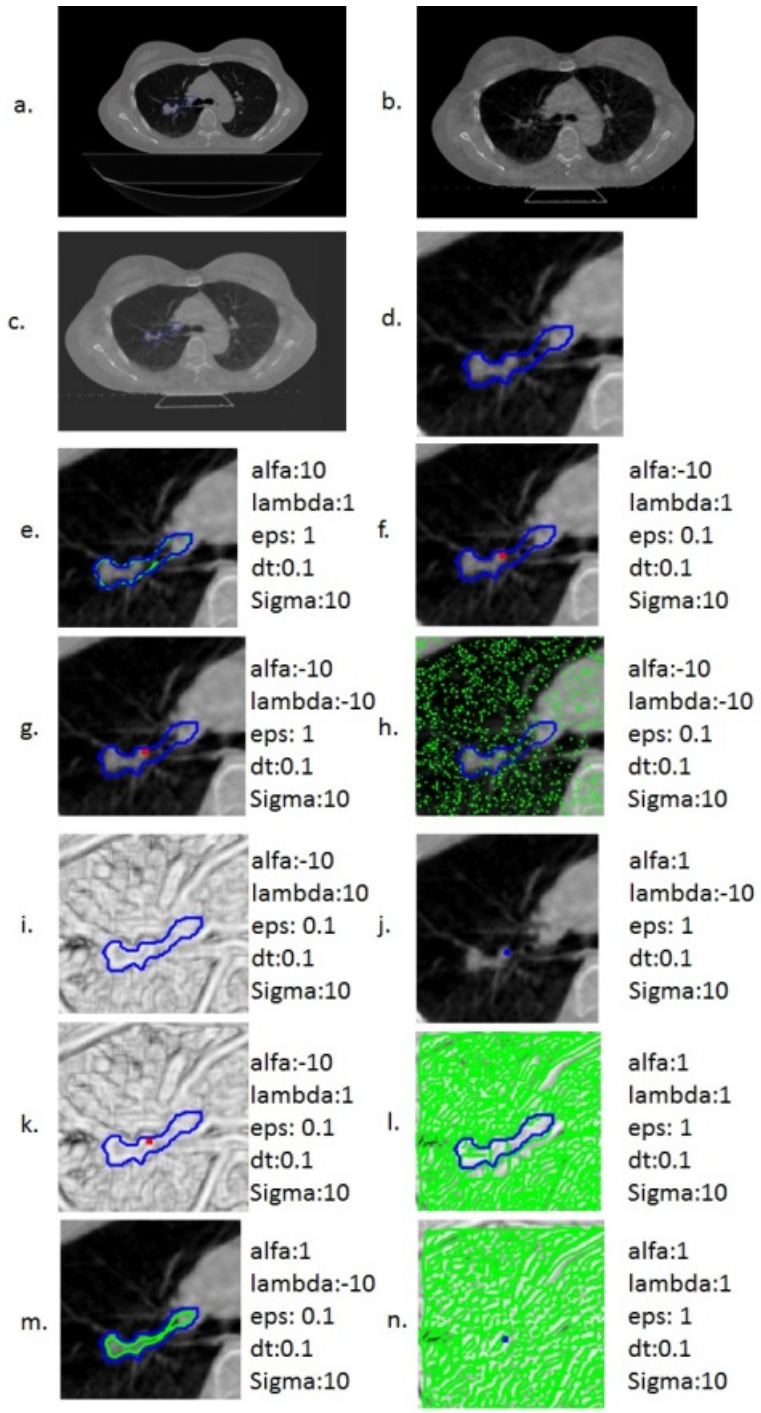

Figure B.3: Performance of different combinations with different parameters for lung CBCT image tumour segmentation, Patient 2-Slice 43: a. planning-CT, b. CBCT #1, c. registered CBCT, d. cropped part of of part c with clinical GTV, e. Li model on CBCT using GTV as its initial contour, f. Chan-Vese model on CBCT using centre of GTV as its initial contour, g. Li model on CBCT using centre of GTV as its initial contour, h. Chan-Vese model on texture image using GTV as its initial contour, i. Li model on PCA image using GTV as its initial contour, j. Chan-Vese model on vector-valued texture image using centre of GTV as its initial contour, k. Li model on PCA image using centre of GTV as its initial contour, l. Chan-Vese model on PCA image using GTV as its initial contour, m. Chan-Vese on CBCT using GTV as its initial contour and n. Chan-Vese model on PCA image using centre of GTV as its initial contour

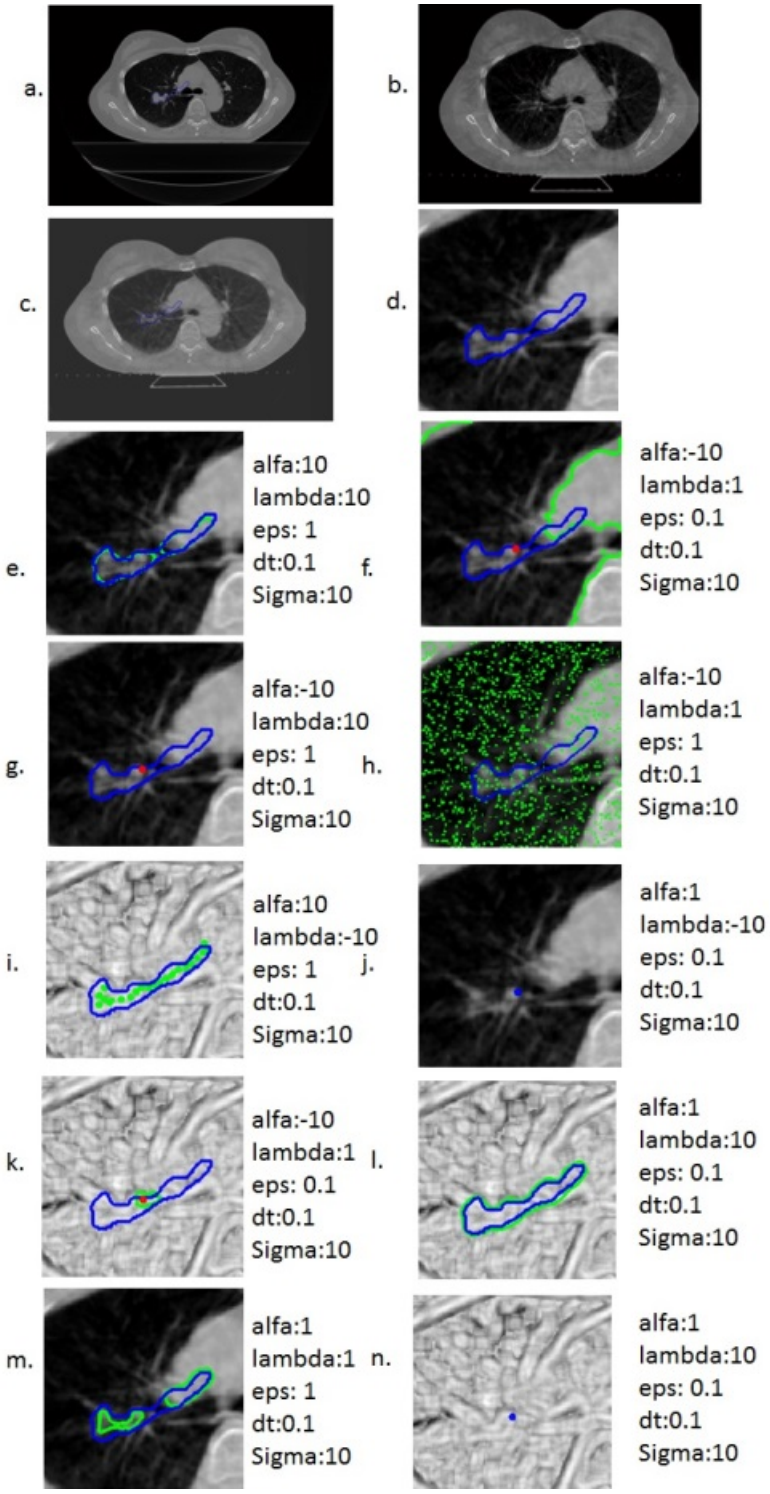

Figure B.4: Performance of different combinations with different parameters for lung CBCT image tumour segmentation, Patient 2-Slice 44: a. Planning-CT, b. CBCT #1, c. Registered CBCT, d. Cropped part of of part c with clinical GTV, e. Li model on CBCT using GTV as its initial contour, f. Chan-Vese model on CBCT using centre of GTV as its initial contour, g. Li model on CBCT using centre of GTV as its initial contour, h. Chan-Vese model on texture image using GTV as its initial contour, i. Li model on PCA image using GTV as its initial contour, j. Chan-Vese model on vector-valued texture image using centre of GTV as its initial contour, k. Li model on PCA image using centre of GTV as its initial contour, l. Chan-Vese model on PCA image using GTV as its initial contour, m. Chan-Vese on CBCT using GTV as its initial contour and n. Chan-Vese model on PCA image using centre of GTV as its initial contour

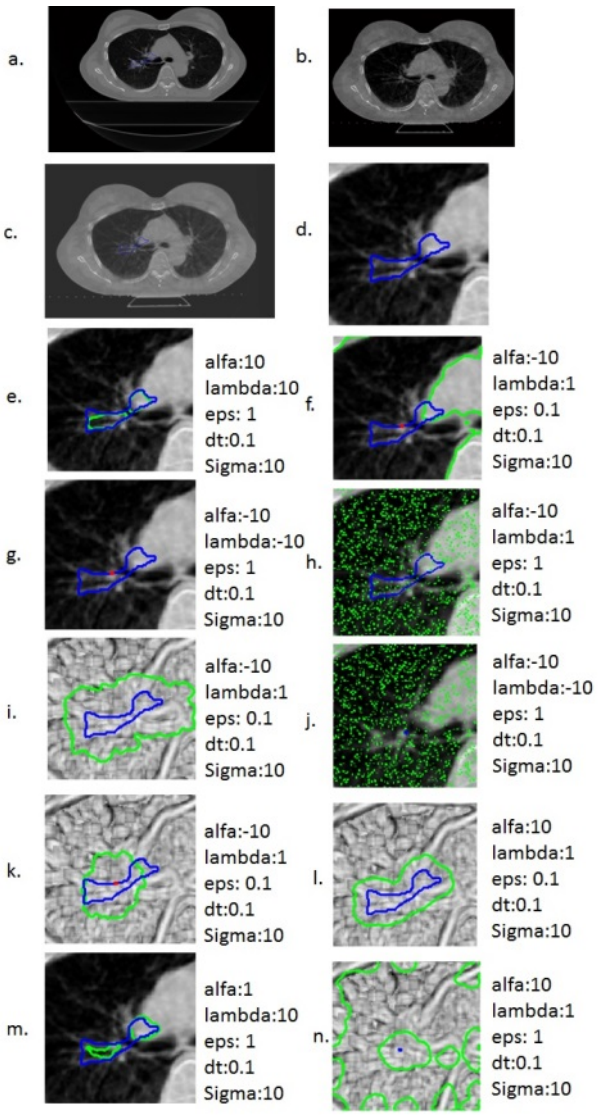

Figure B.5: Performance of different combinations with different parameters for lung CBCT image tumour segmentation, Patient 2-Slice 45: a. Planning-CT, b. CBCT #1, c. Registered CBCT, d. Cropped part of of part c with clinical GTV, e. Li model on CBCT using GTV as its initial contour, f. Chan-Vese model on CBCT using centre of GTV as its initial contour, g. Li model on CBCT using centre of GTV as its initial contour, h. Chan-Vese model on texture image using GTV as its initial contour, i. Li model on PCA image using GTV as its initial contour, j. Chan-Vese model on vector-valued texture image using centre of GTV as its initial contour, k. Li model on PCA image using centre of GTV as its initial contour, l. Chan-Vese model on PCA image using GTV as its initial contour, m. Chan-Vese on CBCT using GTV as its initial contour and n. Chan-Vese model on PCA image using centre of GTV as its initial contour

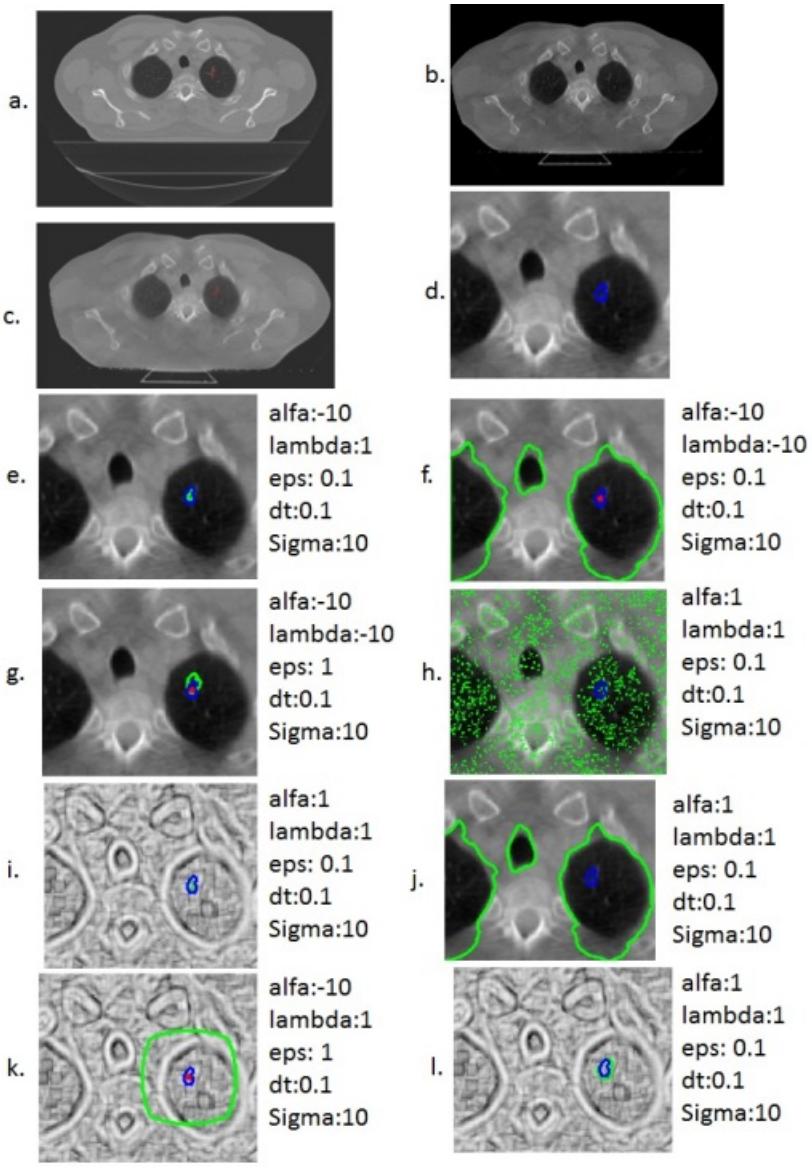

Figure B.6: Performance of different combinations with different parameters for lung CBCT image tumour segmentation, Patient 3-Slice 23: a. planning-CT, b. CBCT #1, c. registered CBCT, d. cropped part of of part c with clinical GTV, e. Li model on CBCT using GTV as its initial contour, f. Chan-Vese model on CBCT using centre of GTV as its initial contour, g. Li model on CBCT using centre of GTV as its initial contour, h. Chan-Vese model on texture image using GTV as its initial contour, i. Li model on PCA image using GTV as its initial contour, j. Chan-Vese model on vector-valued texture image using centre of GTV as its initial contour, k. Li model on PCA image using centre of GTV as its initial contour, l. Chan-Vese model on PCA image using GTV as its initial contour, m. Chan-Vese on CBCT using GTV as its initial contour and n. Chan-Vese model on PCA image using centre of GTV as its initial contour

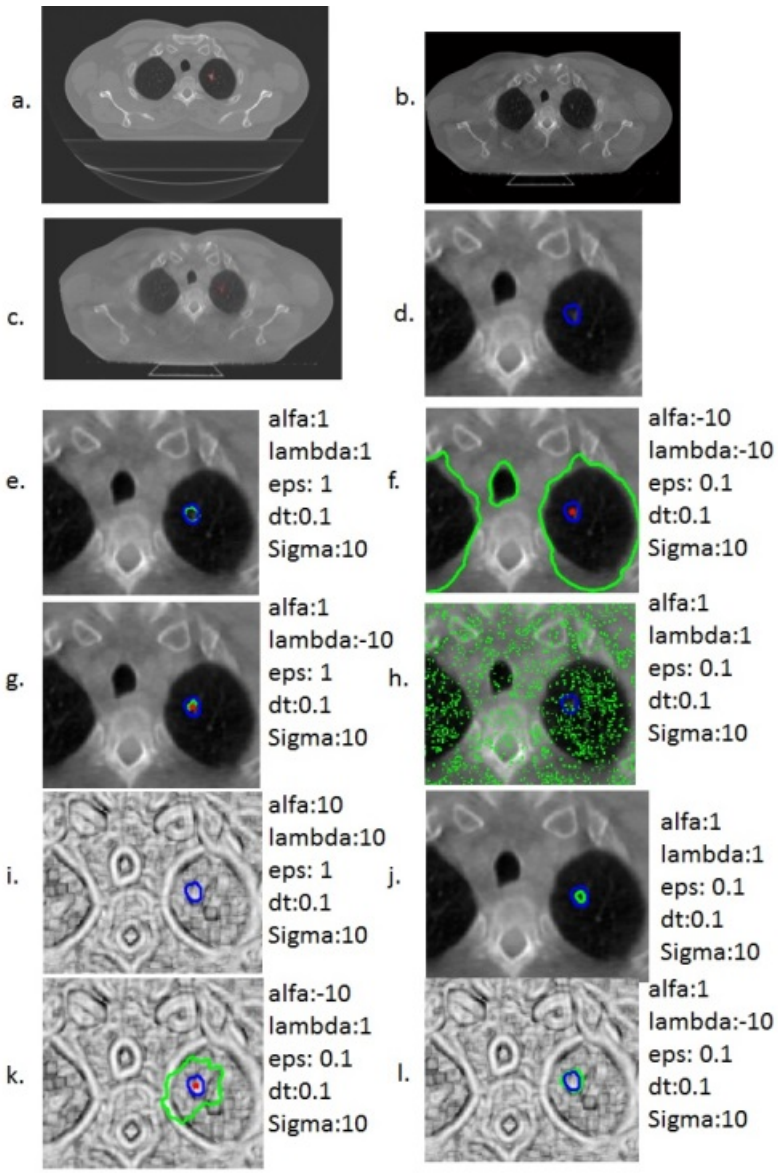

Figure B.7: Performance of different combinations with different parameters for lung CBCT image tumour segmentation, Patient 3-Slice 24: a. Planning-CT, b. CBCT #1, c. Registered CBCT, d. Cropped part of of part c with clinical GTV, e. Li model on CBCT using GTV as its initial contour, f. Chan-Vese model on CBCT using centre of GTV as its initial contour, g. Li model on CBCT using centre of GTV as its initial contour, h. Chan-Vese model on texture image using GTV as its initial contour, i. Li model on PCA image using GTV as its initial contour, j. Chan-Vese model on vector-valued texture image using centre of GTV as its initial contour, k. Li model on PCA image using centre of GTV as its initial contour, l. Chan-Vese model on PCA image using GTV as its initial contour, m. Chan-Vese on CBCT using GTV as its initial contour and n. Chan-Vese model on PCA image using centre of GTV as its initial contour

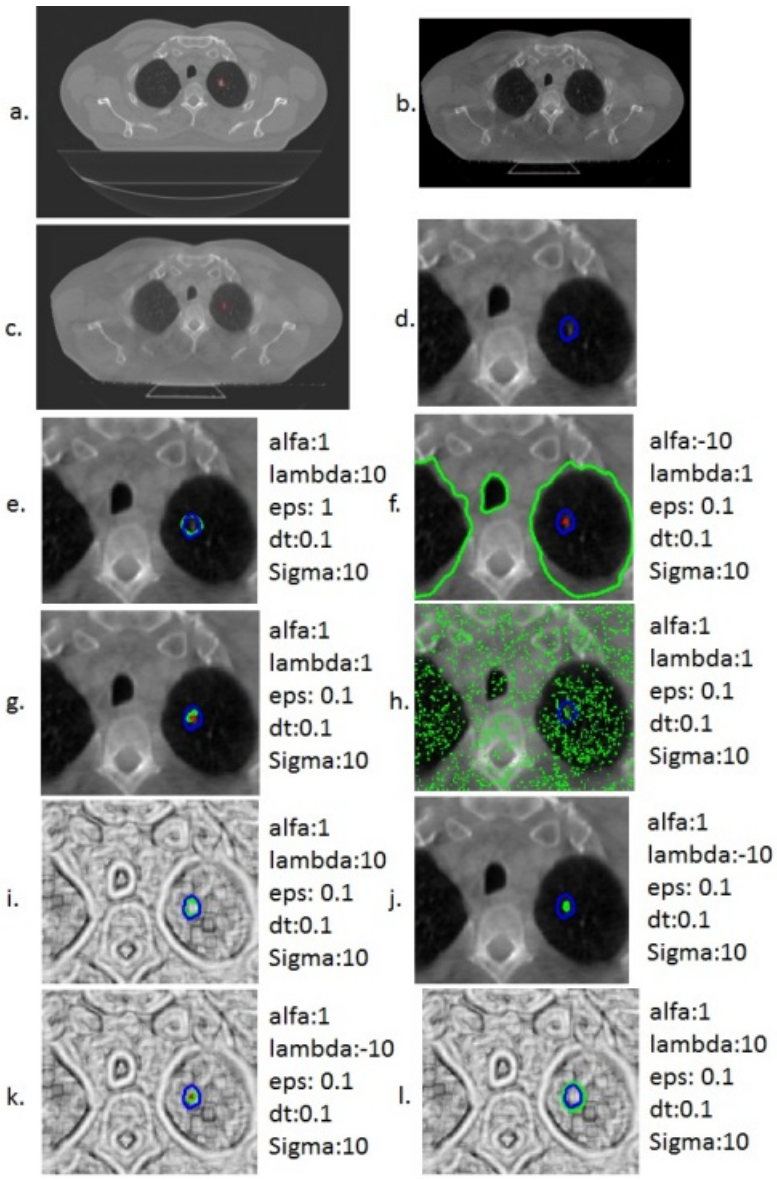

Figure B.8: Performance of different combinations with different parameters for lung CBCT image tumour segmentation, Patient 3-Slice 25: a. planning-CT, b. CBCT #1, c. registered CBCT, d. cropped part of of part c with clinical GTV, e. Li model on CBCT using GTV as its initial contour, f. Chan-Vese model on CBCT using centre of GTV as its initial contour, g. Li model on CBCT using centre of GTV as its initial contour, h. Chan-Vese model on texture image using GTV as its initial contour, i. Li model on PCA image using GTV as its initial contour, j. Chan-Vese model on vector-valued texture image using centre of GTV as its initial contour, k. Li model on PCA image using centre of GTV as its initial contour, l. Chan-Vese model on PCA image using GTV as its initial contour, m. Chan-Vese on CBCT using GTV as its initial contour and n. Chan-Vese model on PCA image using centre of GTV as its initial contour

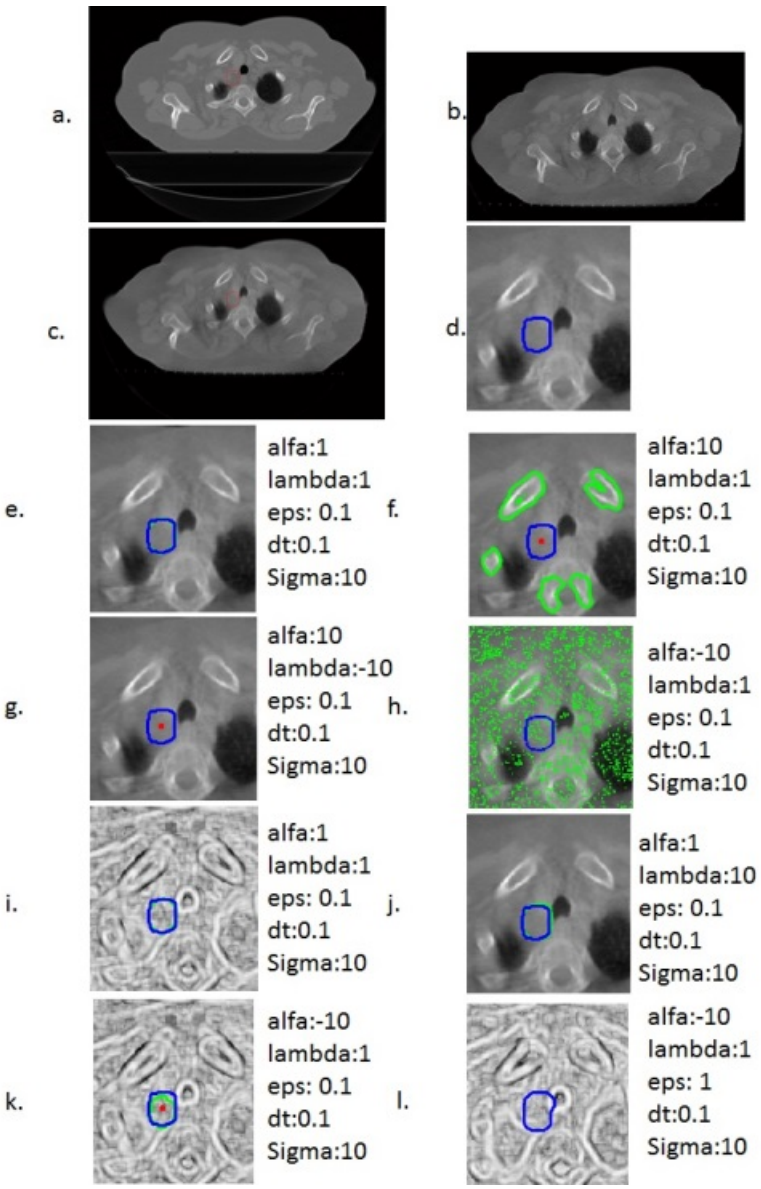

Figure B.9: Performance of different combinations with different parameters for lung CBCT image tumour segmentation, Patient 4-Slice 14: a. planning-CT, b. CBCT #1, c. registered CBCT, d. cropped part of of part c with clinical GTV, e. Li model on CBCT using GTV as its initial contour, f. Chan-Vese model on CBCT using centre of GTV as its initial contour, g. Li model on CBCT using centre of GTV as its initial contour, h. Chan-Vese model on texture image using GTV as its initial contour, i. Li model on PCA image using GTV as its initial contour, j. Chan-Vese model on vector-valued texture image using centre of GTV as its initial contour, k. Li model on PCA image using centre of GTV as its initial contour, l. Chan-Vese model on PCA image using GTV as its initial contour, m. Chan-Vese on CBCT using GTV as its initial contour and n. Chan-Vese model on PCA image using centre of GTV as its initial contour

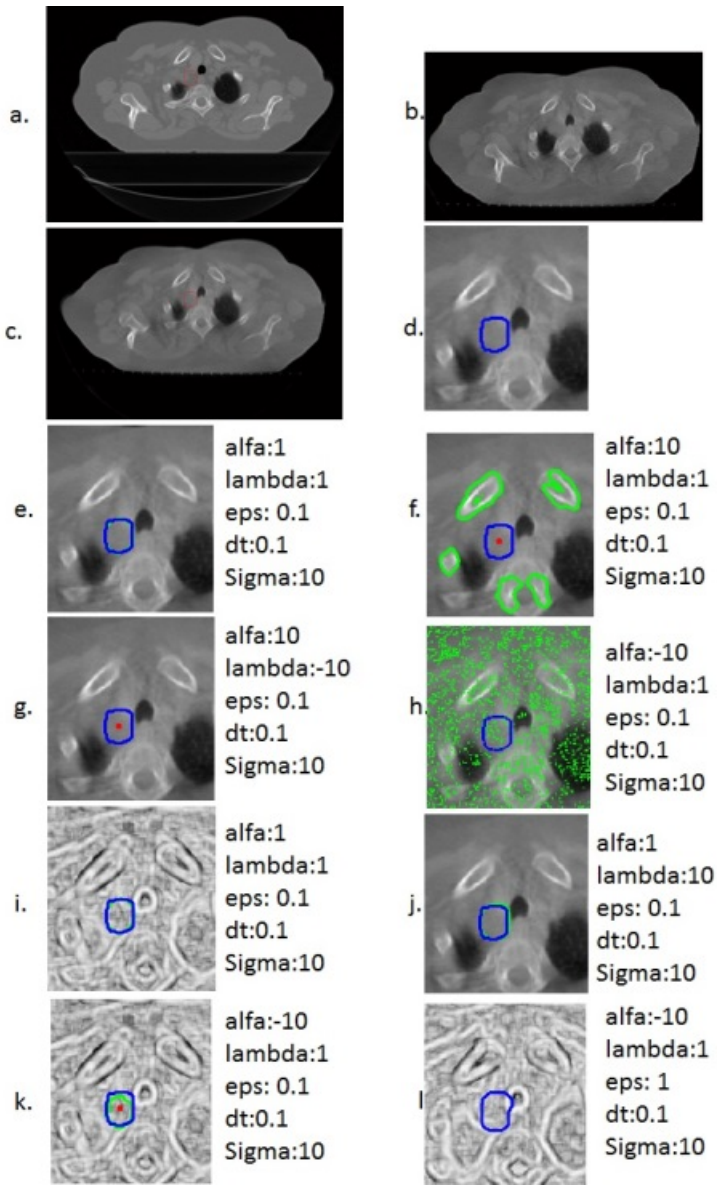

Figure B.10: Performance of different combinations with different parameters for lung CBCT image tumour segmentation, Patient 4-Slice 15: a. planning-CT, b. CBCT #1, c. registered CBCT, d. cropped part of of part c with clinical GTV, e. Li model on CBCT using GTV as its initial contour, f. Chan-Vese model on CBCT using centre of GTV as its initial contour, g. Li model on CBCT using centre of GTV as its initial contour, h. Chan-Vese model on texture image using GTV as its initial contour, i. Li model on PCA image using GTV as its initial contour, j. Chan-Vese model on vector-valued texture image using centre of GTV as its initial contour, k. Li model on PCA image using centre of GTV as its initial contour, l. Chan-Vese model on PCA image using GTV as its initial contour, m. Chan-Vese on CBCT using GTV as its initial contour and n. Chan-Vese model on PCA image using centre of GTV as its initial contour

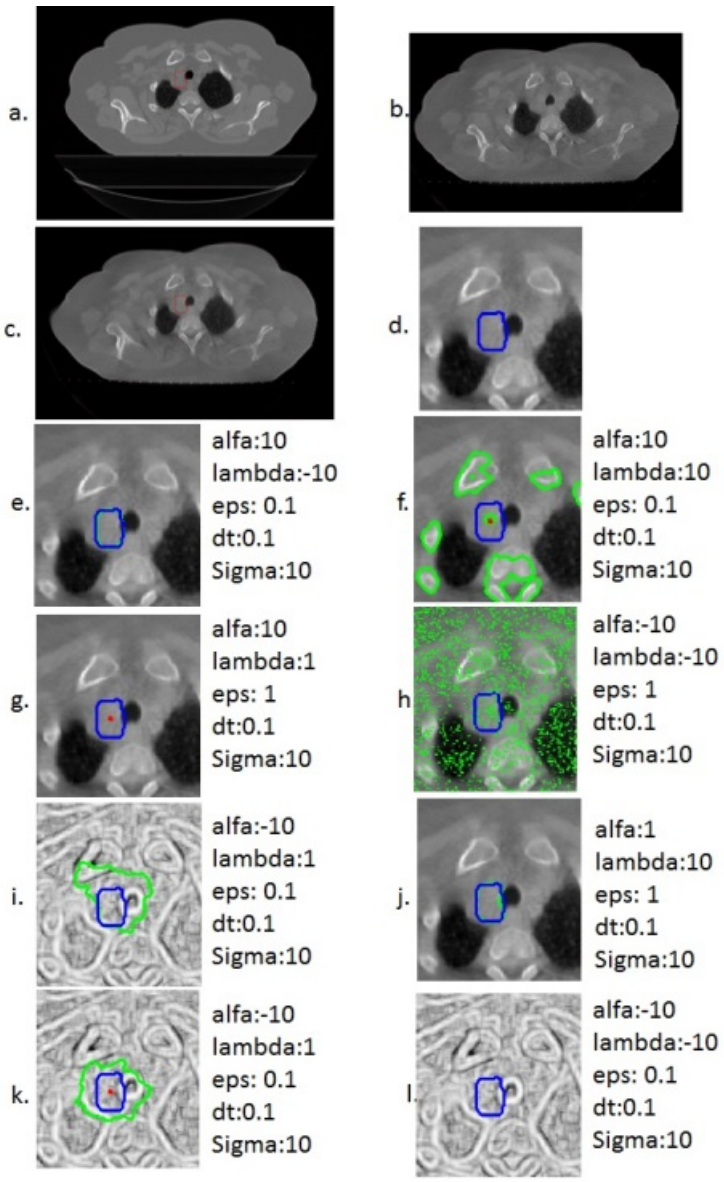

Figure B.11: Performance of different combinations with different parameters for lung CBCT image tumour segmentation, Patient 4-Slice 16: a. planning-CT, b. CBCT #1, c. registered CBCT, d. cropped part of of part c with clinical GTV, e. Li model on CBCT using GTV as its initial contour, f. Chan-Vese model on CBCT using centre of GTV as its initial contour, g. Li model on CBCT using centre of GTV as its initial contour, h. Chan-Vese model on texture image using GTV as its initial contour, i. Li model on PCA image using GTV as its initial contour, j. Chan-Vese model on vector-valued texture image using centre of GTV as its initial contour, k. Li model on PCA image using centre of GTV as its initial contour, l. Chan-Vese model on PCA image using GTV as its initial contour, m. Chan-Vese on CBCT using GTV as its initial contour and n. Chan-Vese model on PCA image using centre of GTV as its initial contour

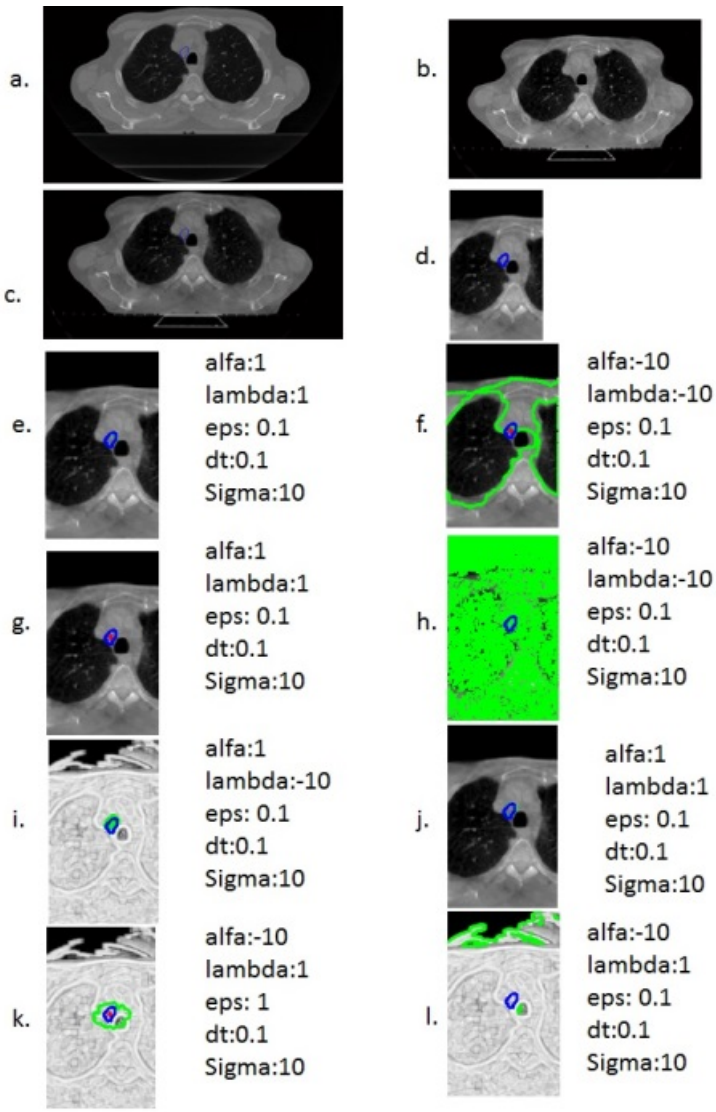

Figure B.12: Performance of different combinations with different parameters for lung CBCT image tumour segmentation, Patient 5-Slice 23: a. planning-CT, b. CBCT #1, c. registered CBCT, d. cropped part of of part c with clinical GTV, e. Li model on CBCT using GTV as its initial contour, f. Chan-Vese model on CBCT using centre of GTV as its initial contour, g. Li model on CBCT using centre of GTV as its initial contour, h. Chan-Vese model on texture image using GTV as its initial contour, i. Li model on PCA image using GTV as its initial contour, j. Chan-Vese model on vector-valued texture image using centre of GTV as its initial contour, k. Li model on PCA image using centre of GTV as its initial contour, l. Chan-Vese model on PCA image using GTV as its initial contour, m. Chan-Vese on CBCT using GTV as its initial contour and n. Chan-Vese model on PCA image using centre of GTV as its initial contour

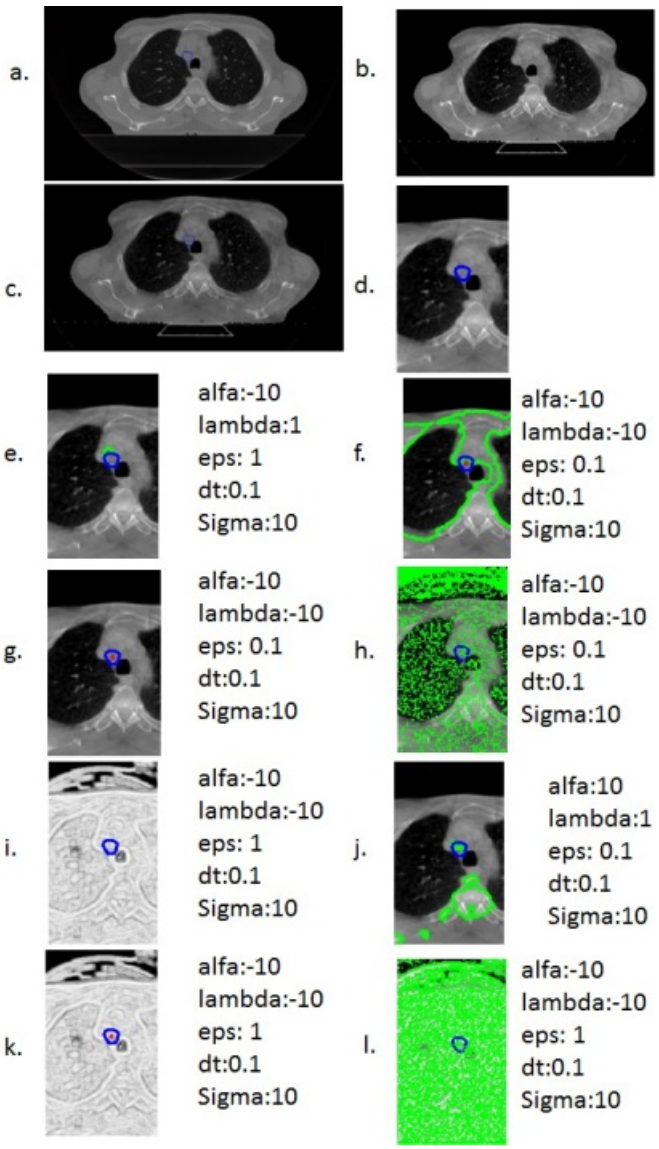

Figure B.13: Performance of different combinations with different parameters for lung CBCT image tumour segmentation, Patient 5-Slice 24: a. planning-CT, b. CBCT #1, c. registered CBCT, d. cropped part of of part c with clinical GTV, e. Li model on CBCT using GTV as its initial contour, f. Chan-Vese model on CBCT using centre of GTV as its initial contour, g. Li model on CBCT using centre of GTV as its initial contour, h. Chan-Vese model on texture image using GTV as its initial contour, i. Li model on PCA image using GTV as its initial contour, j. Chan-Vese model on vector-valued texture image using centre of GTV as its initial contour, k. Li model on PCA image using centre of GTV as its initial contour, l. Chan-Vese model on PCA image using GTV as its initial contour, m. Chan-Vese on CBCT using GTV as its initial contour and n. Chan-Vese model on PCA image using centre of GTV as its initial contour

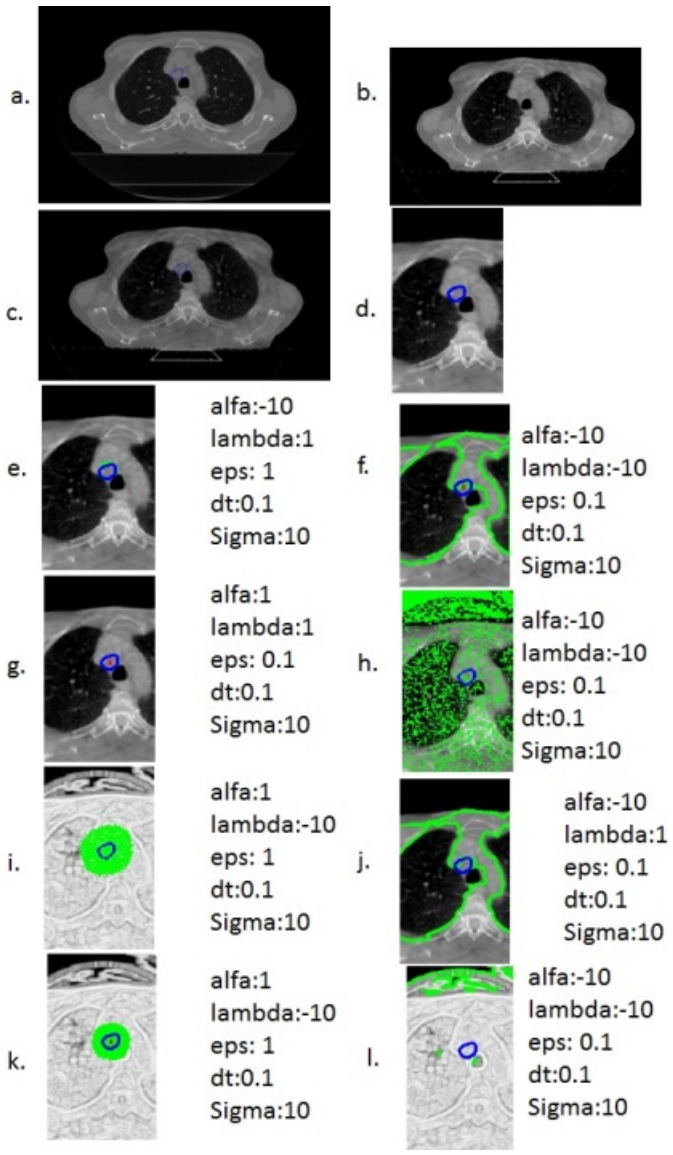

Figure B.14: Performance of different combinations with different parameters for lung CBCT image tumour segmentation, Patient 5-Slice 25: a. planning-CT, b. CBCT #1, c. registered CBCT, d. cropped part of of part c with clinical GTV, e. Li model on CBCT using GTV as its initial contour, f. Chan-Vese model on CBCT using centre of GTV as its initial contour, g. Li model on CBCT using centre of GTV as its initial contour, h. Chan-Vese model on texture image using GTV as its initial contour, i. Li model on PCA image using GTV as its initial contour, j. Chan-Vese model on vector-valued texture image using centre of GTV as its initial contour, k. Li model on PCA image using centre of GTV as its initial contour, l. Chan-Vese model on PCA image using GTV as its initial contour, m. Chan-Vese on CBCT using GTV as its initial contour and n. Chan-Vese model on PCA image using centre of GTV as its initial contour

Bibliography

[1] "Lung cancer statistics," http://www.cancerresearchuk.org/cancer-info/cancerstats/types/lung/, accessed: 11.02.2015.

[2] R. Baskar, K. A. Lee, R. Yeo, and K.-W. Yeoh, "Cancer and radiation therapy: current advances and future directions," *Int J Med Sci*, vol. 9, no. 3, pp. 193–199, 2012.

[3] "Three-dimensial basics: CT vs. CBCT," https://carestreamdentalblogdotcom1.wordpress.com/2014/01/03/three-dimensional-basics-ct-vs-cbct/, accessed: 03.07.2016.

[4] R. A. Novelline and L. F. Squire, "Squire's fundamentals of radiology." La Editorial, UPR, 2004.

[5] K. Rothkamm and M. Löbrich, "Evidence for a lack of DNA double-strand break repair in human cells exposed to very low X-ray doses," *Proceedings of the National Academy of Sciences*, vol. 100, no. 9, pp. 5057–5062, 2003.

[6] "Lung cancer - treatment," http://www.nhs.uk/conditions/cancer-of-the-lung/Pages/Treatment.aspx, accessed: 03.07.2016.

[7] "Prescribing, recording, and reporting photon-beam intensity-modulated radiation therapy (IMRT): Contents," *Journal of the ICRU*, vol. 10, no. 1, p. NP, 2010. [Online]. Available: http://jicru.oxfordjournals.org/content/10/1/NP.2.short

[8] V. Grégoire and T. Mackie, "State of the art on dose prescription, reporting and recording in intensity-modulated radiation therapy (ICRU report no. 83)," *Cancer/Radiothérapie*, vol. 15, pp. 555 – 559, 2011, 22e Congrés national de la Société fran çaise de radiothérapie oncologique (SFRO). [Online]. Available: http://www.sciencedirect.com/science/article/pii/S1278321811000989

[9] R. B. Den and A. P. Dicker, "IMRT, IGRT, SBRT: Advances in treatment planning and delivery of radiotherapy," *International Journal of Radiation Oncology Biology Physics*, vol. 83, no. 1, pp. e3 –, 2012. [Online]. Available: http://www.sciencedirect.com/science/article/pii/S0360301611036546

[10] "Key statistics for lung cancer," http://www.cancer.org/cancer/lungcancer-non-smallcell/detailedguide/non-small-cell-lung-cancer-key-statistics, accessed: 04.07.2016.

[11] "Lung cancer patients cost the nhs £9000 per patient," http://www.thetimes.co.uk/tto/health/news/article3592276.ece, accessed: 12.07.2016.

[12] "Cancer research center," http://www.cancerresearchuk.org/about-cancer/type/lung-cancer/about/types-of-lung-cancer, accessed: 10.05.2016.

[13] "Lung cancer survival statistics," http://www.cancerresearchuk.org/health-professional/cancer-statistics/statistics-by-cancer-type/lung-cancer/survival#jMPBbsmC1Pf5tP8H.99, accessed: 10.05.2016.

[14] "Lung cancer-low dose CT chest lung cancer screening," http://www.memradiology.com/procedures/lung-cancer/, accessed: 08.07.2016.

[15] "Lung cancer," http://www.slideshare.net/ksuneet/lung-cancer-8943833, accessed: 08.07.2016.

[16] "Staging of lung cancer," http://www.cancerresearchuk.org/about-cancer/type/lung-cancer/treatment/more-about-lung-cancer-staging, accessed: 23.07.2016.

[17] "Radiotherapy - how it is performed," http://www.nhs.uk/Conditions/Radiotherapy/Pages/How-it-is-performed.aspx, accessed: 09.02.2017.

[18] U. M. Graf, "Radiotherapy apparatus equipped with an articulable gantry for positioning an imaging unit," 2005, uS Patent 6,888,919.

[19] J. Vandemeulebroucke, "Lung motion modelling and estimation for image guided radiation therapy," Ph.D. dissertation, INSA, Lyon, 2010.

[20] J. M. Galvin, G. Ezzell, and A. Eisbrauch, "Implementing IMRT in clinical practice: a joint document of the American Society for Therapeutic Radiology and Oncology and the American Association of Physicists in Medicine," *International Journal of Radiation Oncology, Biology, Physics*, vol. 58(5), pp. 1616–1634, 2004.

[21] "Three-dimensial basics: CT vs. CBCT," http://doctorsgates.blogspot.co.uk/2011/02/terms-of-position-direction-and-main.html, accessed: 09.07.2016.

[22] H. Gray, "Anatomy of the human body." Lea & Febiger, 1918.

[23] O. S. Pianykh, "What is DICOM?" in *Digital Imaging and Communications in Medicine (DICOM)*. Springer, 2012, pp. 3–5.

[24] A. B. de González and S. Darby, "Risk of cancer from diagnostic X-rays: estimates for the UK and 14 other countries," *The Lancet*, vol. 363, no. 9406, pp. 345 – 351, 2004. [Online]. Available: http://www.sciencedirect.com/science/article/pii/S0140673604154330

[25] "CT Scan Info," http://crashingpatient.com/imaging/ct-scan-info.htm/, accessed: 08.07.2016.

[26] R. Gonzalez, R. E. Woods, and S. L. Eddins, "Digital image processing." Addison-Wesley, 1987.

[27] D. Cremers, M. Rousson, and R. Deriche, "A review of statistical approaches to level set segmentation: integrating color, texture, motion and shape," *International journal of computer vision*, vol. 72, no. 2, pp. 195–215, 2007.

[28] Y. Jiang, M. Wang, and H. Xu, "A survey for region-based level set image segmentation," pp. 413–416, 2012.

[29] G. Vineetha and G. Darshan, "Level set method for image segmentation: a survey," *IOSR J. Comput. Eng*, vol. 8, pp. 74–78, 2013.

[30] X. C. Tai and T. F. Chan, "A survey on multiple level set methods with applications for identifying piecewise constant functions," *Int. J. Numer. Anal. Model*, vol. 1, no. 1, pp. 25–47, 2004.

[31] C. Baillard, P. Hellier, and C. Barillot, "Segmentation of brain 3D MR images using level sets and dense registration," *Medical Image Analysis*, vol. 5, no. 3, pp. 185–194, 2001.

[32] K. Aloui and M. Naceur, "3D brain tumor segmentation using level-sets method and meshes simplification from volumetric MR images," *World Acad. Sci. Eng. Technol*, vol. 57, pp. 127–131, 2009.

[33] S. Taheri, S. H. Ong, and V. Chong, "Level-set segmentation of brain tumors using a threshold-based speed function," *Image and Vision Computing*, vol. 28, no. 1, pp. 26–37, 2010.

[34] ——, "Threshold-based 3D tumor segmentation using level set (TSL)," in *Applications of Computer Vision, 2007. WACV'07. IEEE Workshop on.* IEEE, 2007, pp. 45–45.

[35] J. Zhou, T.-K. Lim, V. Chong, and J. Huang, "Segmentation and visualization of nasopharyngeal carcinoma using MRI," *Computers in biology and medicine*, vol. 33, no. 5, pp. 407–424, 2003.

[36] S. Vinitski, C. Gonzalez, F. Mohamed, T. Iwanaga, R. L. Knobler, K. Khalili, and J. Mack, "Improved intracranial lesion characterization by tissue segmentation based on a 3D feature map," *Magnetic resonance in medicine*, vol. 37, no. 3, pp. 457–469, 1997.

[37] B. Scholkopf and A. J. Smola, "Learning with kernels: support vector machines, regularization, optimization, and beyond." MIT press, 2001.

[38] J. Zhang, K.-K. Ma, M.-H. Er, V. Chong *et al.*, "Tumor segmentation from magnetic resonance imaging by learning via one-class support vector machine," in *International Workshop on Advanced Image Technology (IWAIT'04)*, 2004, pp. 207–211.

[39] C. García and J. A. Moreno, "Kernel based method for segmentation and modeling of magnetic resonance images," pp. 636–645, 2004.

[40] L. M. Fletcher-Heath, L. O. Hall, D. B. Goldgof, and F. R. Murtagh, "Automatic segmentation of non-enhancing brain tumors in magnetic resonance images," *Artificial Intelligence in Medicine*, vol. 21, no. 1, pp. 43–63, 2001.

[41] M. Kass, A. Witkin, and D. Terzopoulos, "Snakes: Active contour models," *International journal of computer vision*, vol. 1, no. 4, pp. 321–331, 1988.

[42] S. Osher and J. A. Sethian, "Fronts propagating with curvature-dependent speed: algorithms based on hamilton-jacobi formulations," *Journal of computational physics*, vol. 79, no. 1, pp. 12–49, 1988.

[43] J. A. Sethian, "Level set methods and fast marching methods: evolving interfaces in computational geometry, fluid mechanics, computer vision, and materials science," vol. 3. Cambridge university press, 1999.

[44] Y. Jiang, M. Wang, and H. Xu, "A survey for region-based level set image segmentation," in *Distributed Computing and Applications to Business, Engineering Science (DCABES), 2012 11th International Symposium on*, Oct 2012, pp. 413–416.

[45] J. S. Suri and K. Liu, "Level set regularizers for shape recovery in medical images," in *Proceedings of the 26th IEEE International Symposium on Computer-Based Medical Systems*. IEEE Computer Society, 2001, pp. 0369–0369.

[46] E. Angelini, Y. Jin, and A. Laine, "State of the art of level set methods in segmentation and registration of medical imaging modalities," in *Handbook of Biomedical Image Analysis*. Springer, 2005, pp. 47–101.

[47] M. Burger and S. J. Osher, "A survey on level set methods for inverse problems and optimal design," *European Journal of Applied Mathematics*, vol. 16, no. 02, pp. 263–301, 2005.

[48] J. Montagnat, H. Delingette, and N. Ayache, "A review of deformable surfaces: topology, geometry and deformation," *Image and vision computing*, vol. 19, no. 14, pp. 1023–1040, 2001.

[49] J. S. Suri, K. Liu, S. Singh, S. N. Laxminarayan, X. Zeng, and L. Reden, "Shape recovery algorithms using level sets in 2D/3D medical imagery: a state-of-the-art review," *Information Technology in Biomedicine, IEEE Transactions on*, vol. 6, no. 1, pp. 8–28, 2002.

[50] Z. C. Bhaidasna and S. Mehta, "Article: A review on level set method for image segmentation," *International Journal of Computer Applications*, vol. 63, no. 11, pp. 20–22, February 2013, full text available.

[51] A. M. Dale, B. Fischl, and M. I. Sereno, "Cortical surface-based analysis: I. segmentation and surface reconstruction," *Neuroimage*, vol. 9, no. 2, pp. 179–194, 1999.

[52] J. A. Sethian and P. Smereka, "Level set methods for fluid interfaces," *Annual review of fluid mechanics*, vol. 35, no. 1, pp. 341–372, 2003.

[53] G. Xingfei and T. Jie, "An automatic active contour model for multiple objects," in *Pattern Recognition, 2002. Proceedings. 16th International Conference on*, vol. 2, 2002, pp. 881–884 vol.2.

[54] C. Li, J. Liu, and M. Fox, "Segmentation of edge preserving gradient vector flow: an approach toward automatically initializing and splitting of snakes," in *Computer Vision and Pattern Recognition, 2005. CVPR 2005. IEEE Computer Society Conference on*, vol. 1, June 2005, pp. 162–167 vol. 1.

[55] B. Li and S. Acton, "Automatic active model initialization via poisson inverse gradient," *Image Processing, IEEE Transactions on*, vol. 17, no. 8, pp. 1406–1420, Aug 2008.

[56] P. Ghosh, M. Mitchell, J. A. Tanyi, and A. Hung, "A genetic algorithm-based level set curve evolution for prostate segmentation on pelvic CT and MR images," 2009.

[57] R. Ganta, S. Zaheeruddin, N. Baddiri, and R. Rao, "Particle swarm optimization clustering based level sets for image segmentation," in *India Conference (INDICON), 2012 Annual IEEE*, Dec 2012, pp. 1053–1056.

[58] D. Jiang, B. Xu, and L. Ge, "A hybrid multi-cell tracking approach with level set evolution and ant colony optimization," in *Advances in Swarm and Computational Intelligence*. Springer, 2015, pp. 213–221.

[59] V. Caselles, R. Kimmel, and G. Sapiro, "Geodesic active contours," *International journal of computer vision*, vol. 22, no. 1, pp. 61–79, 1997.

[60] R. Malladi, J. A. Sethian, and B. C. Vemuri, "Shape modeling with front propagation: A level set approach," *Pattern Analysis and Machine Intelligence, IEEE Transactions on*, vol. 17, no. 2, pp. 158–175, 1995.

[61] M. E. Leventon, W. E. L. Grimson, and O. Faugeras, "Statistical shape influence in geodesic active contours," in *Computer Vision and Pattern Recognition, 2000. Proceedings. IEEE Conference on*, vol. 1. IEEE, 2000, pp. 316–323.

[62] T. Chan and L. Vese, "An active contour model without edges," in *Scale-Space Theories in Computer Vision*. Springer, 1999, pp. 141–151.

[63] T. F. Chan, B. Y. Sandberg, and L. A. Vese, "Active contours without edges for vector-valued images," *Journal of Visual Communication and Image Representation*, vol. 11, no. 2, pp. 130–141, 2000.

[64] D. Mumford and J. Shah, "Optimal approximations by piecewise smooth functions and associated variational problems," *Communications on pure and applied mathematics*, vol. 42, no. 5, pp. 577–685, 1989.

[65] L. A. Vese and T. F. Chan, "A multiphase level set framework for image segmentation using the mumford and shah model," *International journal of computer vision*, vol. 50, no. 3, pp. 271–293, 2002.

[66] M. Rousson, "Cue integration and front evolution in image segmentation," Ph.D. dissertation, Nice, 2004.

[67] M. Lianantonakis and Y. R. Petillot, "Sidescan sonar segmentation using active contours and level set methods," in *Oceans 2005-Europe*, vol. 1. IEEE, 2005, pp. 719–724.

[68] N. Zhang, J. Zhang, and R. Shi, "An improved Chan–Vese model for medical image segmentation," in *Computer Science and Software Engineering, 2008 International Conference on*, vol. 1. IEEE, 2008, pp. 864–867.

[69] K. Zhang, L. Zhang, H. Song, and W. Zhou, "Active contours with selective local or global segmentation: A new formulation and level set method," *Image and Vision Computing*, vol. 28, no. 4, pp. 668–676, 2010.

[70] K. Zhang, H. Song, and L. Zhang, "Active contours driven by local image fitting energy," *Pattern recognition*, vol. 43, no. 4, pp. 1199–1206, 2010.

[71] C. Li, C.-Y. Kao, J. C. Gore, and Z. Ding, "Minimization of region-scalable fitting energy for image segmentation," *Image Processing, IEEE Transactions on*, vol. 17, no. 10, pp. 1940–1949, 2008.

[72] S. Liu and Y. Peng, "A local region-based Chan–Vese model for image segmentation," *Pattern Recognition*, vol. 45, no. 7, pp. 2769–2779, 2012.

[73] X. F. Wang, D. S. Huang, and H. Xu, "An efficient local Chan–Vese model for image segmentation," *Pattern Recognition*, vol. 43, no. 3, pp. 603–618, 2010.

[74] S. Lankton and A. Tannenbaum, "Localizing region-based active contours," *Image Processing, IEEE Transactions on*, vol. 17, no. 11, pp. 2029–2039, 2008.

[75] S. Kichenassamy, A. Kumar, P. Olver, A. Tannenbaum, and A. Yezzi, "Gradient flows and geometric active contour models," in *Computer Vision, 1995. Proceedings., Fifth International Conference on*, Jun 1995, pp. 810–815.

[76] O. Michailovich, Y. Rathi, and A. Tannenbaum, "Image segmentation using active contours driven by the Bhattacharyya gradient flow," *Image Processing, IEEE Transactions on*, vol. 16, no. 11, pp. 2787–2801, Nov 2007.

[77] M. Pereyra, H. Batatia, and S. McLaughlin, "Exploiting information geometry to improve the convergence properties of variational active contours," *IEEE Journal of Selected Topics in Signal Processing*, vol. 7, no. 4, pp. 700–707, 2013.

[78] Y. Yuan and C. He, "Variational level set methods for image segmentation based on both L^2 and sobolev gradients," *Nonlinear Analysis: Real World Applications*, vol. 13, no. 2, pp. 959 – 966, 2012. [Online]. Available: http://www.sciencedirect.com/science/article/pii/S1468121811002689

[79] K. Cheng, L. Gu, and J. Xu, "A novel shape prior based level set method for liver segmentation from MR images," in *Information Technology and Applications in Biomedicine, 2008. ITAB 2008. International Conference on.* IEEE, 2008, pp. 144–147.

[80] O. Bernard, D. Friboulet, P. Thévenaz, and M. Unser, "Variational B-spline level-set: a linear filtering approach for fast deformable model evolution," *Image Processing, IEEE Transactions on*, vol. 18, no. 6, pp. 1179–1191, 2009.

[81] Y. Shi and W. C. Karl, "A real-time algorithm for the approximation of level-set-based curve evolution," *Image Processing, IEEE Transactions on*, vol. 17, no. 5, pp. 645–656, 2008.

[82] M. Droske, B. Meyer, M. Rumpf, and C. Schaller, "An adaptive level set method for medical image segmentation," in *Information Processing in Medical Imaging*. Springer, 2001, pp. 416–422.

[83] S. Bara, M. A. Kerroum, A. Hammouch, and D. Aboutajdine, "Variational image segmentation models: Application to medical images MRI," in *Multimedia Computing and Systems (ICMCS), 2011 International Conference on.* IEEE, 2011, pp. 1–4.

[84] S. Ho, H. Cody, and G. Gerig, "Snap: A software package for user-guided geodesic snake segmentation," *Submitted to MICCAI 2003*, 2003.

[85] A. E. Lefohn, J. E. Cates, and R. T. Whitaker, "Interactive, GPU-based level sets for 3D segmentation," in *Medical Image Computing and Computer-Assisted Intervention-MICCAI 2003.* Springer, 2003, pp. 564–572.

[86] P. Lin, C. xun Zheng, and Y. Yang, "Model-based medical image segmentation: a level set approach," in *Intelligent Control and Automation, 2004. WCICA 2004. Fifth World Congress on*, vol. 6, 2004, pp. 5541–5544 Vol.6.

[87] Z. Cao, Y. Pi, X. Yang, and J. Xiong, "A variational level set SAR image segmentation approach based on statistical model," in *Synthetic Aperture Radar (EUSAR), 2008 7th European Conference on*, 2008, pp. 1–4.

[88] K. Zhang, L. Zhang, and S. Zhang, "A variational multiphase level set approach to simultaneous segmentation and bias correction," in *Image Processing (ICIP), 2010 17th IEEE International Conference on.* IEEE, 2010, pp. 4105–4108.

[89] S. D. El Hadji, S. O. Ba, T. Jerbi, and V. Burdin, "Variational and shape prior-based level set model for image segmentation," in *AIP Conference Proceedings*, vol. 1281, 2010, p. 2139.

[90] C. Li, C.-Y. Kao, J. C. Gore, and Z. Ding, "Implicit active contours driven by local binary fitting energy," in *Computer Vision and Pattern Recognition, 2007. CVPR'07. IEEE Conference on.* IEEE, 2007, pp. 1–7.

[91] C. Li, R. Huang, Z. Ding, J. Gatenby, D. N. Metaxas, and J. C. Gore, "A level set method for image segmentation in the presence of intensity inhomogeneities with application to MRI," *Image Processing, IEEE Transactions on*, vol. 20, no. 7, pp. 2007–2016, 2011.

[92] P. Brodatz, "Textures: a photographic album for artists and designers." Dover Pubns, 1966.

[93] K. H. Zou, S. K. Warfield, A. Bharatha, C. M. Tempany, M. R. Kaus, S. J. Haker, W. M. Wells, F. A. Jolesz, and R. Kikinis, "Statistical validation of image segmentation quality based on a spatial overlap index 1: Scientific reports," *Academic radiology*, vol. 11, no. 2, pp. 178–189, 2004.

[94] R. Haralick, "Statistical and structural approaches to texture," *Proceedings of the IEEE*, vol. 67, no. 5, pp. 786–804, May 1979.